On the Aerodynamics of Trailing Edge Serrations at Low Reynolds Numbers

Israel Bron Simplicio

A thesis

submitted in partial fulfillment of the

requirements for the degree of

Master of Science

University of Washington

2022

Committee:

Robert E. Breidenthal

James C. Hermanson

Program Authorized to Offer Degree:

Aeronautics and Astronautics

University of Washington

Abstract

On the Aerodynamics of Trailing Edge Serrations at Low Reynolds Numbers

Israel Bron Simplicio

Chair of the Supervisory Committee:
Robert E. Breidenthal
Department of Aeronautics and Astronautics

This Master thesis presented an aerodynamic evaluation of wing sections with a serrated trailing edge at flow conditions analogous to those of micro aerial vehicles (MAVs). Tests were performed at Reynolds Numbers between 30,000 and 200,000 on two different wind tunnels. A series of serration configurations were considered with different variables including wavelength, amplitude, and shape of serrations. Five serration shapes were used, all with a thin flat plate as a baseline profile: (i) blunt, (ii) triangular, (iii) quadratic bird feather-like, (iv) quadratic membrane-like, and (v) quadratic membrane-like with tapering. Trailing edge serrations affected the wings' aerodynamic parameters such as C_L, C_D and C_M and reduced the wing sections weight. Results indicated that bird feather-like serrations and quadratic membrane-like ones with tapering provided the highest aerodynamic benefits, accounting for a potential increase in range for MAVs that implement such serrations. Parts of this thesis were presented on the 2020 PNW AIAA TECH Symposium's Poster session and on the 2022 AIAA Scitech Forum [1, 2].

TABLE OF CONTENTS

LIST OF FIGURES

LIST OF TABLES

ACKNOWLEDGEMENTS

I would like to acknowledge Professor Robert Breidenthal and Giovanni Nino for their advice and guidance throughout this thesis project. I would also like to recognize my fiancée, Laura Albert, and my parents, Jalimar and Ana Beatriz, for their constant support throughout my time as a master student.

DEDICATION

This master thesis is dedicated to my fiancée, Laura Albert, and my parents, Jalimar Guimarães Simplício and Ana Beatriz Bron Simplício.

NOMENCLATURE

A = reference area
$A_{c.s}$ = area of test section
$A_{frontal}$ = frontal area of test sample
A_{wake} = wake area of test sample
C_L = coefficient of lift
C_D = coefficient of drag
C_M = coefficient of pitching moment
c = maximum chord length of airfoil [m]
c_{mean} = mean chord length of airfoil [m]
D = drag [N]
d = amplitude of serration [m]
L = lift [N]
MAV = micro aerial vehicle
M = pitching moment [N.m]
q_∞ = dynamic pressure [Pa]
Re = Reynolds Number
s = spanwise length [m]
LE = leading edge
TE = trailing edge
t = thickness of wing section [m]
U_∞ = freestream velocity [m/s]
x = streamwise coordinate measured from the leading edge of the wing [m]
y = wing normal coordinate measured from the leading edge of the wing [m]
z = spanwise coordinate measured from the leading edge of the wing [m]
α = angle of attack (°)
λ = amplitude of serration [m]
μ = dynamic viscosity [kg/m·s]
μWT = Micro Wind Tunnel
3’x3’ WT = 3 ft x 3 ft Wind Tunnel
ρ = density [kg/m^3]

Chapter 1. INTRODUCTION

Since the early stages of aviation, engineers and inventors have studied a variety of wing configurations. These ranged from biplane models designed by the Wright brothers' Flyer and Alberto Santos-Dumont's No. 14 Bis to monoplanes that resembled most modern commercial aircraft like Santos-Dumont's Demoiselle aircraft series [3]. Other notable names, from even earlier periods, included Otto Lilienthal and his experiments with gliders and Leonardo da Vinci with his studies and designs of flying machines [4, 5]. Each one of these aviation pioneers presented different designs and approaches that continued to evolve with time, including the first examples of serrated TEs as seen in Figure 1.2 [5].

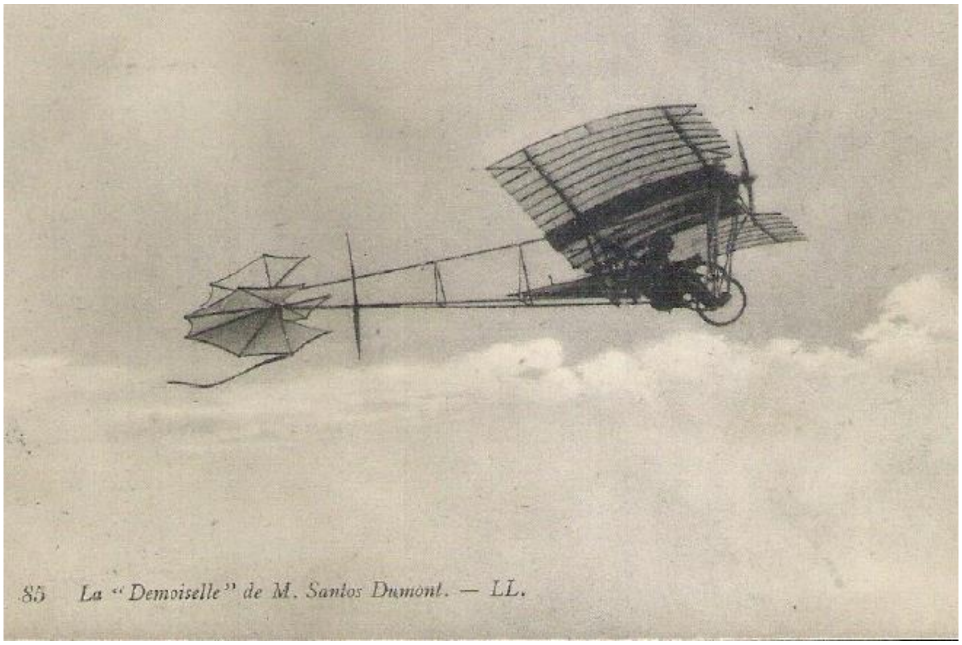

Figure 1.1. The Demoiselle airplane by Santos-Dumont 1909 [3]

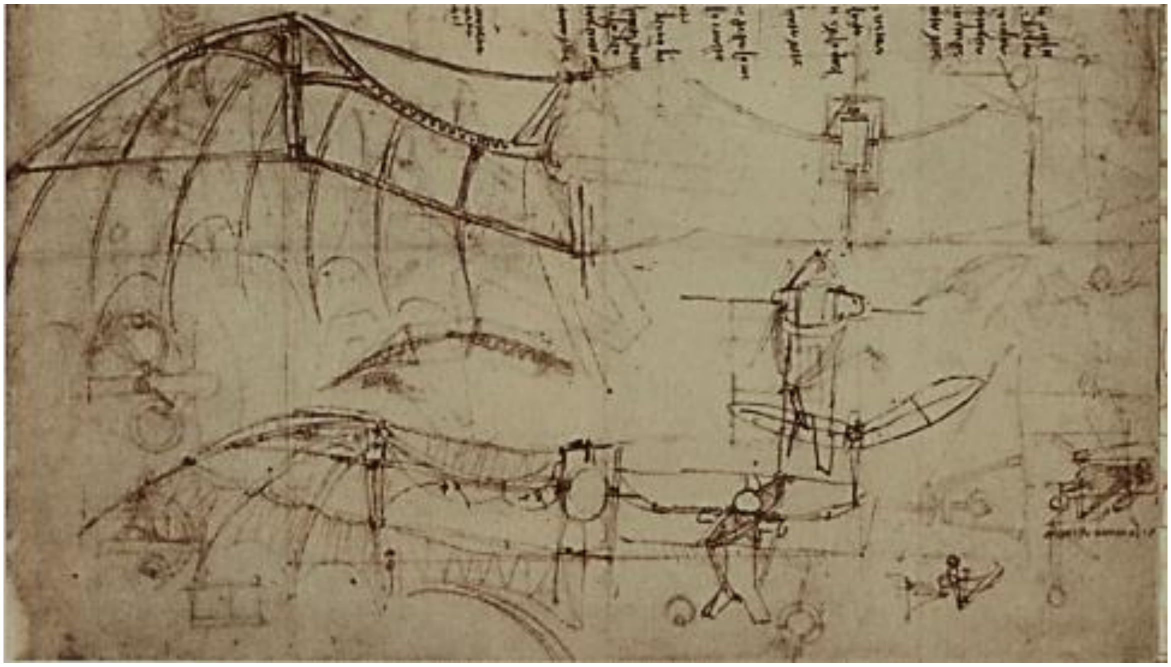

Figure 1.2. Aliant “ornitottero” wing by Leonardo da Vinci [5]

1.1 RESEARCH MOTIVATION

Analogous to the numerous methods employed during the early wing developments, there are still many approaches that can lead to a better understanding of the flow around an airfoil. Some examples of contemporary branches include aeroacoustics and aerodynamics. In recent years, a trend of studies around serrated edges emerged with promising data being gathered regarding alternatives to blunt TEs, regular bluff body airfoils or other standard shapes [6]. There is still, however, much to be learned from applying more unique or complex configurations of serrations. In order to find promising serration designs for this thesis, it was important to first find valuable sources of inspiration. Among them three were of key relevance: (i) nature, (ii) previous technological developments, and (iii) the potential applications for Micro-Aerial Vehicles (*MAVs*).

1.1.1 *Nature Examples*

Observations from nature have historically provided great insight for engineers, inventors and scientists. For instance, raindrops served greatly for the understanding of aerodynamic shapes, and ducks with their webbed feet inspired swim fins. With this in mind, the presence of complex serration-like shapes on the TE of animals' and insects' wings (bats, birds and butterflies, for example) was one specific aspect considered when seeking to expand the knowledge of wing aerodynamics and wing design improvement [7, 8].

Another interesting source of inspiration when considering biological approaches to interactions with fluid was observing marine and fluvial life. For example, tubercles on humpback whales' flippers have been a topic of research on the functionality of sinusoidal serrations which were understood to act as a flow control device [9, 10]. Figure 1.3 illustrates the LE serrations present at the flippers [10]. Such observations also served as inspiration for research and applications of LE sinusoidal serrations on wind turbines and even suggestions of use in the aircraft industry [9].

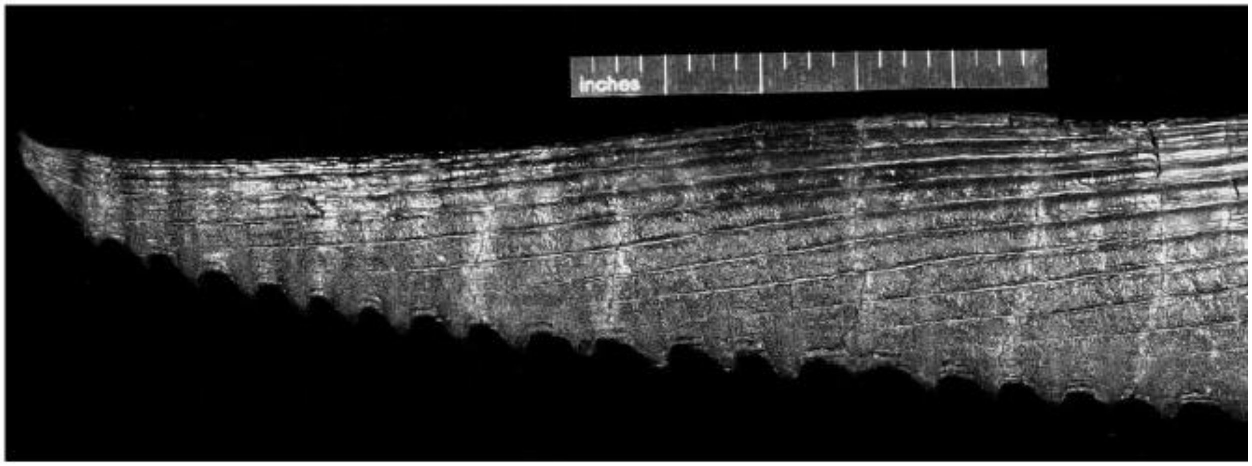

Figure 1.3. Segment of pectoral fin from Protosphyraena with LE protrusions [10]

1.1.2 *Engineering Inspiration*

Serration-like designs are not new to different engineering applications such as wind turbine blades, gas turbine covers or even state-of-the-art motorsport aerodynamic devices. Beginning with wind turbine blades, it was possible to observe their use both at the LE and TE [10, 11, 12]. Figure 1.4 illustrates blades with the serrations present at the LE and TE of wind turbines. These designs included sinusoidal-like serrations as well as triangular ones [10, 11, 12].

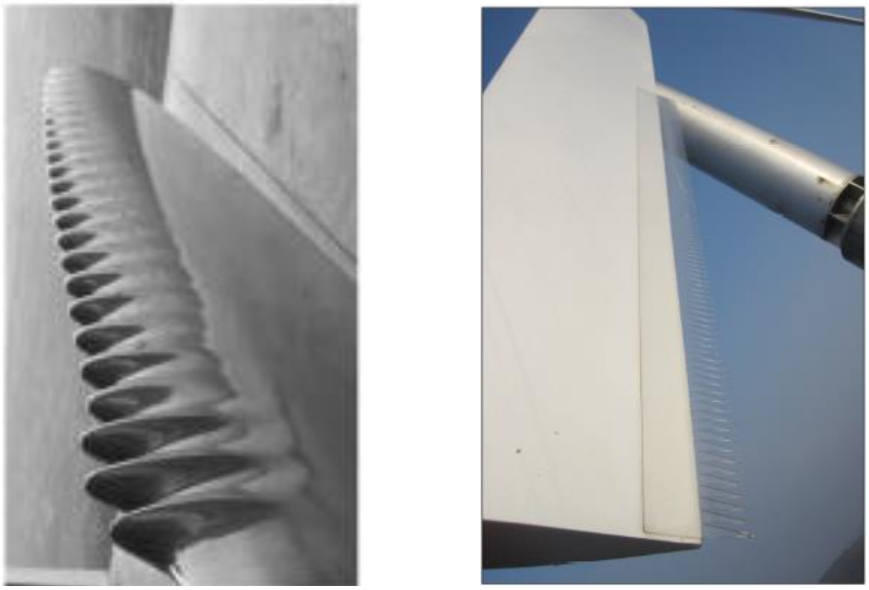

Figure 1.4. Wind turbine blades with serrations at the LE (left) [10] and TE (right) [11]

Furthermore, it was interesting to observe the impact of adding serrations to a body that was subject to a flow stream. In the case of wind turbine blades, one of the main motivations was noise reduction [11]. This was also the case for chevron serrations present in gas turbine covers of some aircraft — see Figure 1.5 [13]. Both were very relevant areas where noise reduction was important for the improvement of noise pollution levels in areas near airports or wind power production plants. Cases such as the one used in rear wings of formula one cars, in turn, considered the potential aerodynamic benefits related to the introduction of the serrations [14].

Figure 1.5. Chevron serrations at gas turbine cover [13]

1.1.3 *Micro-Air Vehicles*

MAVs, a relatively new class of unmanned aerial vehicles, had their formal origins dating to the 1990's with Defense Advanced Research Projects Agency (DARPA) [15]. DARPA established their dimensions "being less than 15 cm", a term that has been loosely interpreted in practice [15]. Among MAVs' potential applications, one category rose as the most prominent use for these vehicles: reconnaissance at very low cost [16]. Some examples of this are military or police forces' surveillance of potentially dangerous areas, search and rescue missions and urban traffic management [16]. In many of these scenarios, the ability to be unnoticeable to bystanders or targets on the ground is necessary, thus requiring low levels of noise. Nonetheless, it is widely accepted that due to their generally small dimension, MAVs fly at low *Re* which cause their flow conditions to be different than those of larger aircrafts.

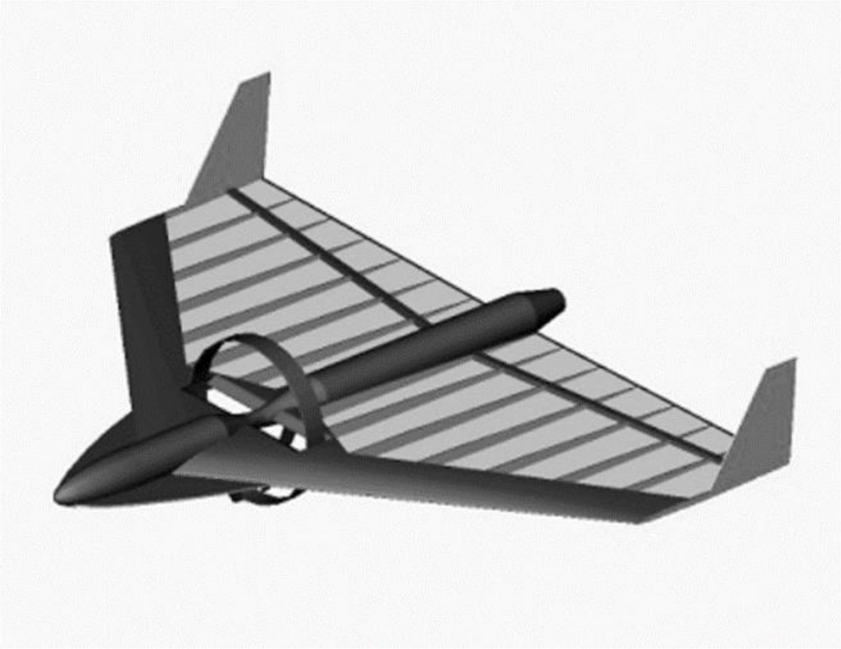

Figure 1.6. Fixed-wing MAV design [16]

Since early MAV developments, many different designs have been considered. These ranged from flapping wings inspired by birds and insects to fixed-wing models used for long endurance outdoors applications, and rotary wings for short endurance outdoors missions that require hovering capabilities [15, 16]. In light of this, fixed-wing MAVs, those that resemble conventional airplanes, were the application on which this thesis focused. In this context, serrations are a relatively new consideration with potential noise reduction and aerodynamic performance benefits.

1.2 THESIS OBJECTIVES

In light of the ongoing research on MAVs and serrated TEs, the aim of this thesis was the investigation of a series of serration shapes including: (i) blunt, (ii) triangular, (iii) quadratic bird feather-like, (iv) quadratic membrane-like, and (v) quadratic membrane-like with tapering. A thin flat plate was used as a baseline for all wings tested as an easy to customize and fabricate platform. The goal was to identify whether or not the serrated models improved the wing's aerodynamic characteristics when compared to the regular thin flat plate, as hypothesized. It was expected that the beneficial effects would increase at lower *Re*. The hypothesis was that the interaction between the vortex shedding and the streamwise vortices generated by the serrations would reduce the strength of the vortex shedding and, hence, the drag. This thesis also aimed to identify the best performing samples according to the following measures:

1. C_L, C_D and C_M performance.
2. Flow visualization.

The findings from this study and the potential revealed by it were intended to further the knowledge of how different types of TE serrations affect the performance of the wing, with the interest of applications on the MAV segment. As mentioned before, however, there are many more configurations available, and this thesis did not intend to claim an exclusive solution and design to this topic.

Chapter 2. BACKGROUND

2.1 AIRFOIL AERODYNAMICS

2.1.1 *Basic Concepts*

In order to understand the aerodynamic performance of the different wing sections, it is important, first, to discuss their basic parameters and aerodynamic descriptive characteristics. There are several common terms in the general description of an airfoil including *c*, camber, LE, TE, and *t* [17, 18]. A more descriptive set of parameters is presented in Figure 2.1 [17].

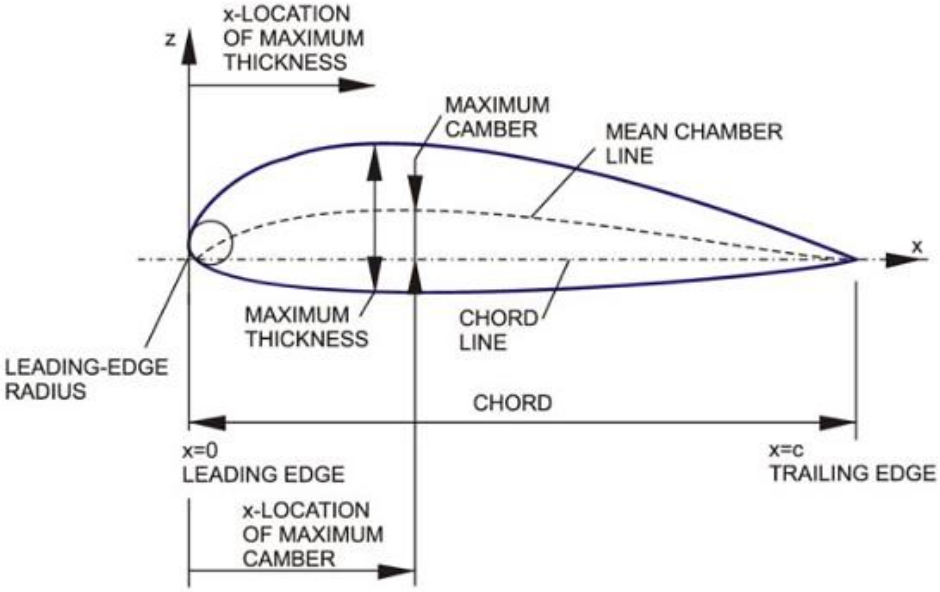

Figure 2.1. Airfoil design parameters [18]

With basic nomenclature defined, it is important to introduce some aerodynamic terms: lift (*L*), drag (*D*), and pitch moment (*M*). *L* and *D* are two of the most essential terms in airfoils aerodynamics. *L* represents an upwards vertical force component while *D* relates to the force acting in the same direction as the free flow [19]. These two terms can also be described by the non-dimensional counterparts, coefficient of lift (C_L) and coefficient of drag (C_D). These two terms were of more relevance for this thesis as they represent a metric commonly used across the academic and industrial environments. When measured based on different angles of attack (α), C_D and C_L provided useful information when analyzing the aerodynamic performance of a wing section.

The equations below describe C_L and C_D [19]:

$$C_L = \frac{L}{\frac{1}{2}\rho U_{\infty}^{2} A} \tag{2.1}$$

$$C_D = \frac{D}{\frac{1}{2}\rho U_{\infty}^{2} A} \tag{2.2}$$

2.1.2 *Truncated and Serrated Trailing Edge*

In the pursuit of improving wing design, different strategies were proposed. One of the early suggestions was using blunt or truncated TEs. This type of modification provided structural benefits in comparison to the full TE counterpart [20, 21]. The disadvantages, however, have been widely reported, showing an increase in intensity of the low-pressure area near the wing's TE [20, 21, 22]. This caused an increase in base *D* and ultimately in total *D* [20, 21, 22].

The aerodynamic related challenges of using a blunt TE or a bluff airfoil have led researchers to continue their search for more advantageous alternatives. Tanner, an early prominent figure in this field, investigated if changes in TE shape, such as the introduction of serrations and splitters, improved the airfoil's performance [20]. The "M" shaped serrations, for example, reached base *D* values that were 32% of the ones observed in a basic blunt TE with no apparent negative consequences to the wing section's *L* characteristics [20]. Figure 2.2 illustrates the C_D curves based on three different wing models observed by Tanner [20]. In his research, it was possible to infer that, when compared to non-truncated or bluff airfoils—a category referred to in this thesis as a regular wing—the serrated models indicated an increase in C_L [20].

However, an increase in C_D was also observed, something that was attributed to the vortex formation developed by the blunt portions of the serrations [20, 22].

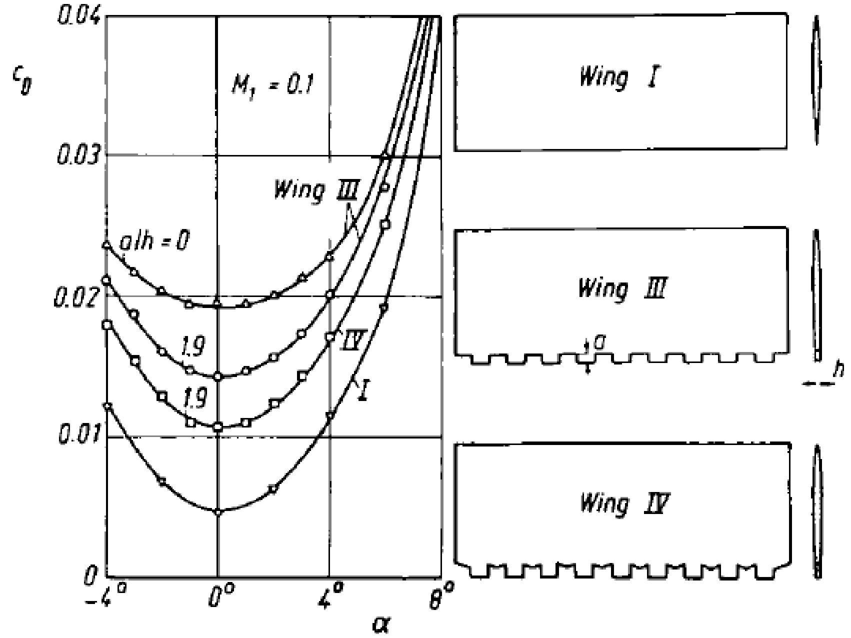

Figure 2.2. C_D of wings: no TE serration, rectangular and “M”-shaped serrations [20]

The early studies in the field of serrated TEs continued over the latter half of the 20th century and into the 21st century. Promising results led to patents such as US5088665 and US9670901 on TE serrations used for aerodynamic improvements and noise reduction, proving their value [23, 24]. Additional research conducted by Nedić & Vassilicos considered a series of different serration configurations ranging from triangular samples to more complex fractal serrations at *Re* = 150,000 [22]. Among some of the finds, it was revealed that the lift-to-drag ratio (C_L/C_D) could be improved for serrations with relatively wide chevron angle, while the addition of fractal/multi-scale patterns had little impact [22]. Furthermore, a reduction in C_D was linked to the weakening of intensity of spanwise coherent structures created by the von-Karman type shedding [22]. The employment of serrations yielded an increase in the maximum C_L/C_D of up to 8% compared to a regular wing without TE modifications [22]. These von-Karman vortex shedding structures have been well documented as an influencing factor on TE aerodynamic performance [25].

In another study, Hussain et al. compared the performance of quadratic spline-shaped TE serrations with the more conventional triangular ones, using as a base model a NACA 0012 airfoil at a *Re* = 360,000 [26]. Across their study it was concluded that use of quadratic spline-shaped TE serrations proved to increase C_L/C_D in comparison to similar triangular shaped TEs [26]. This was attributed to the reduction in the serrated TE's mean bluntness [26].

Figure 2.3. Wing and quadratic spline TE serration [26]

Thomareis & Papadakis developed a direct numerical study evaluating different types of TE shapes including straight, blunt and serrated models using the NACA 0012 airfoil as a baseline at *Re* = 50,000 [6]. Among other findings from this study, Thomareis & Papadakis identified the formation of a spanwise pressure gradient in samples adopting TE serrations [6]. This was attributed to the development of a secondary flow pattern in the wing section's spanwise direction [6]. The serrations were also linked to the attenuation of vortex shedding energy [6, 27]. These results indicated promising opportunities for applications of serrated devices in flows subject to very low *Re*, similar to the ones considered in this thesis.

Loughnane & Gunasekaran introduced a study comparing the aerodynamic performance of TE serrations (TEU), LE serrations (LEU), and of a combination of both (LETEU) [28]. The wing sections also had undulations parallel to the streamwise direction as seen in Figure 2.4. Among other observations, they identified that the TEU and LETEU yielded benefits in performance compared to baseline NACA 0012, especially at low α (200,000 < Re < 300,000). Meanwhile, the LEU and LETEU wings indicated post-stall benefits [28].

Figure 2.4. Examples of wing sections tested by Loughnane & Gunasekaran [28]

Other studies considered the use of serrations as an attachment to the wing section's TE [11, 29]. In their research, Liu et al. identified a reduction in C_D at low α and in the wing sections' wake turbulence levels for such types of serrated TE approach [29]. Llorente & Ragni used thicker airfoils for wind turbine applications and observed an increase in C_L in the models that included the serrated extension for maximum L [11].

2.1.3 *Low Re Airfoil Performance*

This thesis focused on the aerodynamic developments of wings at low *Re* regimes, ranging from 30,000 < *Re* < 200,000. These conditions were selected within the established parameters for small unmanned aerial vehicles (SUAV) [30]. The ongoing developments and the relative ease of implementation of serrated TEs in this scale were a key motivator of the work performed in this thesis.

This range of *Re* overlaps with some important special flow considerations that must be taken into account when studying the aerodynamic performance of wings. Starting with one that encompassed all cases studied in this thesis, research indicated that at *Re* < 500,000, the laminar boundary-layer separation had a significant impact on the wing's performance [15, 30, 31]. Lissaman described in his research that this was caused by an adverse pressure gradient being formed where the boundary layer was laminar [32]. The flow then reattached to the airfoil once it transitioned to being turbulent, with the space between separation and reattachment being referred to as a laminar separation bubble, as seen in Figure 2.5 [15, 32]. Such a phenomenon induced parasitic *D* [30].

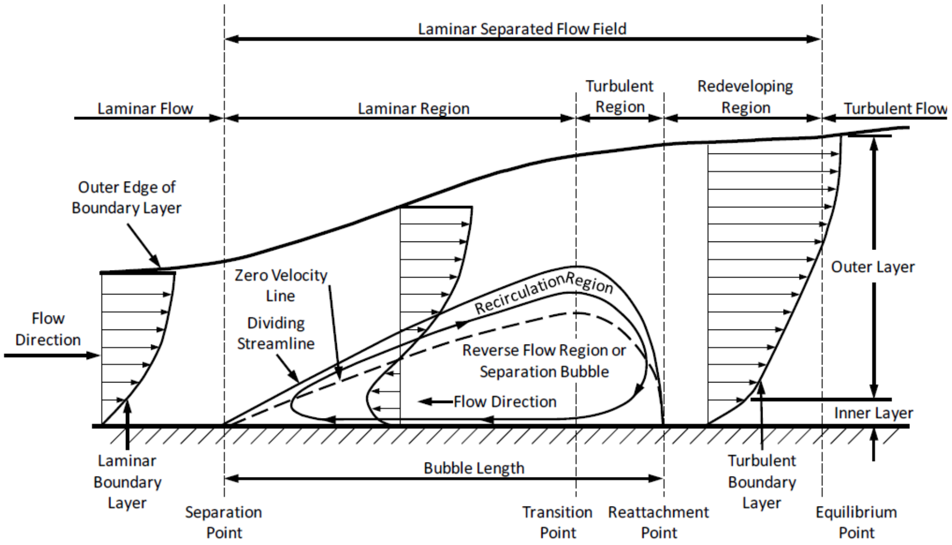

Figure 2.5. Laminar-turbulent transition and laminar separation bubble [33]

Between 200,000 < *Re* < 500,000, the bubble formation was small and, therefore, it presented the best aerodynamic indicators [30]. At a range of 70,000 < *Re* < 200,000, it was understood that the flow separation occurring near the LE intensified, and special considerations were needed for wing design [15]. At *Re* < 70,000, more specifically below 50,000, flow separation tended to not reattach over the surface of the wing, causing a drastic increase in the energy of vortex shedding, parasitic *D* and decrease in *L*, leading to stall at low *α* [30, 31, 32, 34]. Figure 2.6 illustrates the change in aerodynamic performance associated with variations to *Re* for a collection of wing profiles ranging including, among others, flat plates [35].

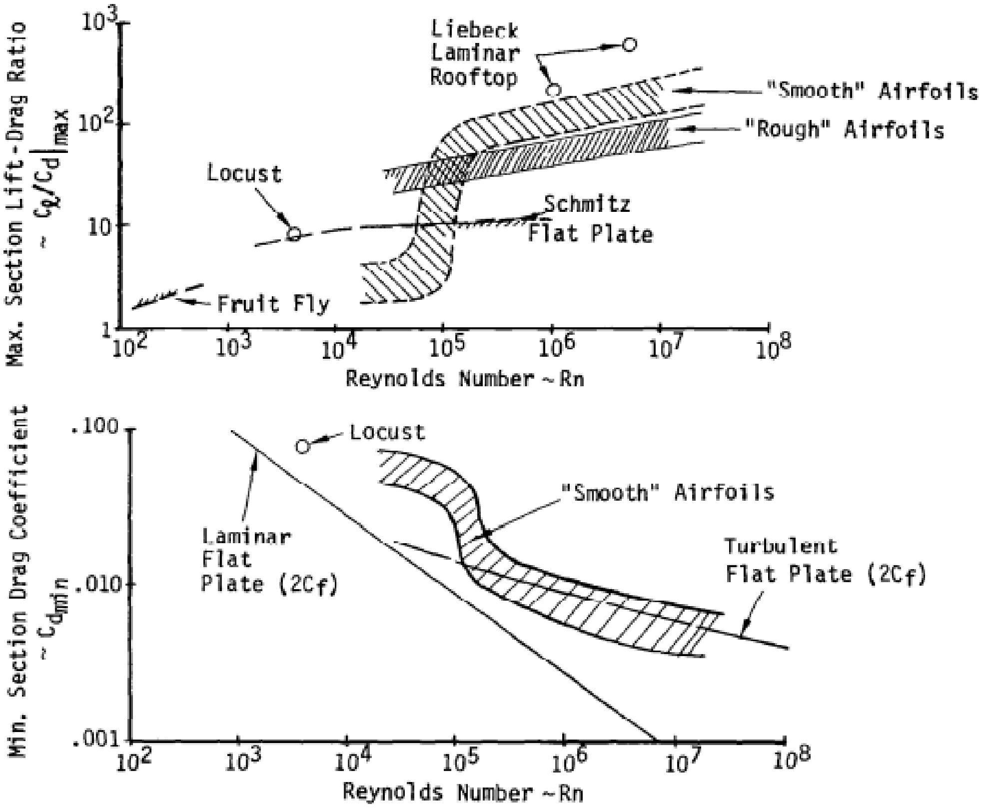

Figure 2.6. C_L/C_D (top) and minimum section drag (bottom) as a function of *Re* [35]

Based on this understanding, it was important to describe the flow using the equations of continuity and of momentum, according to an incompressible Navier-Stokes case [36].

$$\frac{d\rho}{dt} + \rho\nabla\cdot\mathbf{u} = 0 \tag{2.3}$$

$$\rho\frac{d\mathbf{u}}{dt} = -\nabla p + \rho\mathbf{f} + \mu\nabla^2\mathbf{u} \tag{2.4}$$

2.2 WIND TUNNEL THEORY

In his paper, Lissaman identified the challenges related to experimental testing at different Re [32]. Among them, wind tunnel testing was mentioned with difficulties including tunnel walls, model support effects, and incoming turbulence in the test section [32]. Similar issues were also discussed in Placek's work [37].

In their book, Barlow et al. explained the various considerations necessary while performing low speed wind tunnel testing [38]. The first point that deserved special attention was establishing proper flow similarity [36, 38]. For this thesis, the key parameter in analysis was *Re*, which allowed for comparisons between samples of different scales [36, 38].

$$Re = \frac{\rho U_{\infty} L}{\mu} \tag{2.5}$$

There are also different types of wind tunnels, with a key distinction being open and closed-circuit ones. A closed-circuit wind tunnel has air recirculating within a closed path [38, 39]. An open-circuit refers to wind tunnels that have an inlet and outlet which draw air from the outside environment, expelling once it completes its path— see Figure 2.7 [38, 39]. For this thesis, open-circuit wind tunnels were used given the access to facilities on campus employing this configuration. Under this context, however, it is important to mention the necessity for methods of reducing any non-uniformity of the flow within the test section, a phenomenon that can occur when using open-circuit wind tunnels. In this case, extensive flow screening devices, such as a honeycomb screen placed upstream from the test section, are typically required [38].

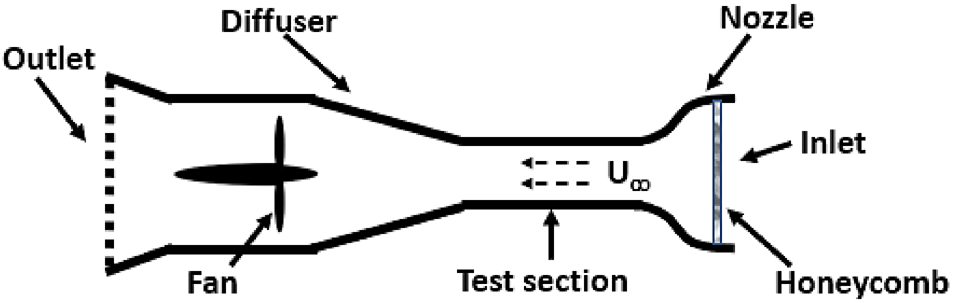

Figure 2.7. Open-circuit wind tunnel configuration

Additionally, there are some relevant wind tunnel effects that must be taken into consideration for this thesis given their potential impact on experimental results. For the purposes of this project, the ones considered were solid blockage, wake blockage and streamline curvature [38]. These were important considerations especially for the first part of this thesis's tests, which was subject to a higher blockage [38]. Solid and wake blockages relate to the confined space formed by the wind tunnel walls [38]. While the solid blockage is influenced directly by the ratio between a model's frontal area and the tunnel's cross section, the wake blockage uses the size of the wake as its metric — see equations below [38]. Additionally, the streamline curvature distortion refers to the different curvature of the flow bounded by a closed test section compared to a free-stream case [38]. Each one of these effects had an impact on the tests performed in this project. However, the solid and wake blockages were considered of primary relevance and measured during the experiments.

$$S.B. = \frac{A_{frontal}}{A_{c.s.}} \tag{2.6}$$

$$W.B. = \frac{A_{wake}}{A_{c.s.}} \tag{2.7}$$

2.3 WAKE SURVEY THEORY

Considering the theory behind the processes of analysis used in this thesis, it was important to understand how a wake survey method operates. This is a common technique for measuring profile *D* by focusing on the variation of the dynamic q_∞ measured using a combination of static and total pressure ports [40, 41, 42]. There are different ways of performing such a process, but all of them include measuring total and static pressure at regions sufficiently downstream from the model being studied [40]. Some of these configurations use a single pitot tube that traverses across a single line or even the entire 2-D cross-section [41]. This is called a traversing wake probe system and is illustrated in Figure 2.8 [41]. Others use a rake containing multiple probes that can simultaneously measure pressures across an entire profile, as seen in Figure 2.9 [41].

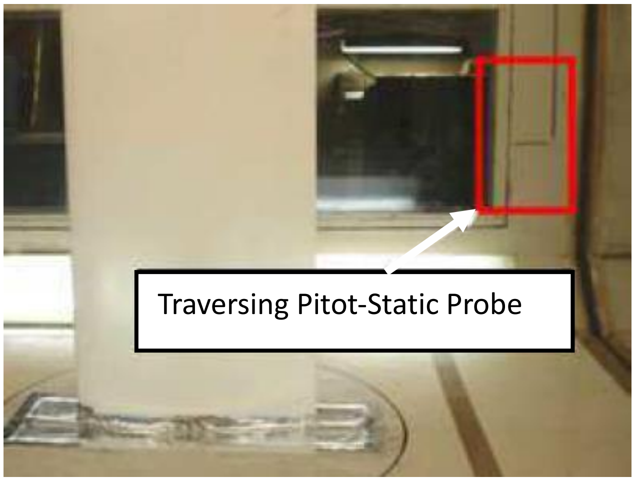

Figure 2.8. Traversing wake [41].

Figure 2.9. Wake rake [41].

The wake survey method is relevant for aerodynamic measurement as a technique that allows measuring a specimen's *D* without the use of a force balance. In order to do so, the total local pressure is subtracted by static pressure readings allowing for calculating local q_∞ in different points downstream from a sample [40, 42, 43]. As the flow moves past a specimen, a wake region is formed behind it, where the fluid loses momentum which causes a reduction in q_∞ [41, 42]. By transforming this data into local velocity measurements and integrating them across the cross section, it is possible to calculate C_D [43]. The equations below summarize this process [42, 43].

$$q_\infty = \frac{1}{2}\rho U_\infty^2 \tag{2.8}$$

$$C_d = \frac{2}{scU_\infty^2}\iint U(U_\infty - U)dA \tag{2.9}$$

It is important, however, to understand the limitations of the wake survey method. For instance, a wake survey does not provide information regarding flow directionality, resulting in the recommendation to take measurements far enough away from a model's TE [40]. This, however, cannot be excessively downstream as the gradient of velocity variation becomes weaker [40].

2.4 FORCE BALANCE THEORY

Measuring aerodynamic forces was a key objective of the experiments performed in this thesis. These forces allowed for a translation into non-dimensional parameters commonly used on scholarly aerodynamic studies, which were described previously in this chapter. It was, therefore, intrinsically important to determine the strategies and mechanisms used for measuring forces in such studies. These instruments are generally called force balances and may come in many configurations.

The major two types of force balances are internal and external ones. Internal force balances can be briefly described as a measuring device, generally named a sting balance, that is inserted into a model [44, 45]. Such a fixture is attached to a stand that anchors the system at different α [44, 45]. An external force balance uses fixed elements to transfer the loads from a sample to measuring devices, such as strain gauges, outside the wind tunnel [45]. In this thesis, the external force balance method was used due to its easier installation with thin models as compared to internal force balances.

A force balance is also classified by the number of component-forces and torques it is capable of measuring. Simpler models start with one or two-component force balances used to measure only a combination of L and D. Such is the case of the model proposed by Morris & Post which measure both forces [46]. The 3-component and the 6-component, however, are the most common versions of force balances, allowing measurement of M [45, 47]. These latter models were the types of force balances used in this thesis.

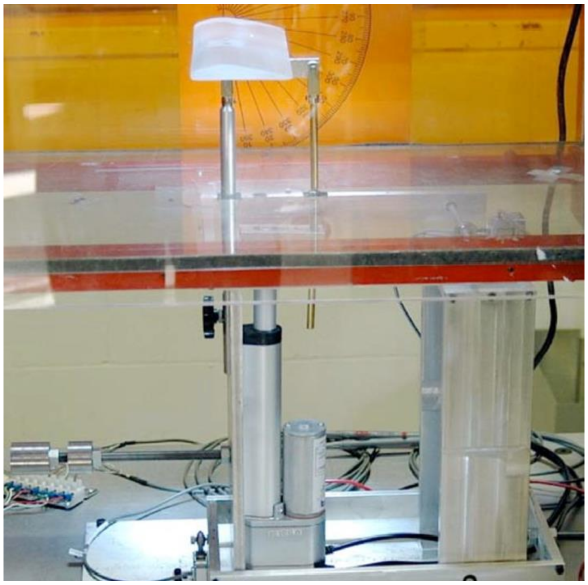

Figure 2.10. 2-component force balance [46].

As part of the work done in this thesis, a 3-component force balance was built (see Appendix A). Therefore, it was important to expand upon the theory behind this design. Multiple works have been written on the construction of an affordable balance using three uniaxial load cells [45, 47]. Two of these devices were connected to arms that linked the external balance to the model [45, 47]. Together, these two load cells provided information on L through a simple addition of its forces and M based on the sum moments about the leading edge of the model [47]. This is represented in the equations below, where F_1 and F_2 represent the vertical component, and F_3 the horizontal component of the forces [47]. The distance from LE and from the quarter point of the wing's chord length are, respectively, represented by (i) x_1 and x_2, and (ii) $x_{(c/4)1}$ and $x_{(c/4)2}$ [47]. At least one load cell was then placed to measure D in an arrangement that decoupled the forces [45, 47].

$$L = F_1 + F_2 \tag{2.10}$$

$$D = F_3 \tag{2.11}$$

$$M_{LE} = x_1 * F_1 + x_2 * F_2 \tag{2.12}$$

$$M = x_{\left(\frac{c}{4}\right)_1} * F_1 + x_{\left(\frac{c}{4}\right)_2} * F_2 \tag{2.13}$$

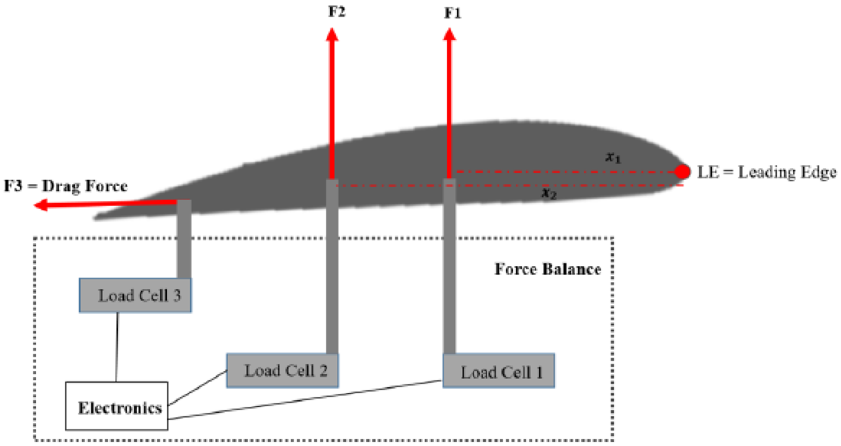

Figure 2.11. Simplified diagram of force balance system [47].

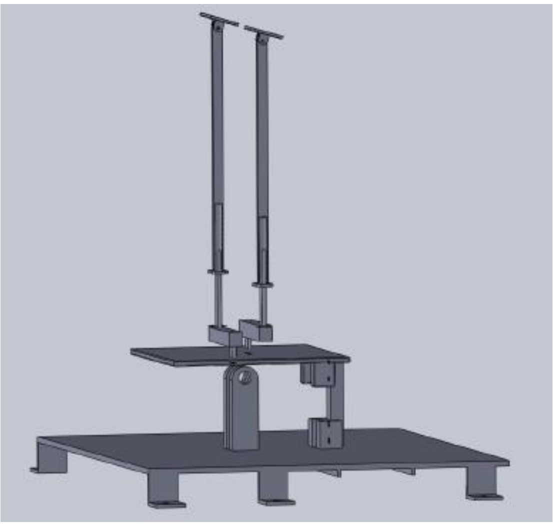

Figure 2.12. Example of design of 3-component force balance by Tintoré [45].

Chapter 3. DESIGN AND EXPERIMENTAL SETUP

3.1 RESEARCH PLAN

This thesis, as an experimental study, required a strategic approach to reduce the theoretically large array of test sample configurations to an acceptable and comprehensive set. For this purpose, the following plan was devised, outlining the scope of variables observed, preliminary screening system observations and final evaluation of the most promising samples.

Starting with the variables analyzed, the study focused on three metrics: (i) d, (ii) λ and (iii) shape of serration. Various configurations were then selected to represent the initial test sample group, a small subset of an endless array of options used to showcase the changes on the wing sections' aerodynamic performance. This step was part of the screening system devised to reduce the number of samples from the initial larger group to a small one used for a detailed comparative study based on C_L, C_D and C_M. At this initial phase, however, greater focus was given to the analysis of the effects on C_L, C_D and from the velocity field downstream of each sample. This was done by isolating and analyzing one variable at a time.

The best performing combination of d and λ proportions in reference to c was, then, used to create a smaller sample group used for deeper investigation with samples at a larger scale and higher Re. The focus in this section shifted to serration topology with shapes ranging from a conventional triangular serration to quadratic parabolic ones (bird feather-like and membrane-like serrations), and tapered TEs. For an array of α and Re, an in-depth study was performed on the aerodynamic characteristics of each wing section with the goal of identifying the best combination of all parameters. This insight was also intended to help guide future works focused on continuing the optimization of aerodynamic serrations for the small unmanned aerial vehicle segment, based on quantitative and qualitative results.

A detailed schematic portraying the research plan is provided in Figure 3.1.

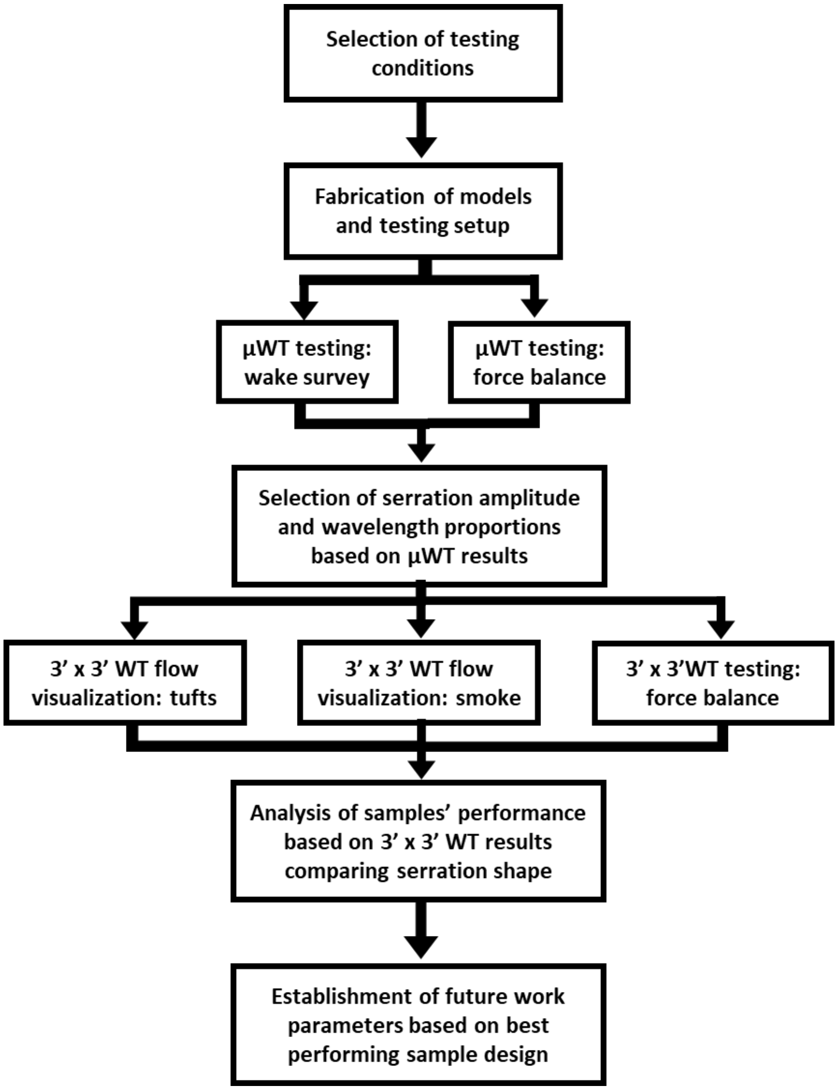

Figure 3.1. Schematic of Research Plan.

3.2 ASSUMPTIONS

In order to complete the analysis of this thesis, it was important to establish a series of engineering assumptions. As a part of low-speed fluid mechanics, the cases studied were considered to involve an incompressible flow. Another consequence of the very low subsonic flow speeds was that viscosity effects represented a critical component in the interaction between the bodies investigated and air, something that reflected into a thicker boundary layer.

Mechanical assumptions were also required for the calculations of the forces through the model and structures developed during this thesis. All parts were assumed to be rigid bodies. Such a consideration implied that torques and forces applied to the samples were transferred to load cells, with negligible losses. Furthermore, it was important to state that the room conditions, such as temperature and humidity at the lab facilities for the micro wind tunnel (µWT) and 3’ x 3’ wind tunnel (3’ x 3’ WT), were stable and their results were transferrable and comparable.

3.3 MICRO WIND TUNNEL (µWT)

As mentioned previously, a first set of experiments was performed at a µWT with a 3” x 3” test section (see Figure 3.2). These tests were done to narrow down the variables to be more thoroughly evaluated at higher scale and *Re*. The tests at the µWT were divided into two methods: wake survey and force balance measurements. The description of their experimental setup is presented below.

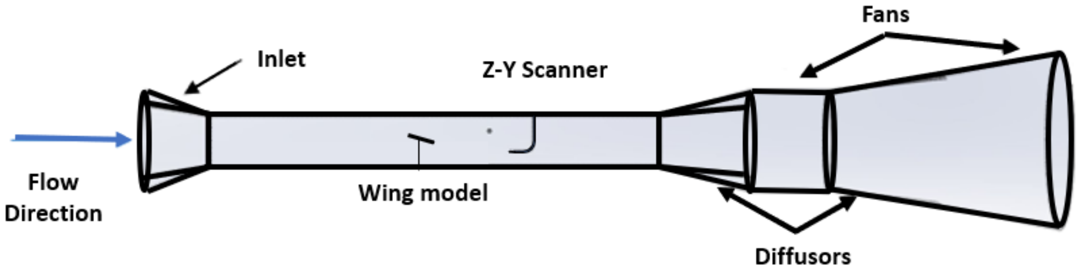

Figure 3.2. µWT schematic.

3.3.1 *Experimental Setup*

The µWT was set to operate at a *Re* ≈ 30,000 ($U\infty = 9$ m/s). Considering the setup for the wake survey measurements, the wing sections were attached to a series of slots in the wind tunnels’ walls, adjustable according to a series of α — 0°, 5°, 10°, 15°, and 20° (see Appendices A and B). A pressure sensor scanner was used to collect data with the help of a LabVIEW program that controlled a pitot tube located at 1.5 x *c* behind the wing section's TE [48]. This pitot tube was able to traverse across a 30 x 30 grid (0.095 m x 0.092 m) in the *y*- and *z*-direction (see Figure 3.3). A static pressure tube was placed downstream from the specimen, and both pitot tube and static pressure tube interfaced together through an Arduino Uno, capable of measuring 1000 samples per second. The sensor used for data collection was an Omega PX409 with a pressure capacity of 2500 PA. This setup allowed for the examination of the wing sections' wake. These data were, then, imported into a MATLAB program responsible for post processing of the pressure data and converting it into C_D through the wake survey method (See Appendix C).

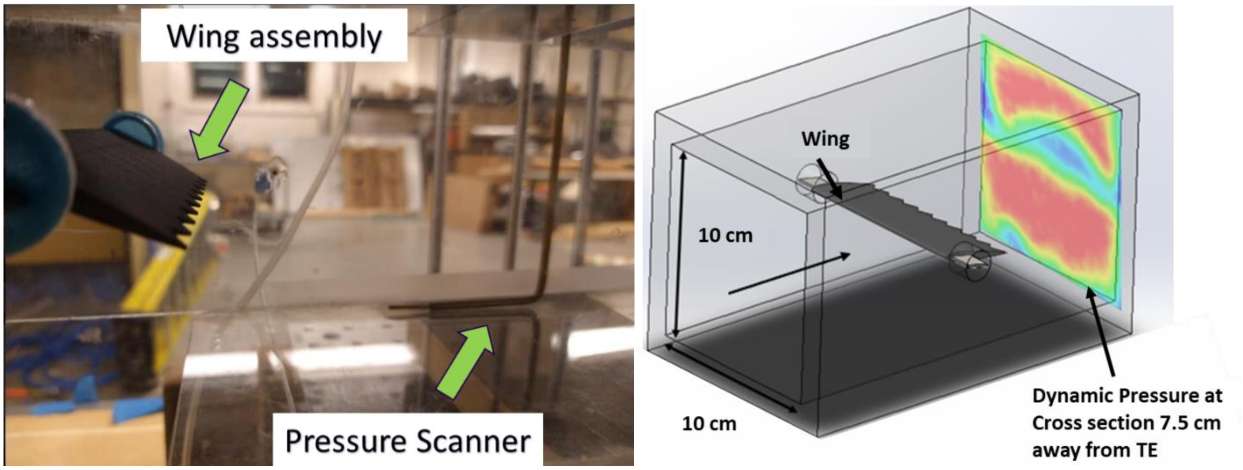

Figure 3.3. Setup for wake survey [1].

The force balance section of the screening process considered a 3-component instrument based on Tintoré's design [45] (see Appendices A and B for additional setup diagrams). Two vertical arms would enter the wind tunnel through its floor and the models were mounted onto them. The frontal arm was fixed while the rear one was adjusted manually, allowing the samples' α to range from 0° to 15° in increments of 5° (see Figure 3.4). These connected to two load cells, one for each arm, through a connecting piece. These two load cells were responsible for measuring *L* and *M* as seen in Figure 3.5.

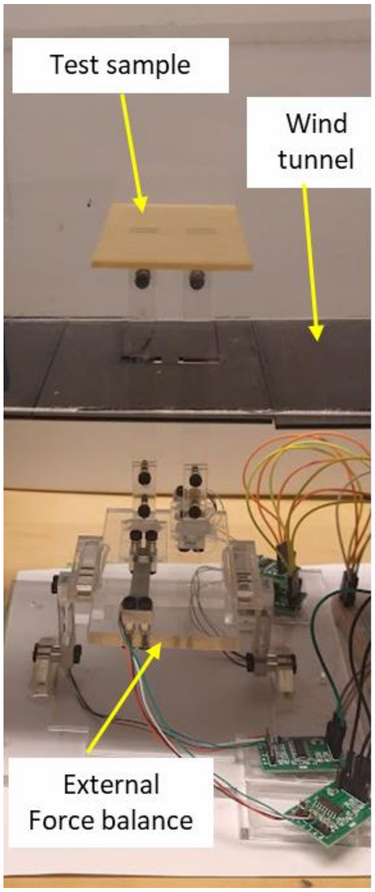

Figure 3.4. Setup for 3” x 3” force balance testing.

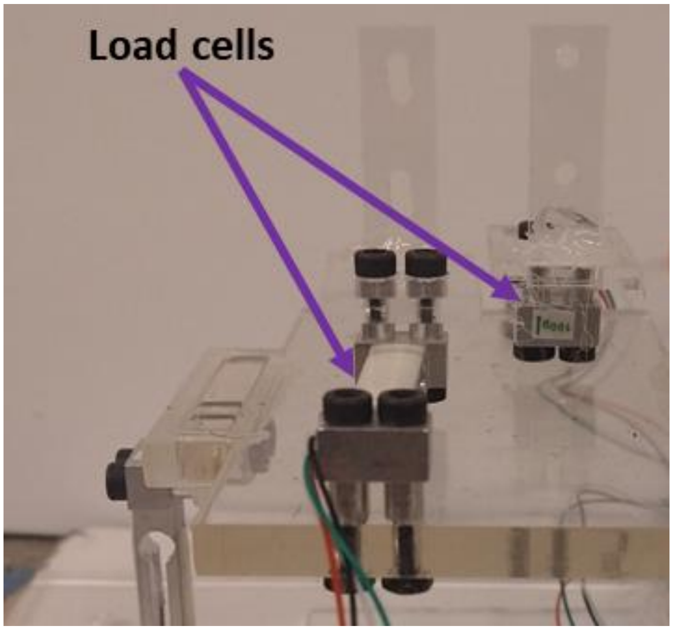

Figure 3.5. Upper section of force balance.

The two load cells were held steady by an intermediate horizontal platform. Such a platform was designed to be a stiff component that interfaces with a set of two more load cells that were placed vertically and attached to the base of the entire system. These two load cells were used to measure *D*. Although it was possible to use only one load cell in this section, the use of two load cells at the opposite ends of the force balance allowed for a symmetric system and a more even transfer of loads across it (see Figure 3.6).

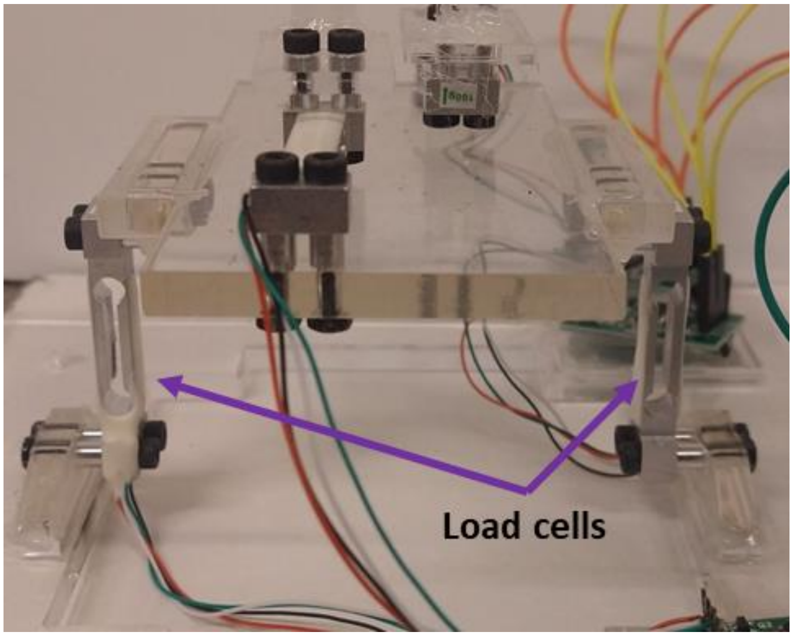

Figure 3.6. Lower section force balance.

All load cells had a maximum load capacity of 1 N with a resolution of ± 1 mN which was then paired with a HX711 load cell amplifier. At each α, load data was collected and then converted into C_L, C_D and C_M with the help of an Arduino Uno and an Arduino IDE program adapted for the specifications of the current system—see Appendix D [45].

The interfacing pieces for this force balance were made from acrylic with different levels of thickness due to its low cost and desired mechanical properties, advantageous for the loads considered in this series of tests. All these parts were fabricated using an Epilog fusion M2 laser cutter, as it allowed for the accuracy and consistency these pieces required for ideal load transferring. The 3-component force balance is seen in Figure 3.7.

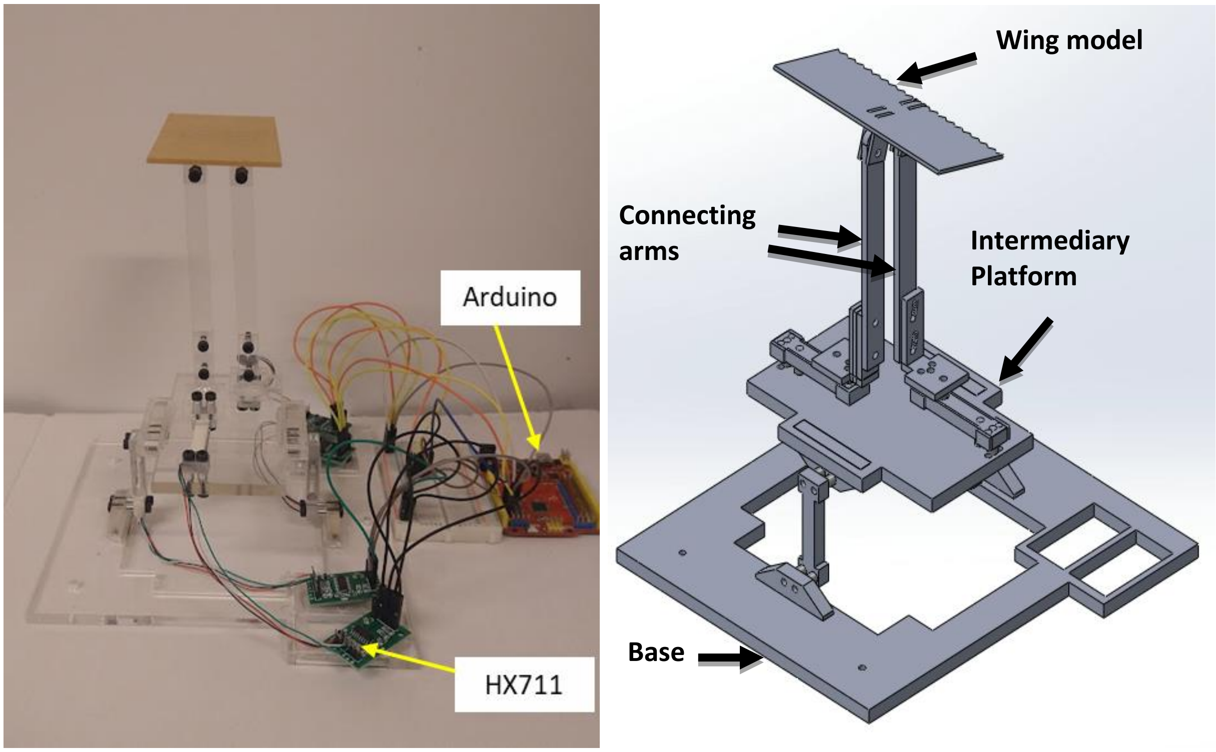

Figure 3.7. Fully assembled force balance.

3.3.2 *Design and Fabrication of Test Samples*

MAVs commonly use a thin wing profile, and thus, a thin flat plate wing section with a $t/c \approx 3\%$ was selected [15, 49]. As described previously, 3 metrics were used as variables for the remainder of the thesis: (i) d, (ii) λ and (iii) shape of serration. The first two were non-dimensionalized, becoming a function of the wing's maximum chord length (c) for practicability across different testing platforms and samples. There were three serration shapes implemented: (i) triangular, (ii) membrane-like, and (iii) bird feather-like. In total, the number of initial test samples is 8, which are described in Table 3.1 and Figures 3.8-9. They were manufactured using an Epilog Fusion M2 32 laser cutter for precision and consistency.

Table 3.1. µWT wing section dimensions.

Wing ID	**Wind Tunnel**	**Wing Type**	**c [m]**	**s [m]**	**t [m]**	**λ [m]**	**d [m]**
W1	µWT	Flat Plate	0.05	0.10	0.0015	—	—
W2	µWT	Triangular	0.05	0.10	0.0015	0.005	0.0025
W3	µWT	Triangular	0.05	0.10	0.0015	0.005	0.0050
W4	µWT	Triangular	0.05	0.10	0.0015	0.005	0.0100
W5	µWT	Triangular	0.05	0.10	0.0015	0.010	0.0050
W6	µWT	Triangular	0.05	0.10	0.0015	0.020	0.0050
W7	µWT	Bird Feather	0.05	0.10	0.0015	0.005	0.0050
W8	µWT	Membrane	0.05	0.10	0.0015	0.005	0.0050

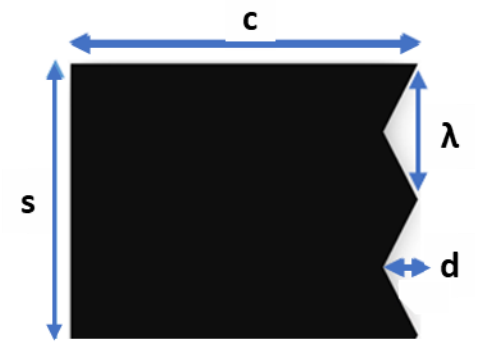

Figure 3.8. Diagram of wing sample's dimensions.

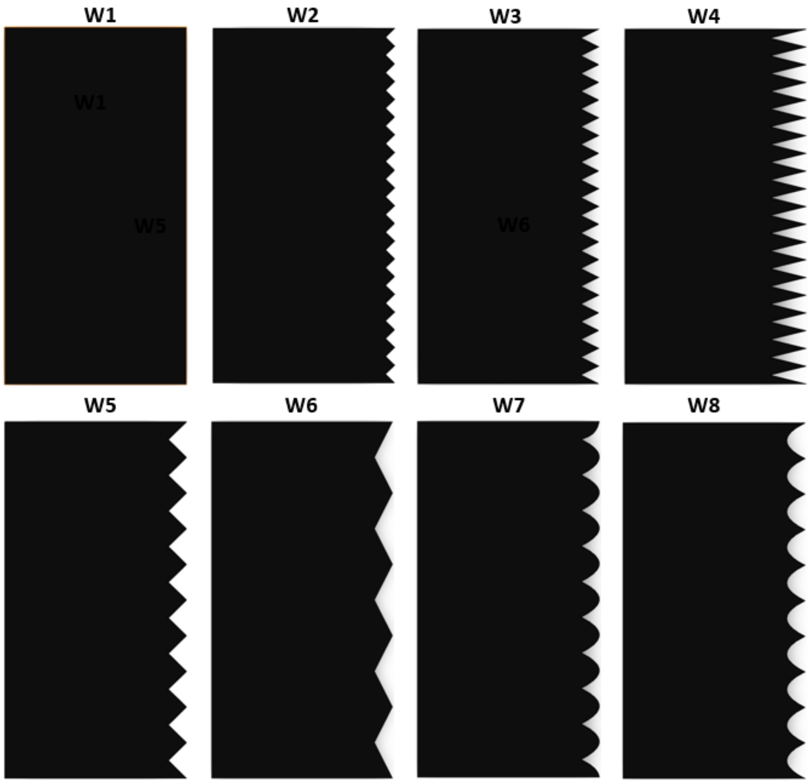

Figure 3.9. µWT wing sections [2].

3.4 3’ X 3’ WIND TUNNEL (3’ X 3’ WT)

The 3’ x 3’ WT tests followed the μWT’s screening process, focusing on the effects of the shape of serration. They were comprised of two sets of experiments: aerodynamic load measuring and flow visualization (see Figure 3.10). This open-loop facility has a test section of 0.91 m (3 ft) x 0.91 m (3 ft) x 2.44 m (8 ft) and a wind speed capacity ranging from 15 m/s to 60 m/s [50].

Figure 3.10. 3’ x 3’ WT.

3.4.1 *Experimental Setup*

In order to perform the experiments, an ATI F/T Sensor: Mini45 load cell was used. This instrument is capable of measuring 6 components, 3 forces and 3 torques, and was fitted above a platform that allows for 360˚ rotation (see Figure 3.11). The force balance’s sensing ranges and resolution is seen in Figure 3.12.

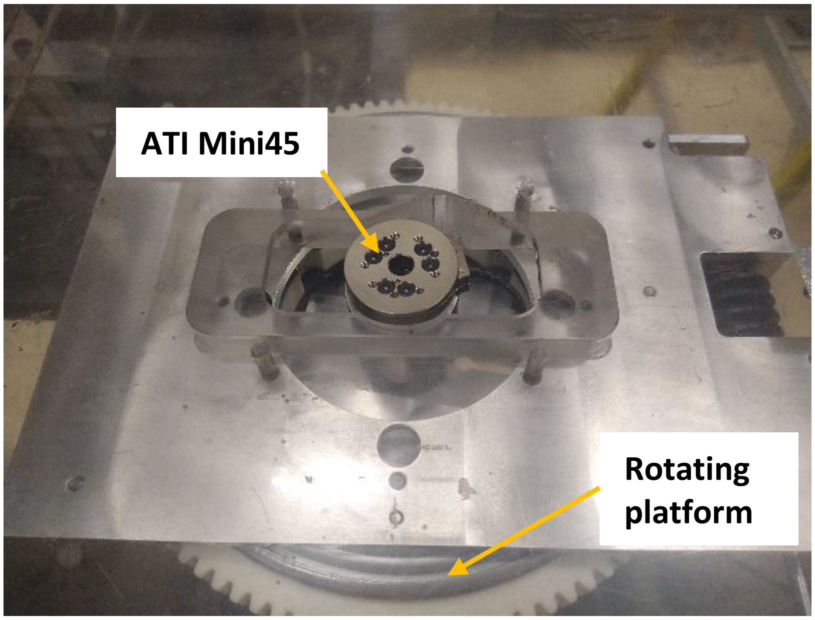

Figure 3.11. ATI F/T Sensor: Mini45 platform [2].

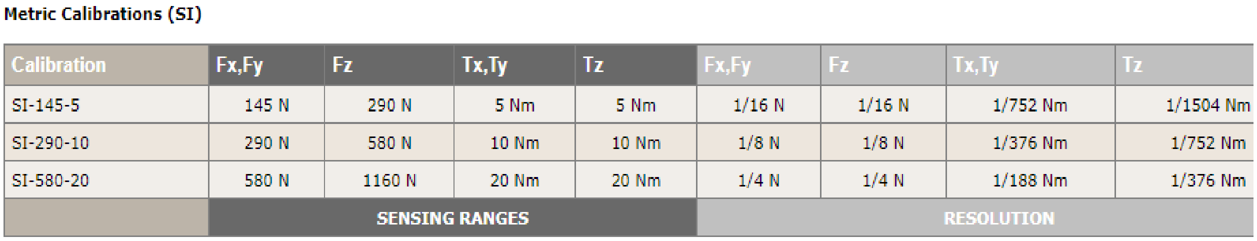

Metric Calibrations (SI)

Calibration	Fx,Fy	Fz	Tx,Ty	Tz	Fx,Fy	Fz	Tx,Ty	Tz
SI-145-5	145 N	290 N	5 Nm	5 Nm	1/16 N	1/16 N	1/752 Nm	1/1504 Nm
SI-290-10	290 N	580 N	10 Nm	10 Nm	1/8 N	1/8 N	1/376 Nm	1/752 Nm
SI-580-20	580 N	1160 N	20 Nm	20 Nm	1/4 N	1/4 N	1/188 Nm	1/376 Nm
	SENSING RANGES				RESOLUTION			

Figure 3.12. Sensing Ranges and Resolution of ATI F/T Sensor: Mini45 [51].

The test samples were mounted vertically above the ATI Mini45, with an interface tool using M3 fasteners to connect with the force sensor and M8 fasteners for the interface/wing attachment (see Figure 3.13 and Figure 3.14). This assembly was set to range in *Re* between 100,000, 150,000, and 200,000. The samples' α was set to vary between 0° and 30° in increments of 2.5°.

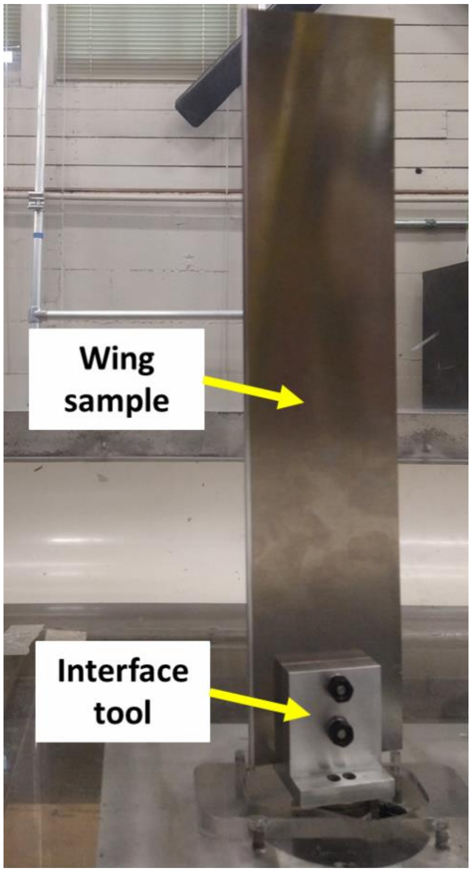

Figure 3.13. Setup for 3’ x 3’ wind tunnel testing with interface tool.

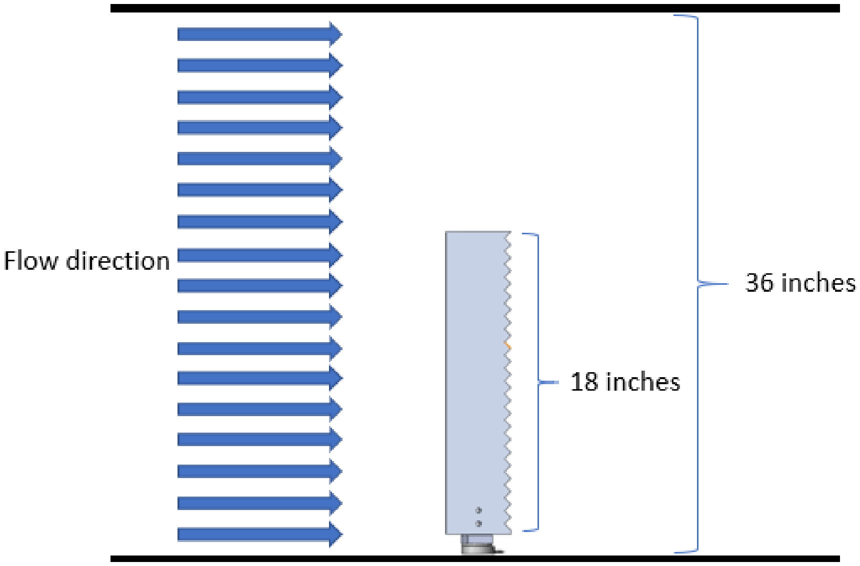

Figure 3.14. Schematic of test setup for 3’x 3’ WT testing [2].

A qualitative set of tests performing flow visualization was also done using the same general experimental setup. Two methods were used for visualization. The first was comprised of two rows of tufts located across the wing sections for consideration throughout the specimens' surface. The second used a smoke machine aided by a laser sheet for 2-D planar observations of the flow past each wing section (see Figure 3.15).

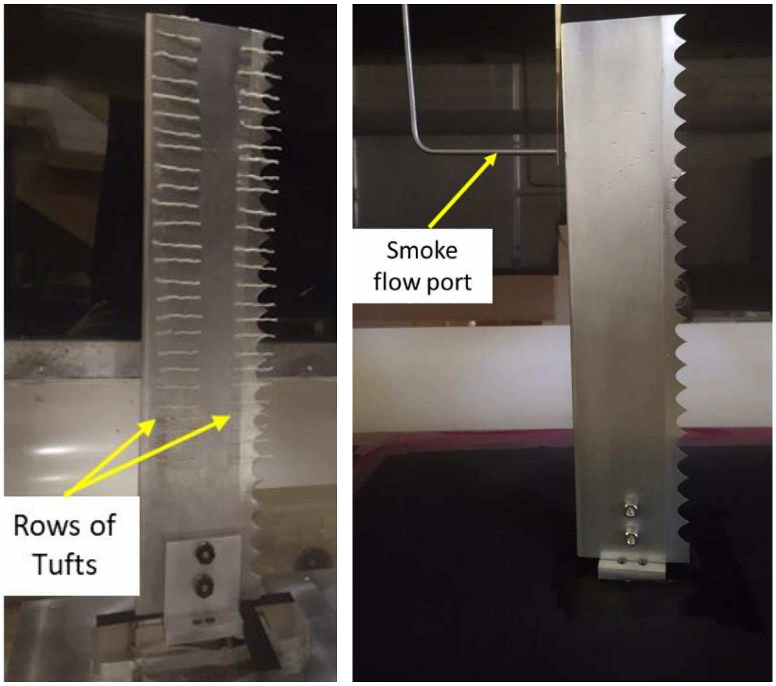

Figure 3.15. Flow visualization setup with tufts attached (left) and smoke (right).

3.4.2 *Design and Fabrication of Test Samples*

The larger wing samples used for the 3' x 3' WT were manufactured through CNC machining, using aluminum 2024 alloy given its appropriate properties to endure the loads applied to the mechanism. An image illustrating the process of fabrication of the larger wing section models is presented at Figure 3.16.

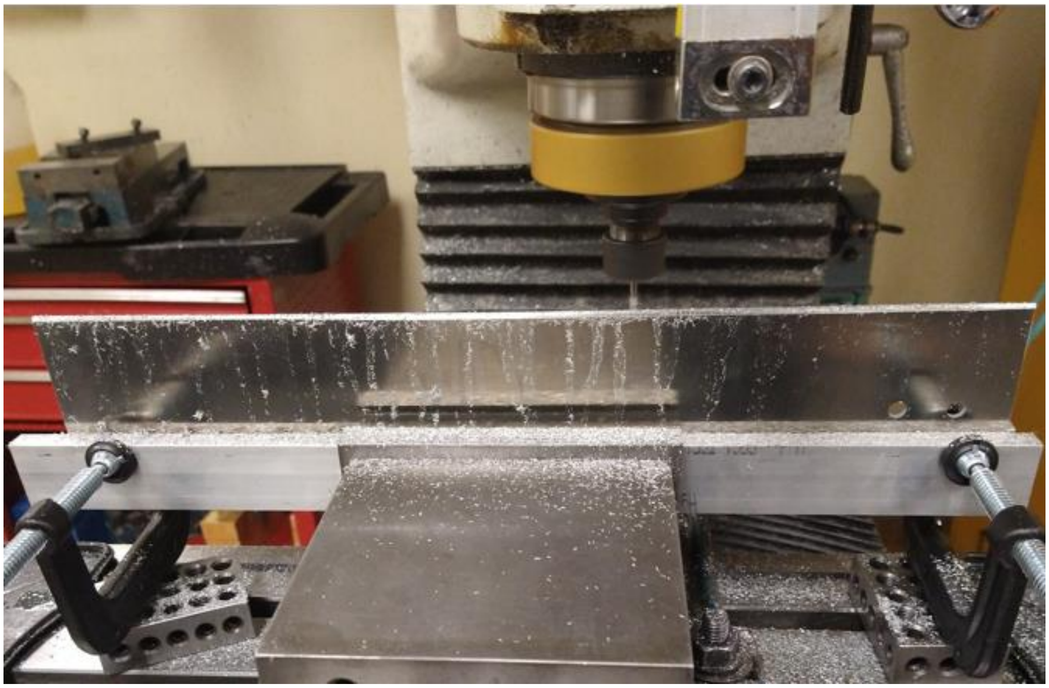

Figure 3.16. Larger wing section CNC manufacturing.

There were 5 wing samples in total, identified as W9 through W13 (see Figure 3.17). The main dimensions common to all wings are described in Table 3.2. W9 represented a control sample flat plate. W10, W11 and W12 represented, respectively, the triangular, bird feather and membrane serration shapes. W13 combined a tapered TE and a membrane-like serration. The dimensions related to the serrations are described in Chapter 5, since *d* and *λ* were defined based on the proportions of the μWT wing sample that yielded the most promising results.

Table 3.2. 3’ x 3’ WT wing section dimensions.

c [m]	**s [m]**	**t [m]**
0.10	0.45	0.0030

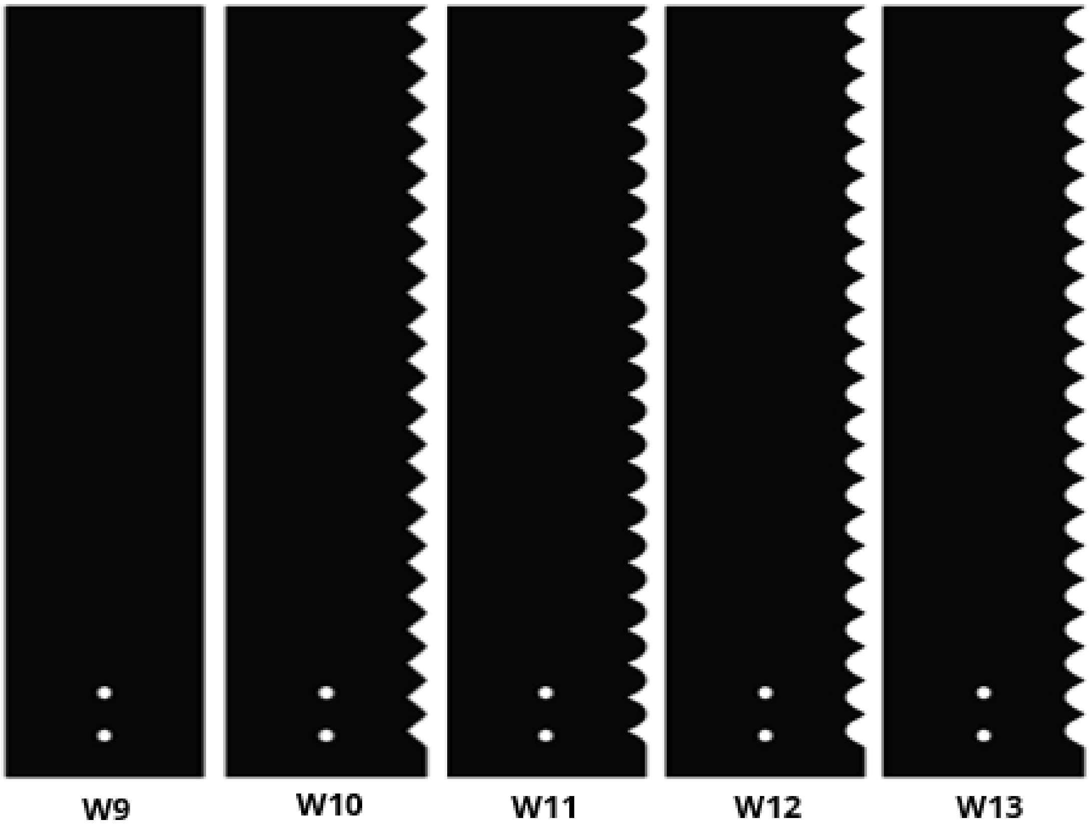

Figure 3.17. Wing specimen concepts for 3’x3’ WT [2].

3.5 SETUP SUMMARY

Table 3.3 presents a summary of the experimental test plan and setup described in this chapter. This was divided into two stages related to the experiments run at the μWT and 3’x3’ WT, in this respective order. The testing types conducted, variables considered, and test samples are also described.

Table 3.3. Testing plan summary matrix.

Stage	**Wind Tunnel**	**Testing Type**	**Testing Variables**	**Serration Variables**	**Wing Samples**	**Sample Description**
1	μWT	Wake Survey	$Re \approx 30{,}000$ $0^\circ \le \alpha \le 20^\circ$ (increments of 5°)	Shape Wavelength (λ) Amplitude (d)	W1	Flat plate baseline
					W2	Triangular d: shallowest λ: narrowest
					W3	Triangular d: intermediate λ: narrowest
					W4	Triangular d: deepest λ: narrowest
		Force balance measurements	$Re \approx 30{,}000$ $0^\circ \le \alpha \le 15^\circ$ (increments of 5°)		W5	Triangular d: intermediate λ: intermediate
					W6	Triangular d: intermediate λ: widest
					W7	Bird feather
					W8	Membrane
2	3’x3’ WT	Flow visualization with tufts	$Re \approx 100{,}000$, 150,000 and 200,000 $0^\circ \le \alpha \le 30^\circ$ (increments of 2.5°)	Shape	W9	Flat plate baseline
					W10	Triangular
		Smoke flow visualization			W11	Bird feather
					W12	Membrane
		Force balance measurements			W13	Membrane + tapering

Chapter 4. µWT RESULTS AND ANALYSIS

The µWT primarily functioned as a screening system for the tests performed at the 3' x 3' WT. These low-speed tests (*Re* ≈ 30,000) also proved to be relevant for understanding the potential applications of serrations as technological progress allows for even smaller aerial vehicles. It is worth noting that, due to the small dimensions of this wind tunnel, solid blockage affected these samples' performance, reaching a maximum of 17% at $\alpha = 20°$. All specimens, however, experienced approximately the same levels of blockage effects. Thus, a comparison between them at the various α still provided valuable information as to the capabilities of each different serration model compared to the baseline W1. Two sets of experiments were performed using this system: wake survey and force balance measurements. Sections 4.1.1 and 4.2 expand upon topics previously explored in the research performed by Bron Simplicio et. al. [2].

4.1 WAKE SURVEY METHOD

4.1.1 *Velocity Contours*

The wake survey method employed at the µWT provided two outcomes: a visualization of the flow downstream of the wing's TE and an initial estimate on the C_D of each model. Figure 4.1 portrays the former case by showing a comparative observation of the velocity cross sections between a flat plate wing section (W1) and three serrated wing sections: W5, W7 and W8. Three main portions were noticed in the plots: (i) two red regions of high energy flow representing the freestream regions, (ii) a central lower speed section related to a wing's wake, and (iii) two lower energy flow segments located at the *y*-coordinate's extremities linked to the tunnel walls' boundary layer. In general, these plots showed no clear visual contrast between the different wing sections' flow characteristics that could be attributed to positive or negative impacts from the serrations. Therefore, more quantitative measurements were needed for a better analysis in search of optimal serrated TE configurations.

There were, however, key instances worth mentioning in the flow development as the wings' α changed. Starting at low α (up to 5°), the wake revealed a flow that was overall characterized by its 2-D behavior with a narrow rectangular wake region. This was evident by considering that the darker (red) high energy flow portions representing the freestream flow uniformly covered most of the upper and lower sections of the plots. This regularity in the wake at low α was seen at all wing sections tested, suggesting that the flow was attached.

At higher α, the wake region became characterized by a growing arched shape. This depicted a significant increase in the flow's wake region and a worsening of the wing's aerodynamic performance, signs of flow separation. Likewise, there was a reduction in the tunnel walls' boundary layer thickness induced by a noticeable increase in flow blockage at higher α due to the test section's small size. Solid and wake blockages, which reached a maximum of about 17% and 33% respectively, were responsible for a flow compression against the wind tunnel walls and, consequently, a wall boundary layer thickness reduction.

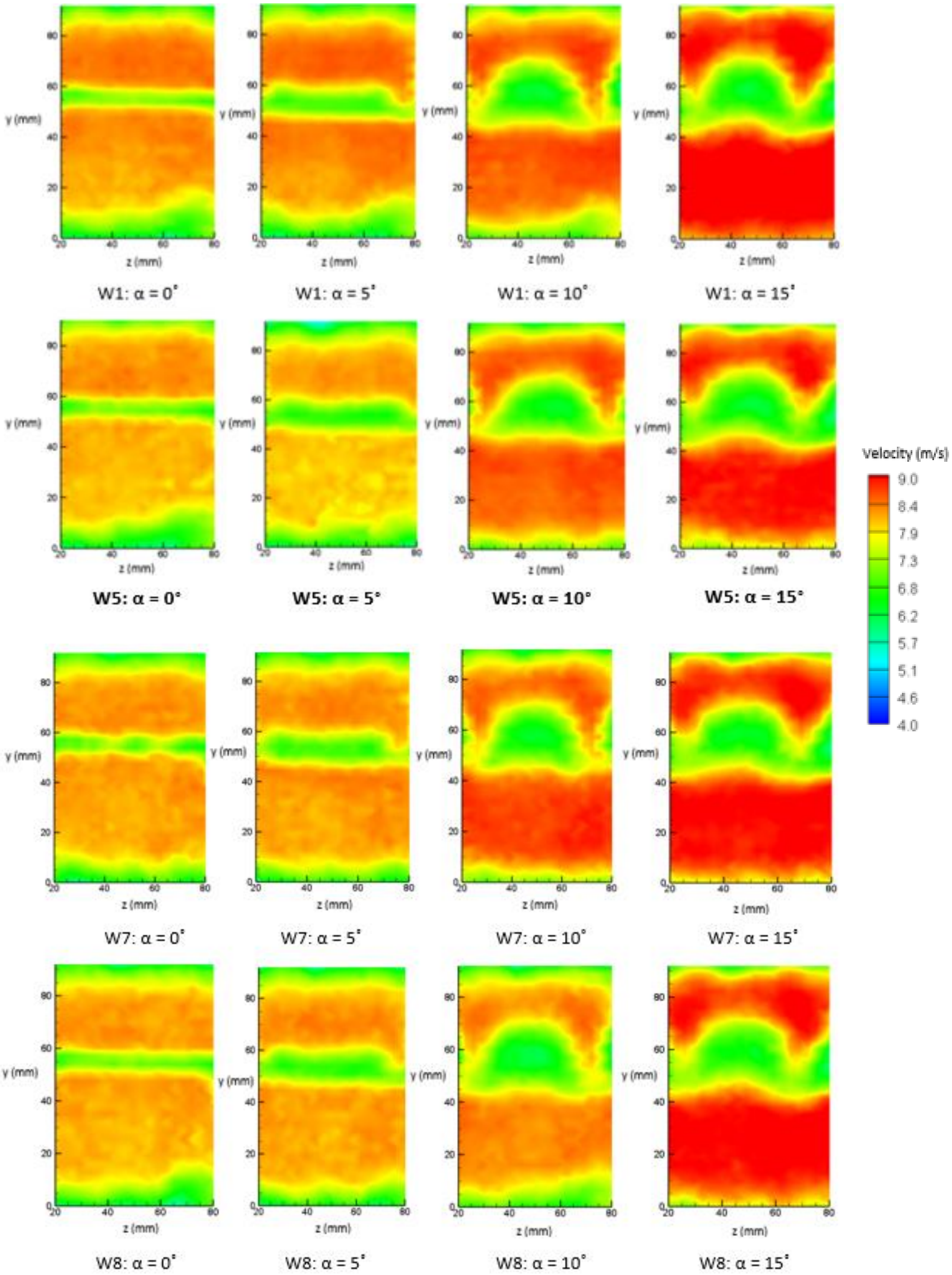

W1: α = 0° W1: α = 5° W1: α = 10° W1: α = 15°

W5: α = 0° **W5: α = 5°** **W5: α = 10°** **W5: α = 15°**

W7: α = 0° W7: α = 5° W7: α = 10° W7: α = 15°

W8: α = 0° W8: α = 5° W8: α = 10° W8: α = 15°

Figure 4.1. µWT velocity contours in W1, W5, W7 and W8’s wake (not at scale) [2].

4.1.2 *Coefficient of Drag Estimates Derived from Wake Survey*

The C_D estimates through wake survey represented a first attempt at quantitatively understanding the effects of implementing serrated TEs. A MATLAB program was used to transform individual pressure data points into C_D according to the equations mentioned in Chapter 2 (see Appendix C). This method didn't show a noticeable C_D reduction related to the presence of serrations when compared to W1. In fact, most of them displayed a small increase in C_D over the angles considered. Three plots were made and showed a comparative analysis based on the main serration variables: d, λ and shape.

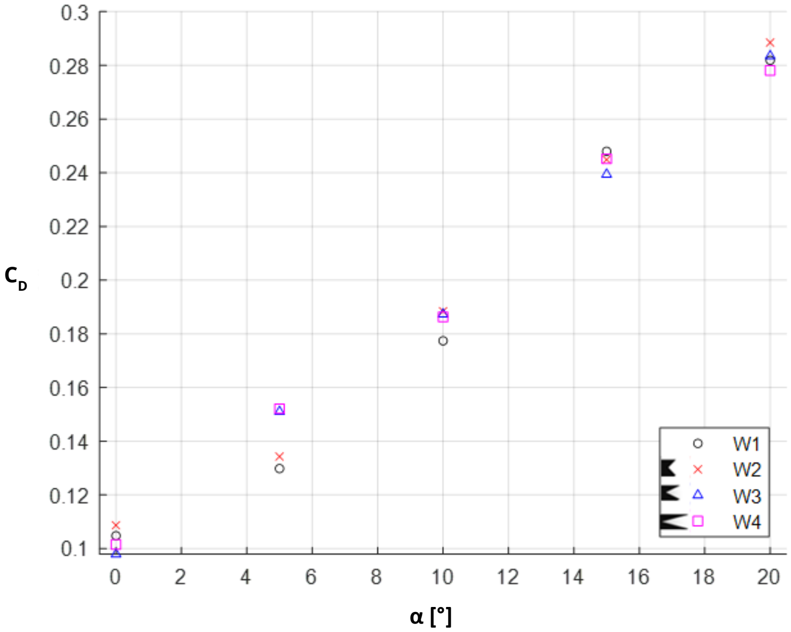

Figure 4.2. Comparison of C_D based on d, $Re \approx 30{,}000$

In relation to the d comparison, it was possible to observe that the shallower serration seemed to indicate a better drag performance at lower α (<10˚). This could be especially seen at $\alpha = 5^\circ$ where there was a 13% difference in C_D between W2 and W4, using W1 as a reference (see Figure 4.2). W2's C_D was 3.5% higher than W1's, while W4's was 17% higher. At greater α, the deficit in C_D reduced when compared to the baseline, W1. W3, with its d representing 10%

of *c* (the intermediate case), became the best performing out of the three serrated models considered.

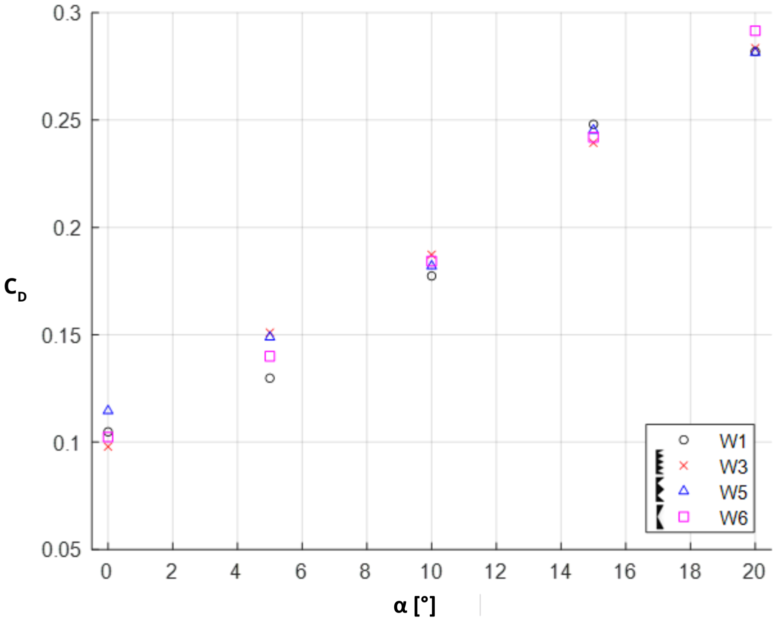

Figure 4.3. Comparison of C_D based on λ, $Re \approx 30,000$

Second in consideration, λ was tested with 3 different models corresponding to 10%, 20% and 40% of *c* (see Figure 4.3). Again, a difference was noticed between lower and higher α. At $\alpha < 10^\circ$, the wider serrations, represented by W6, yielded the best results with a 7% difference to W5 at $\alpha = 5^\circ$. W6's C_D was 8% higher than W1's, while W5's was 15% higher. At $\alpha \leq 10^\circ$, W5, with its intermediate λ, proved to most consistently yield the best results. However, at this range, all samples' C_D performances were close to one another.

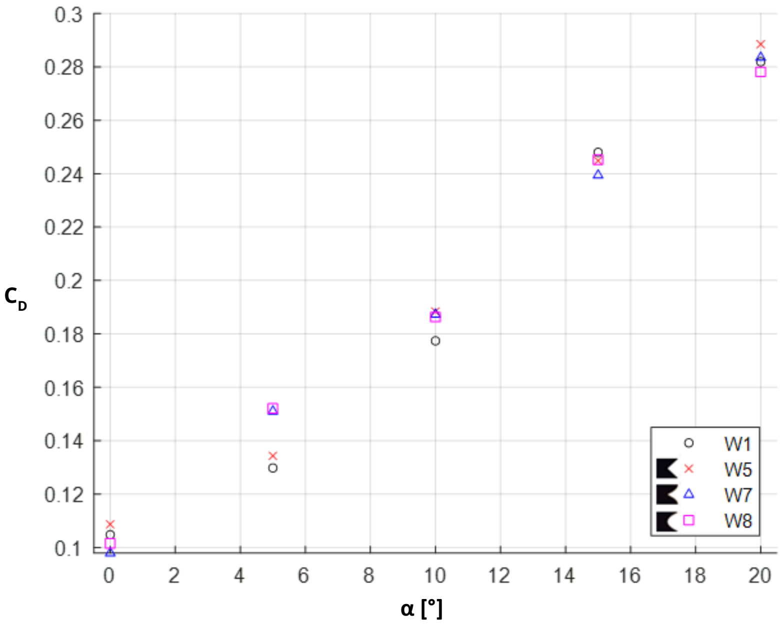

Figure 4.4. Comparison of C_D based on serration shape, *Re* ≈ 30,000

Overall, however, serration shape was the variable that most impacted the C_D (see Figure 4.4). Using W5 as reference for λ and d, the bird feather-like shape, W7, and the membrane-like serration, W8, were built. Among them, W7 proved to yield the best C_D performance across all α. W7 was also estimated to be consistently the best of all 8 wing samples including the base model. Furthermore, it was interesting to note that both the membrane and the bird feather TEs, with their curvilinear serrations, exhibited better results than the triangular shaped one in most α considered.

4.2 FORCE BALANCE

Given that the wake survey method only provided an estimate of the C_D, a series of force balance tests were performed aiming to further the understanding of serrated wing sections' performance at this range of *Re*. For this case, α was set to range from 0° to 15° in increments of 5° and at a U_∞ = 9 m/s ($Re \approx 30{,}000$). Since this instrument allowed for the collection of C_L, C_D, and C_M data, it was possible to draw additional comparisons while maintaining the same structure of analysis divided into (i) *d*, (ii) λ and (iii) shape of serration. The plots presented in this section show an average of the data gathered for each α throughout its collection duration, while the vertical bars associated with them represented the standard deviation of time-dependent fluctuations in their respective dataset.

Starting with *d* comparisons, when considering C_L/C_D, the deepest serrations represented by W4 caused a significant reduction in performance, accounting for a 15% drop compared to the W1 (baseline) at $\alpha = 10^\circ$ and $\alpha = 15^\circ$ (see Figures 4.5 and 4.6). It was possible to determine, then, that an excessive *d* (~20% of *c*) correlated to a significant negative impact on wing section aerodynamics. Upon further inspections of the individual parameters, it was noticed that the reduction in performance was mostly due to a decrease in C_L with a minor increase in C_D. This could be attributed to the streamwise vortices being introduced further upstream from the TE and, therefore, impacting the pressure gradient between the pressure and suction surfaces of throughout a larger portion of this wing section. W3, with its 10% *d* ratio in relation to its chord length, yielded better results at $5^\circ \leq \alpha \leq 10^\circ$ (see Appendices E, F and G). Regarding the effects of *d* on C_M, no clear trend could be identified as to whether it could be accounted for a specific change. Nonetheless, most indicated a decrease in stability (see Figures 4.7 and 4.8).

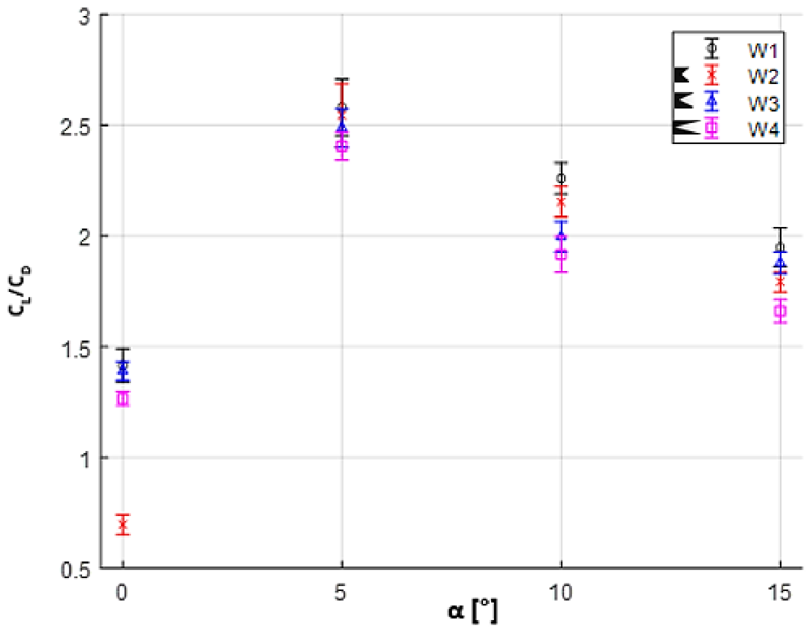

Figure 4.5. C_L/C_D based on *d*, *Re* ≈ 30,000

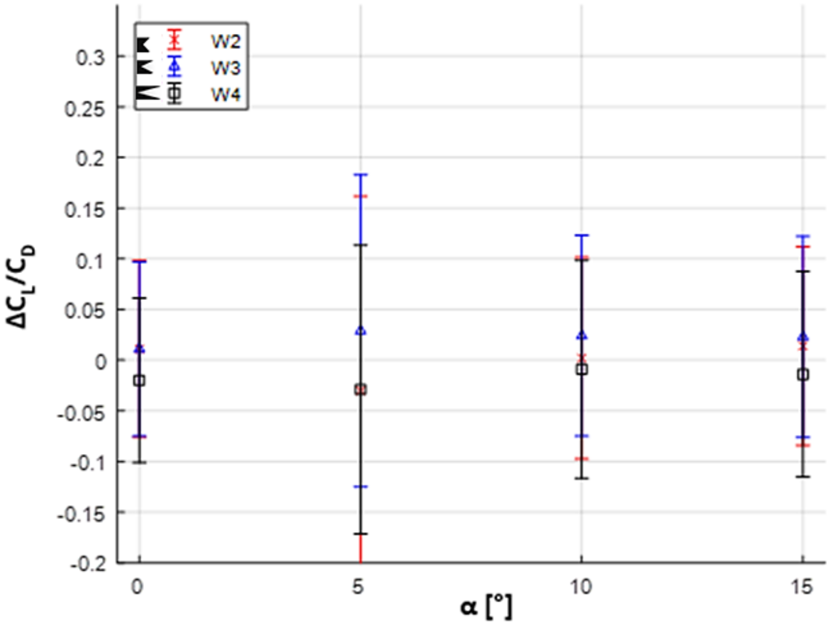

Figure 4.6. $\Delta C_L/C_D$ based on *d* (serrated samples – W1), *Re* ≈ 30,000

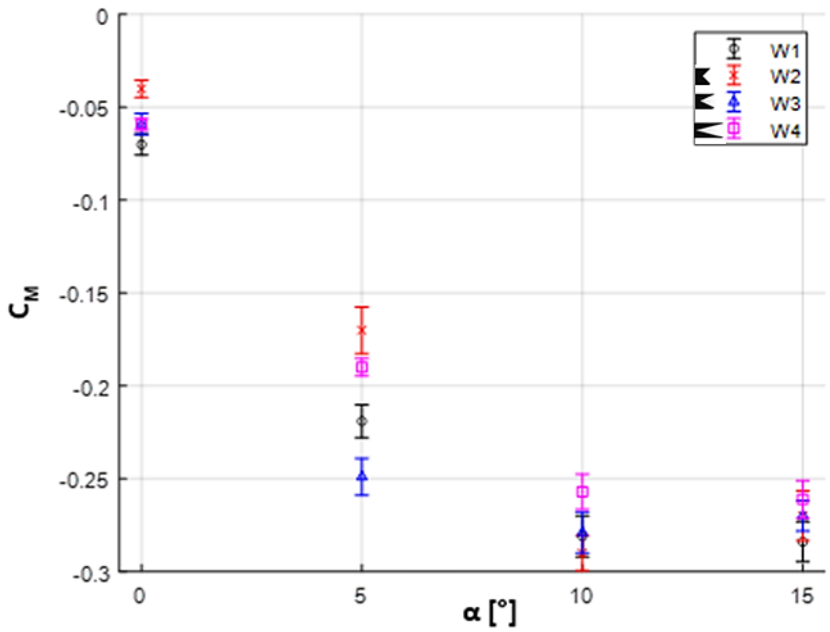

Figure 4.7. C_M based on *d*, *Re* ≈ 30,000

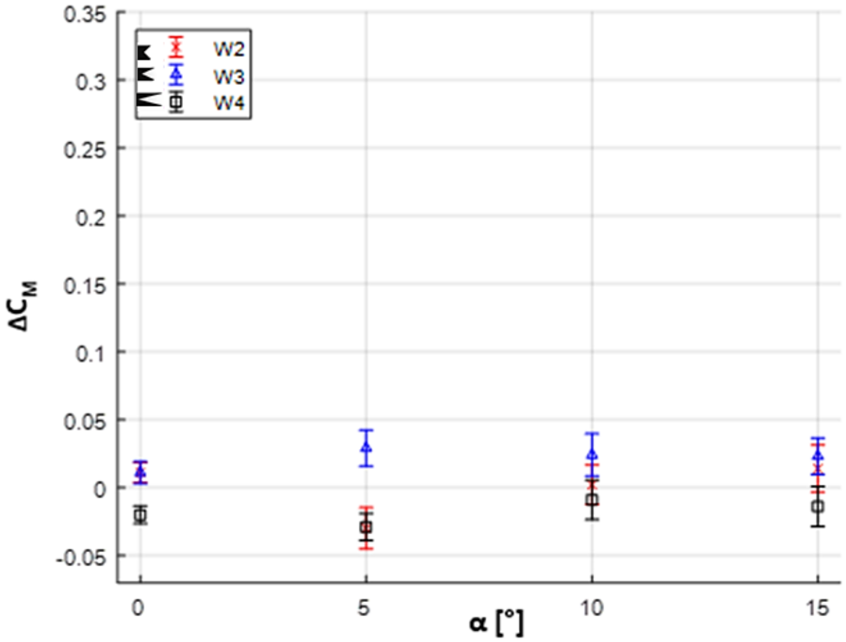

Figure 4.8. ΔC_M based on *d* (serrated samples – W1), *Re* ≈ 30,000

The influence of λ, however, was clearer (see Figures 4.9 and 4.10). W5 with its intermediate *d* had the best results, considering C_L/C_D (improving the performance up to 9%, relative to W1 at α = 5°). This indicated that the distance between each pair of serration-generated streamwise vortices had a direct effect on decreasing the vortex shedding's energy formed at the wing section's TE. Narrow serrations (W3) seemed to lead to an excessive proximity between each pair of streamwise vortices through the sample's span, inducing an increase in C_D. This was believed to be due to a high interaction between each pair of streamwise vortices which reduced their vortex shedding energy attenuation capacity. Similarly, wide serrations (W6) also yielded an increase in C_D, a result of the lack enough streamwise vortices to attenuate the vortex shedding energy. W5, therefore, demonstrated an optimal configuration at this criterion. This was due to two phenomena: a general increase in C_L and reduction of C_D in comparison to W3 and W6 (see Appendices E, F and G). C_M showed similar characteristics to what was observed with C_L/C_D, with W5 improving stability compared to the other wings in this segment (see Figure 4.11 and 4.12).

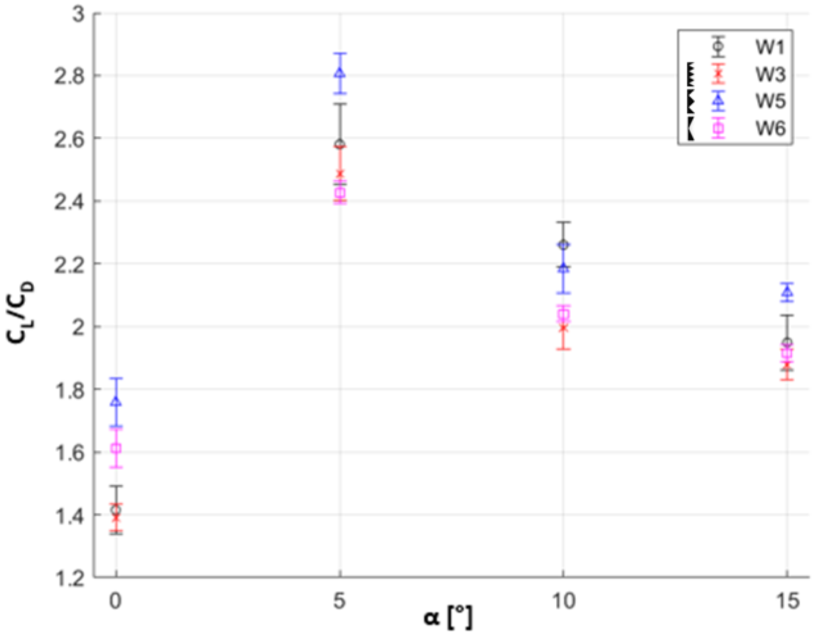

Figure 4.9. C_L/C_D based on λ, *Re* ≈ 30,000

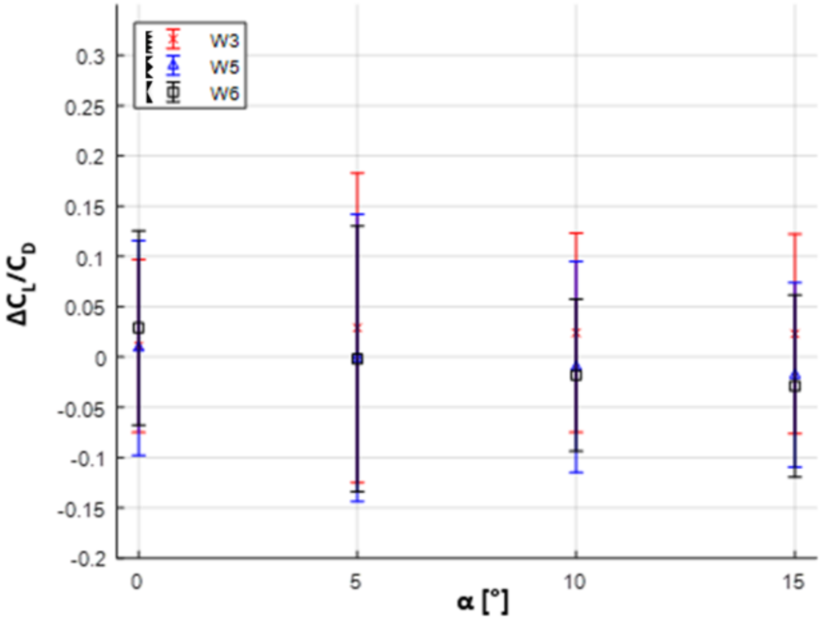

Figure 4.10. $\Delta C_L/C_D$ based on λ (serrated samples – W1), *Re* ≈ 30,000

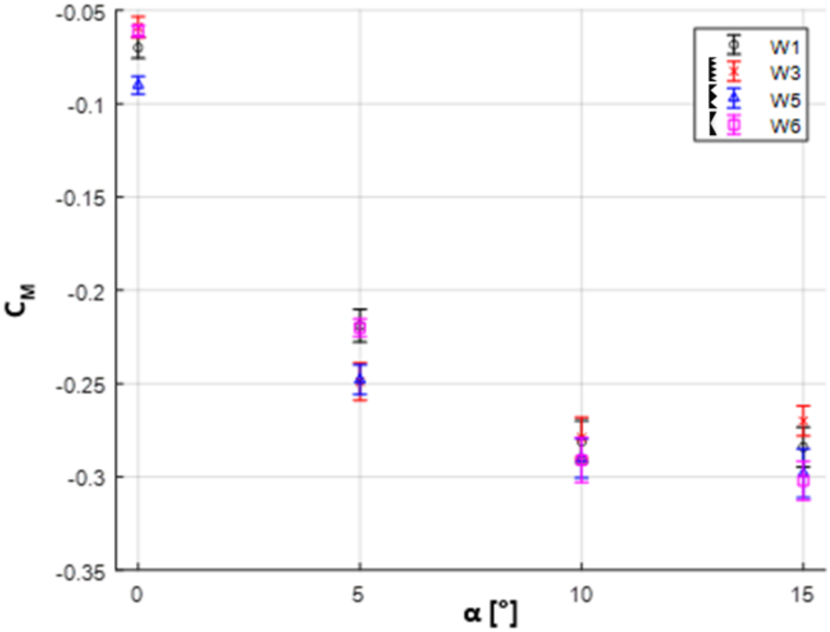

Figure 4.11. C_M based on λ, *Re* ≈ 30,000

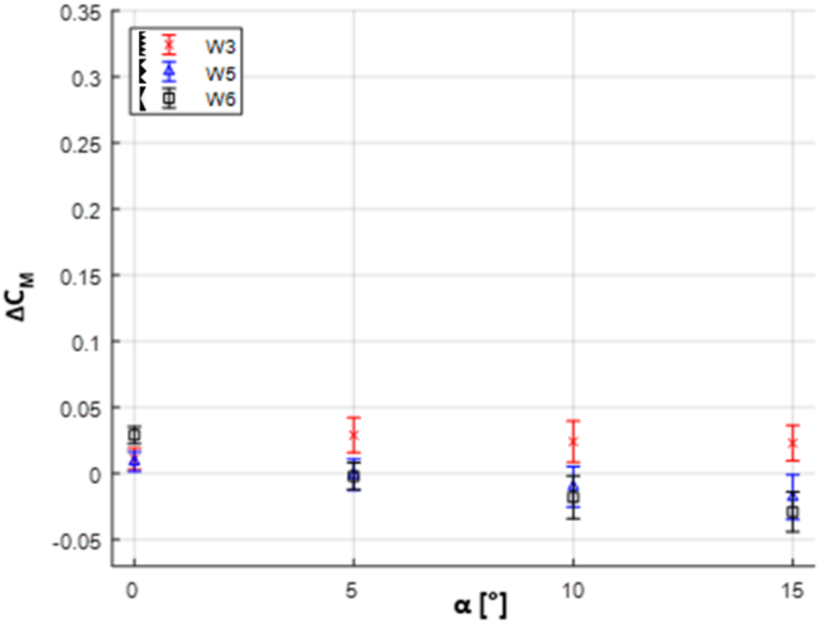

Figure 4.12. ΔC_M based on λ (serrated samples – W1), *Re* ≈ 30,000

Considering the effects of shape, W7 and W8 were built based on the *d* and λ present in W5. At first, it was possible to notice that the improved performance of W5 remained for W7 and W8, showing that their common *d* and λ configuration was the best considered in this thesis (see Figures 4.13 and 4.14). Among these three wing sections, however, W8 and W5 displayed very similar C_L/C_D curves, while W7 showed slightly worse results. Under a more detailed analysis, W7 and W8 matched or outperformed W1 proving capable of reducing C_D of the wing sections while minimizing their impact on C_L (see Appendices E, F and G). No clear trend could be observed for C_M and stability considerations (see Figures 4.15 and 4.16).

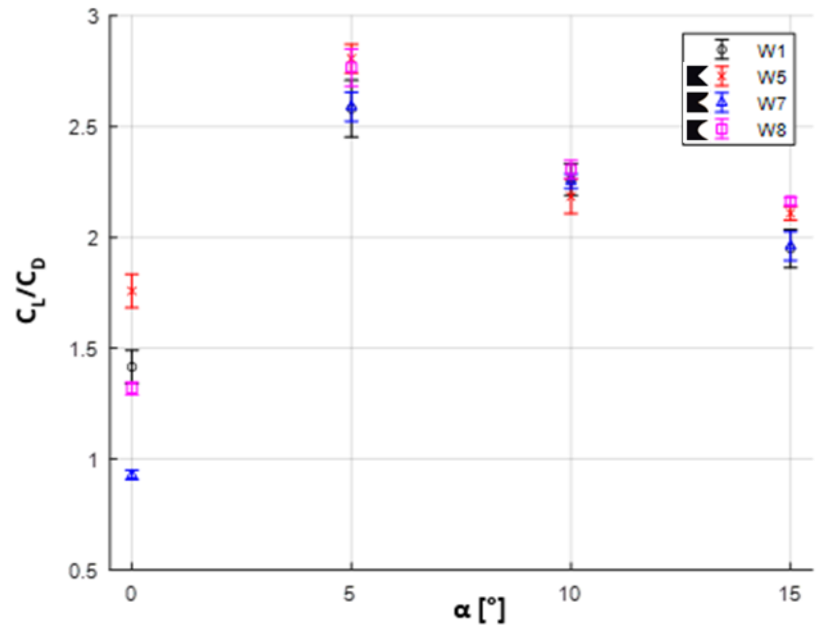

Figure 4.13. C_L/C_D based on serration shape, *Re* ≈ 30,000

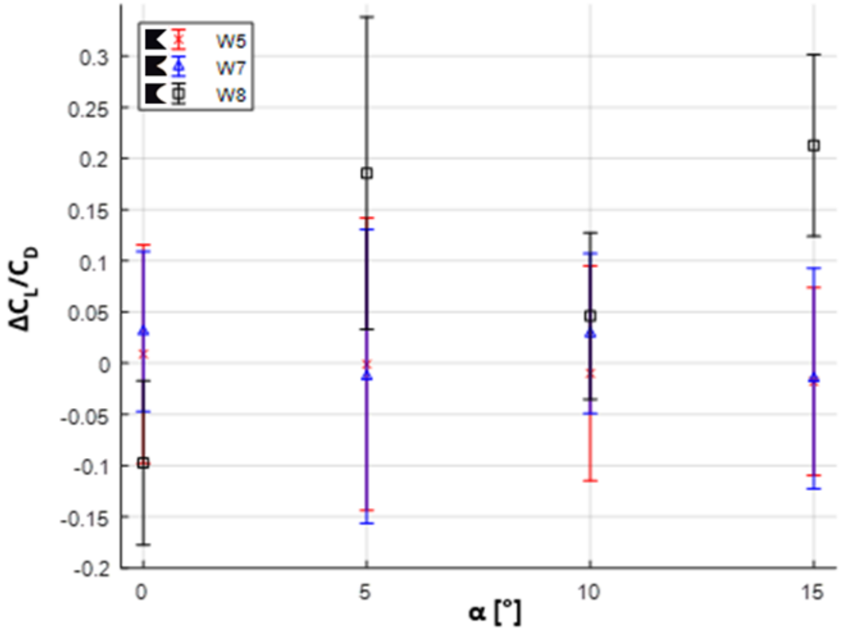

Figure 4.14. $\Delta C_L/C_D$ based on serration shape (serrated samples – W1), *Re* ≈ 30,000

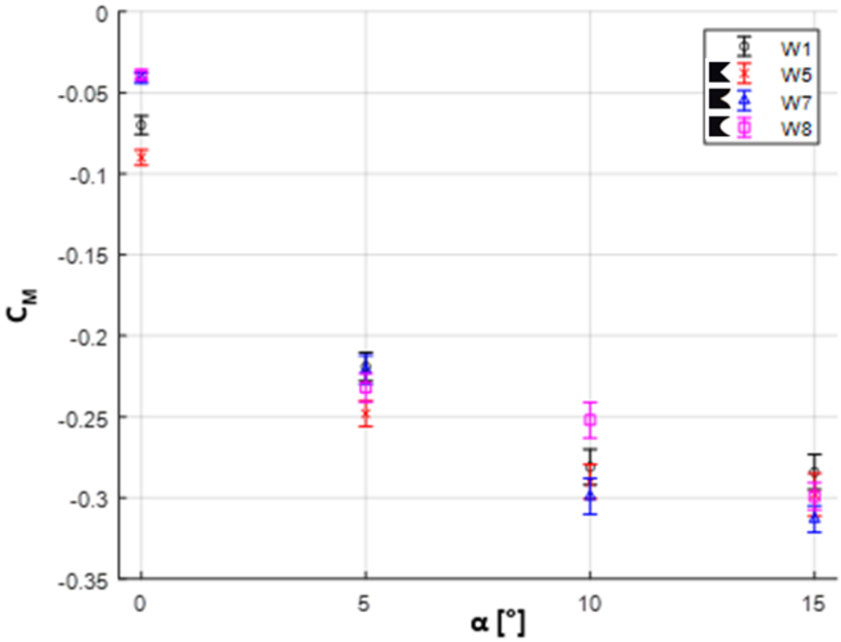

Figure 4.15. C_M based on serration shape, *Re* ≈ 30,000

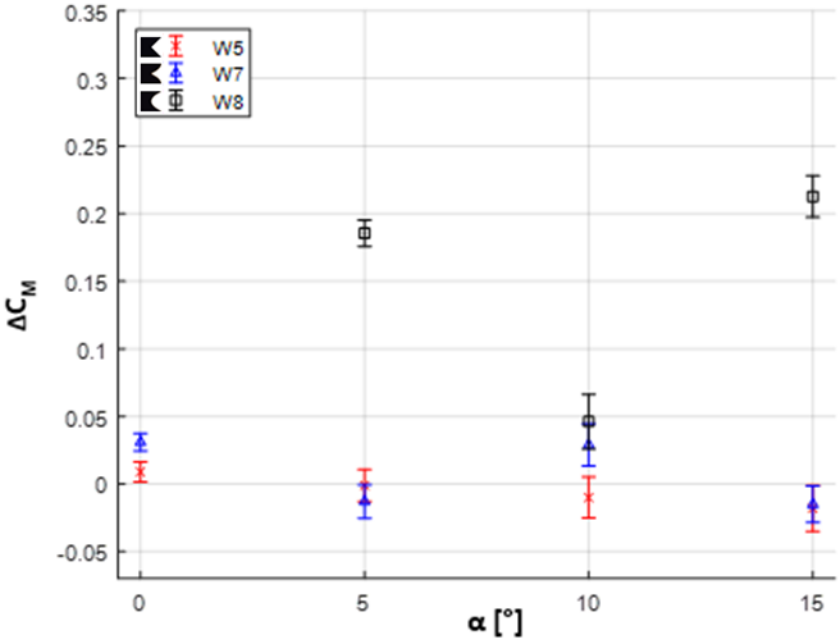

Figure 4.16. ΔC_M based on serration shape (serrated samples – W1), *Re* ≈ 30,000

4.3 PERFORMANCE SUMMARY

Based on the data collected from each of the μWT's tests, some comments could be made. Figure 4.17 shows the performance of each serrated wing at two α: 5˚ and 10˚, representing a pre- and post-flow separation conditions respectively. This is illustrated for every wing sample with TE serrations. The serrated models could provide significant improvements to the C_L/C_D performance of wing sections, depending on λ and d. W5 proved to have the best combination of these two variables. W5, W7 and W8 yielded the best results among serrated samples, and thus were selected for more in-depth, larger scale 3' x 3' WT tests devised to consider higher Re, comprising a greater range of MAVs' flight conditions.

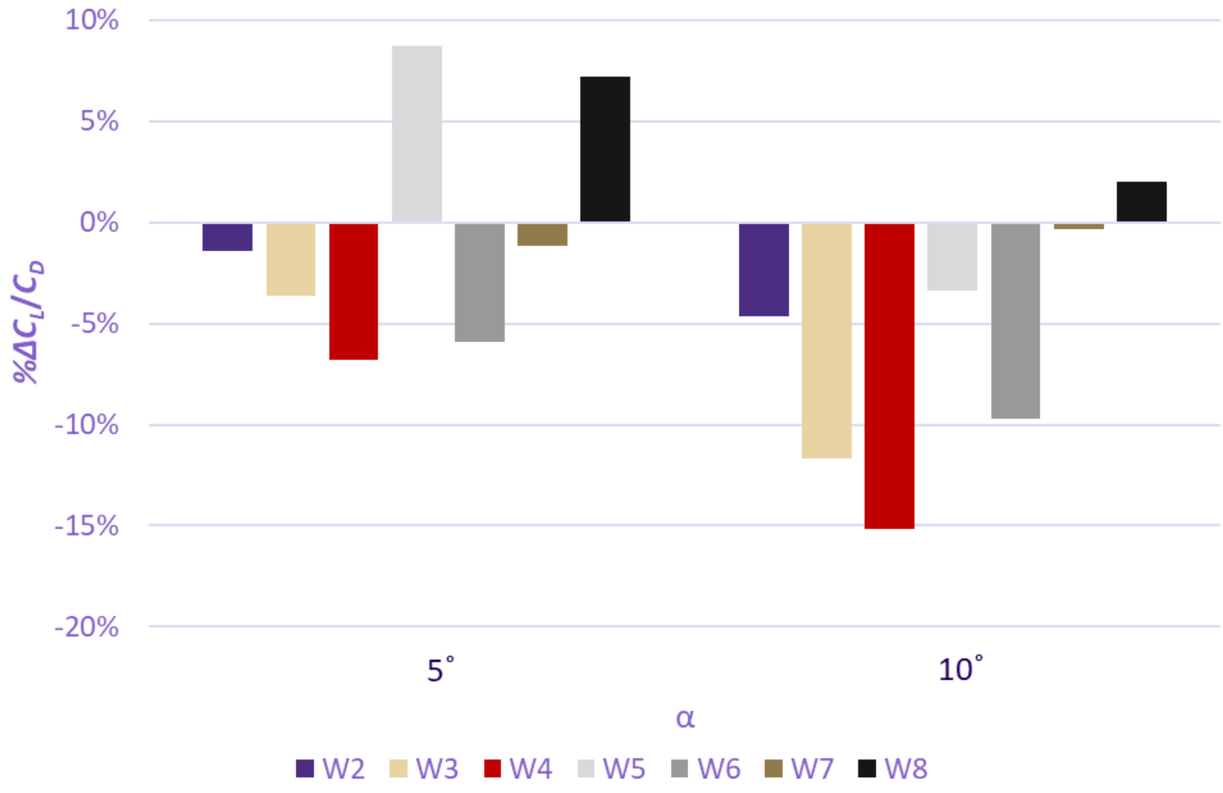

Figure 4.17. $\%\Delta CL/CD$ (serrated TE samples – W1), $Re \approx 30{,}000$.

Chapter 5. 3’ X 3’ WT RESULTS AND ANALYSIS

Tests performed at the 3’x3’ WT facility at the University of Washington continued this study by reducing the number of variables considered. The λ and d were fixed proportional to the parameters defined by W5. These tests also served to improve the reliability of measurements by using more precise instruments and measuring greater loads with higher levels of confinement. The aerodynamic performance of three different types of serrations (W10, W11 and W12, inspired by the µWT’s W5, W7 and W8) and one model with a tapered TE (W13) was evaluated. These wings were compared with the baseline W9 (see Figure 5.1). The samples’ detailed dimensions are described in Table 5.1. Both qualitative and quantitative analysis were performed using, tufts, smoke visualization and force measurements. The quantitative studies were divided into three main portions: C_L/C_D, $(C_L/C_D)/weight$ and C_M. More information on the data collected is presented in Appendices E and F, and additional plots are provided in Appendix G. Sections 5.1, 5.4, 5.5, 5.6, 5.7 and 5.8 expand upon topics previously explored in the research performed by Bron Simplicio et. al. [2].

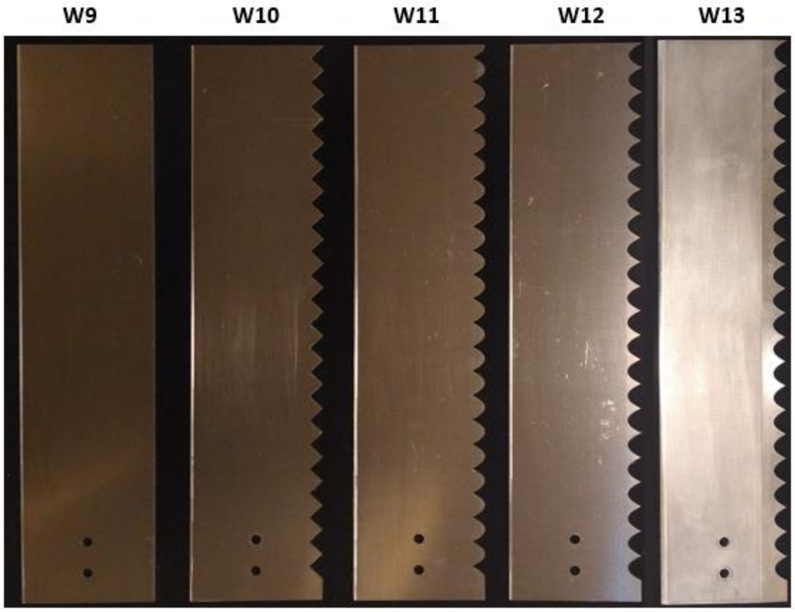

Figure 5.1. Larger wing sections.

Table 5.1. Wing section dimensions for the 3’x3’ WT.

Wing ID	Wind Tunnel	Wing Type	c [m]	s [m]	t [m]	λ [m]	d [m]
W9	3’x3’ WT	Flat Plate	0.10	0.45	0.0030	—	—
W10	3’x3’ WT	Triangular	0.10	0.45	0.0030	0.020	0.0100
W11	3’x3’ WT	Bird Feather	0.10	0.45	0.0030	0.020	0.0100
W12	3’x3’ WT	Membrane	0.10	0.45	0.0030	0.020	0.0100
W13	3’x3’ WT	Membrane with Tapering	0.10	0.45	0.0030	0.020	0.0100

5.1 VALIDATION

Figures 5.2-4 present a validation of the experimental data collected at the 3’x3’ WT. This validation was performed considering the data collected for W9, the baseline flat plate, at a *Re* ≈ 100,000. The results were compared to literature values from Traub et. al. and Selig et. al., which had close *Re* conditions ranging from 80,000 to 120,000 [52, 53]. Starting with C_L, it was clear that this thesis’ data correlated well with the two literature sources [52, 53]. It was understood, therefore, that this study’s C_L data was coherent with what was expected from it (See Figure 5.2).

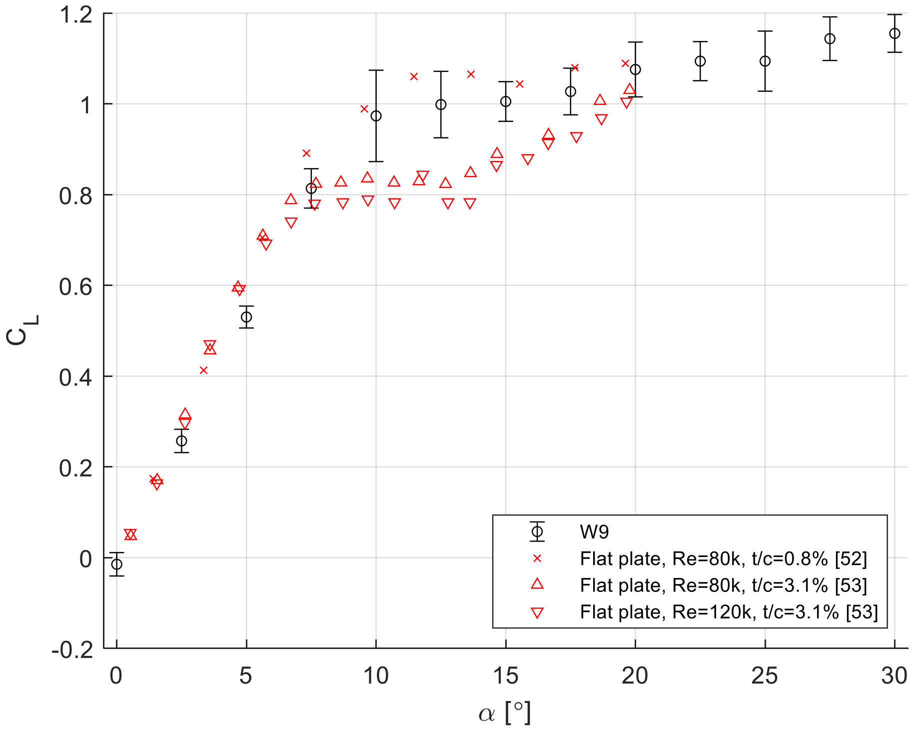

Figure 5.2.Validation plots for C_L vs *α*, *Re* ≈ 100,000 [2].

The C_D validation was done considering the measurements from Traub et. al. at *Re* = 80,000 [52]. Upon further comparison, an offset between W9's and Traub's C_D was observed (see Figure 5.3). W9's C_D was consistently higher than the reference one. This seemed to be attributed to a 3D aerodynamic effect caused by the interaction between the base mount and wing sample as can be seen in Figure 3.12. The presence of the support base interfered with the flow in the region near itself inducing an increase in C_D. The trend of C_D vs α was, however, very similar between them, indicating the validity of using C_D data for relative comparison between the wing specimens and baseline W9.

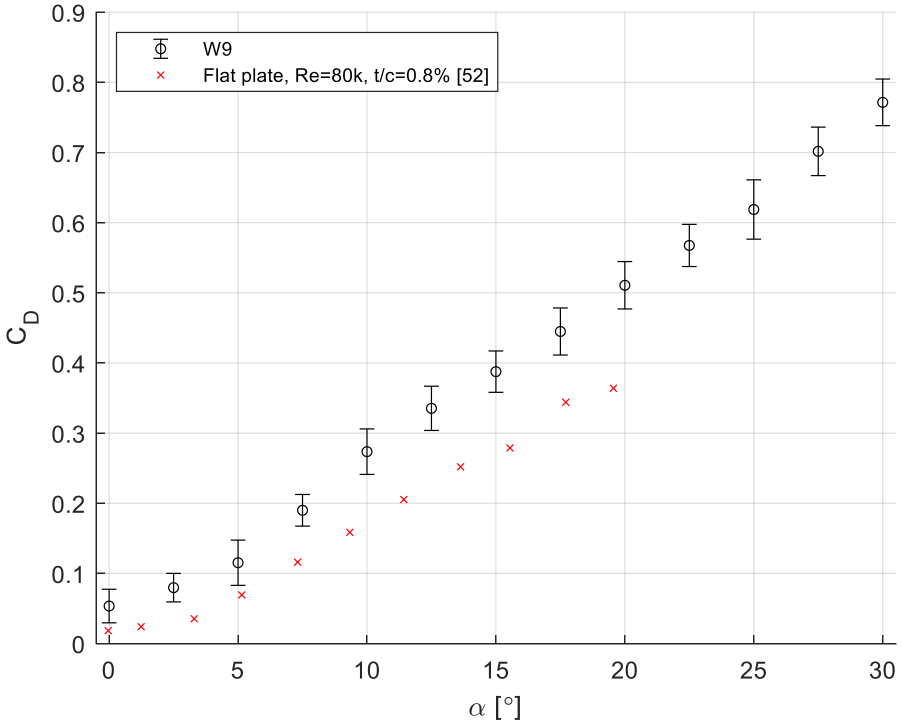

Figure 5.3.Validation plots for C_D vs α, *Re* ≈ 100,000 [2].

The C_M validation was performed by comparing W9's data with measurements from Selig et. al. at *Re* = 80,000 and 120,000 [53]. Similar trends were observed for this case. Therefore, analogous to C_L, it was understood that this study's C_M data was coherent with what was expected from it (See Figure 5.4).

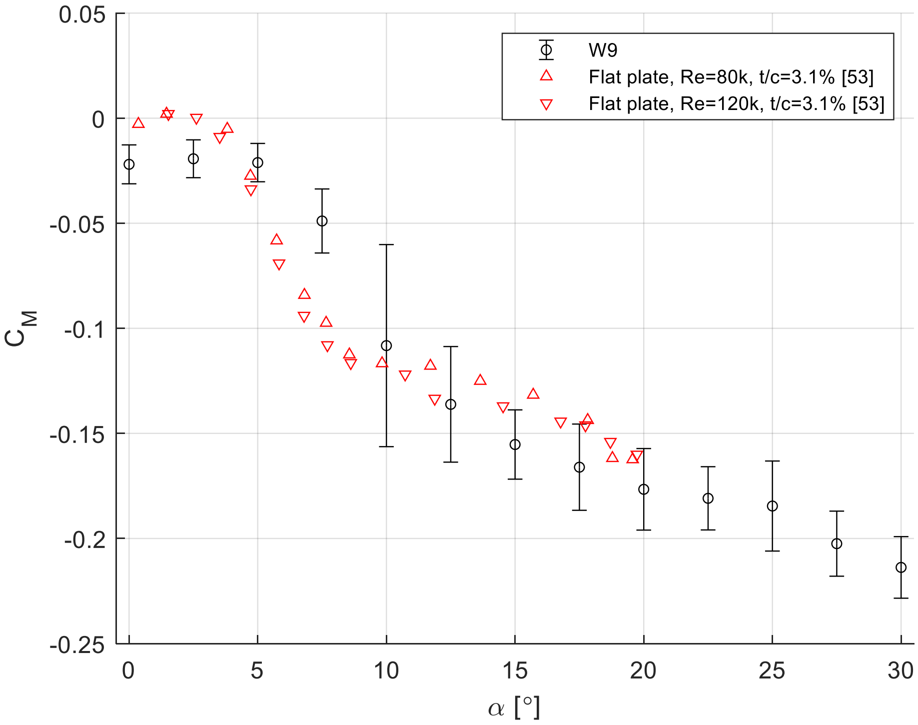

Figure 5.4.Validation plots for C_M vs α, *Re* ≈ 100,000 [2].

5.2 COEFFICIENT OF LIFT

Figures 5.5-7 show ΔC_L measured by subtracting W9's C_L from each individual serrated TE sample. These plots allowed for evaluations of how each serration impacted the wing's C_L performance. They were divided into the three different *Re*: 100,000, 150,000 and 200,000. The plots' vertical bars represented the standard deviation of the averaged data points' time-dependent fluctuations. The data is also presented in Table 5.2, summarizing the mean ΔC_L values of each wing sample for a given *Re* and α.

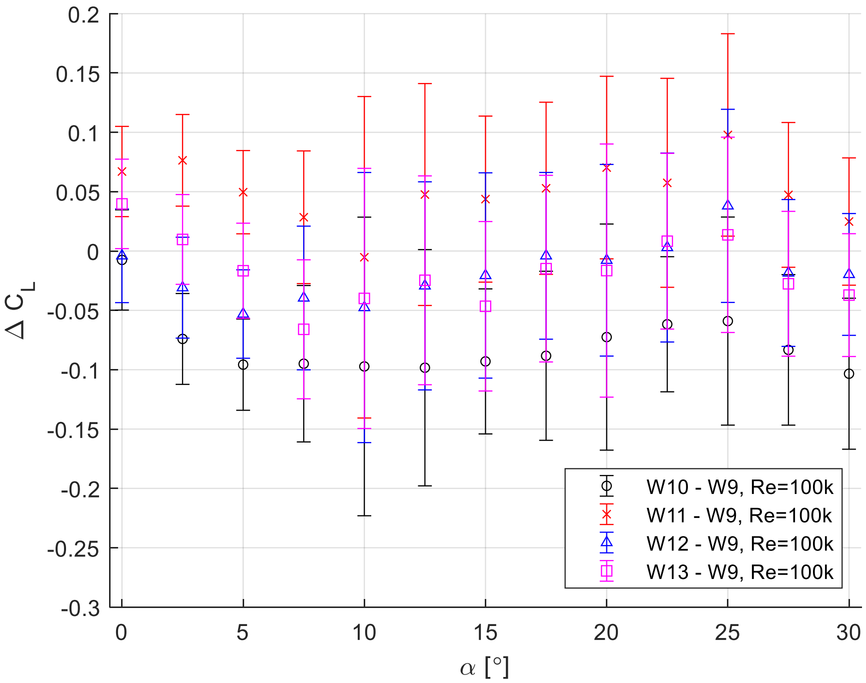

Figure 5.5. ΔC_L of serrated TE samples – W9, *Re* ≈ 100,000.

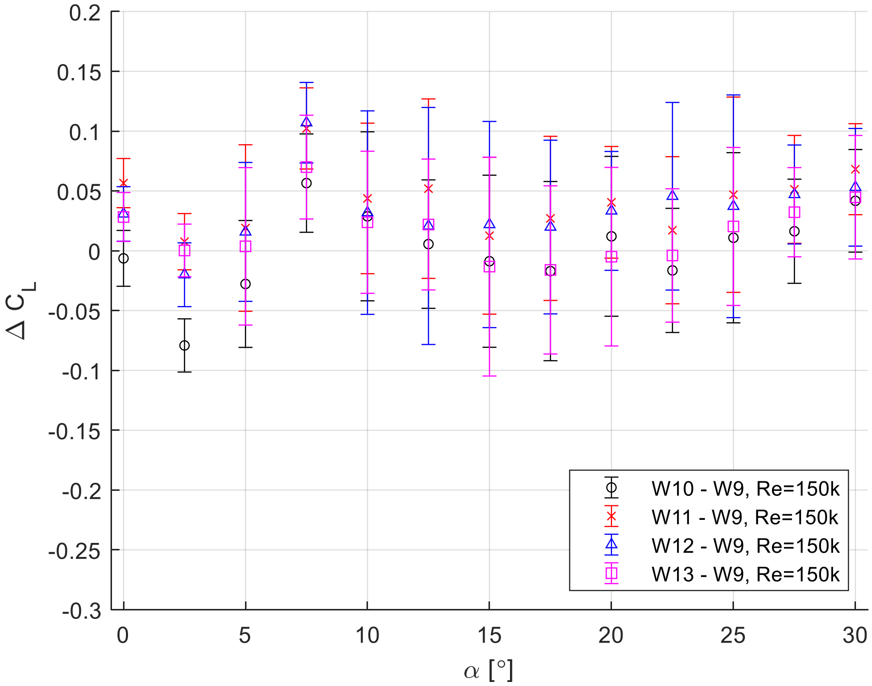

Figure 5.6. ΔC_L of serrated TE samples – W9, *Re* ≈ 150,000.

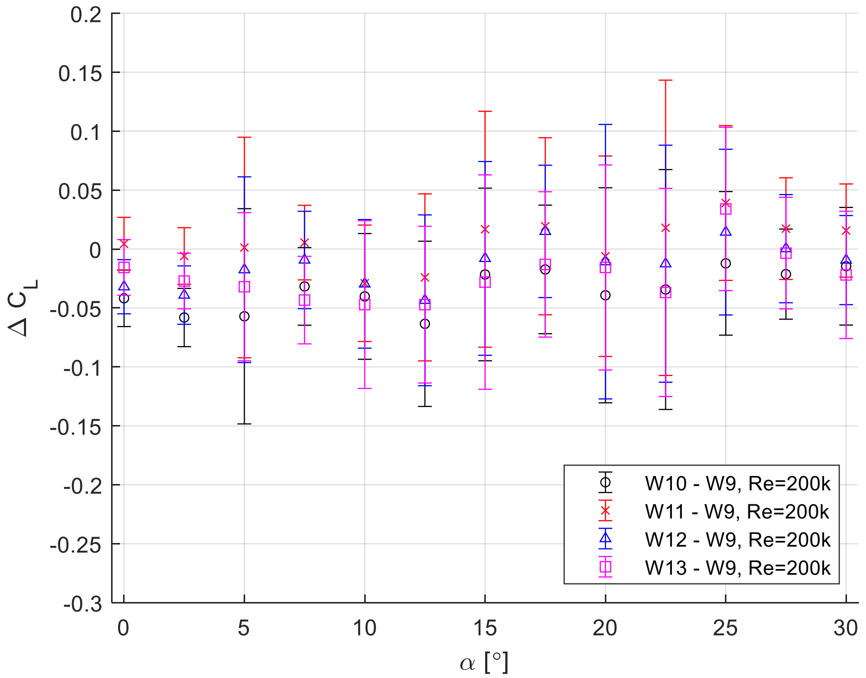

Figure 5.7. ΔC_L of serrated TE samples – W9, *Re* ≈ 200,000.

In analyzing C_L, one factor became of high relevance: the level of bluntness at the TE. Studies comparing blunt and conventional wings showed that the presence of bluntness at the TE increased a wing's C_L [22]. All samples in this project had a level of bluntness, with W9-W12 having a uniform bluntness across their span. W13, in turn had a lower average bluntness thickness, which pointed to a lower C_L performance (see Table 5.2). This was in accordance with most of the samples outperforming W13's C_L. Additionally, W11 was considered the best serrated wing section design, outperforming W9 at *Re* ≈ 100,000. This reached a 30% increase when compared to W9 at *Re* ≈ 100,000 and α = 2.5˚ (see Figure 5.5). W10 and W12 did not have a positive impact relative to baseline W9.

Table 5.2. ΔC_L of wing specimens (serrated TE sample -W9).

Wing ID	**W10**			**W11**			**W12**			**W13**		
Re	1 x 10^5	1.5 x 10^5	2 x 10^5	1 x 10^5	1.5 x 10^5	2 x 10^5	1 x 10^5	1.5 x 10^5	2 x 10^5	1 x 10^5	1.5 x 10^5	2 x 10^5
α	-----	-----	-----	-----	-----	-----	-----	-----	-----	-----	-----	-----
0°	-0.007	-0.050	-0.042	0.067	0.0133	0.004	-0.004	-0.012	-0.032	0.040	-0.015	-0.016
2.5°	-0.074	-0.070	-0.058	0.076	0.017	-0.006	-0.031	-0.011	-0.039	0.010	0.010	-0.027
5°	-0.096	-0.055	-0.057	0.050	-0.008	0.001	-0.053	-0.012	-0.018	-0.017	-0.024	-0.032
7.5°	-0.095	-0.058	-0.032	0.028	-0.013	0.005	-0.039	-0.008	-0.009	-0.066	-0.045	-0.043
10°	-0.097	-0.046	-0.040	-0.005	-0.031	-0.029	-0.048	-0.043	-0.030	-0.040	-0.051	-0.047
12.5°	-0.098	-0.046	-0.063	0.048	0.000	-0.024	-0.029	-0.031	-0.043	-0.025	-0.030	-0.047
15°	-0.093	-0.047	-0.022	0.044	-0.026	0.017	-0.021	-0.016	-0.008	-0.047	-0.052	-0.028
17.5°	-0.088	-0.034	-0.017	0.053	0.010	0.019	-0.004	0.002	0.015	-0.015	-0.033	-0.013
20°	-0.073	-0.008	-0.039	0.070	0.021	-0.006	-0.008	0.014	-0.011	-0.016	-0.025	-0.016
22.5°	-0.062	-0.026	-0.034	0.057	0.008	0.018	0.003	0.036	-0.012	0.008	-0.013	-0.037
25°	-0.059	-0.011	-0.012	0.098	0.025	0.039	0.038	0.015	0.014	0.014	-0.001	0.034
27.5°	-0.083	-0.019	-0.021	0.047	0.016	0.017	-0.018	0.011	0.000	-0.028	-0.003	-0.004
30°	-0.103	-0.025	-0.015	0.025	0.002	0.016	-0.020	-0.013	-0.009	-0.037	-0.022	-0.022

5.3 COEFFICIENT OF DRAG

The results collected for C_D represented a key element in evaluating serrated wing samples. This was due to the understanding that one of the main beneficial effects of TE serrations was the reduction of base *D* when compared to blunt TE wings such as W9 [20, 21, 22, 54, 55]. Figures 5.8-10 show ΔC_D measured at the three *Re* considered in this project. The data is also presented in Table 5.3, summarizing the mean ΔC_D values of each wing sample for a given *Re* and *α*.

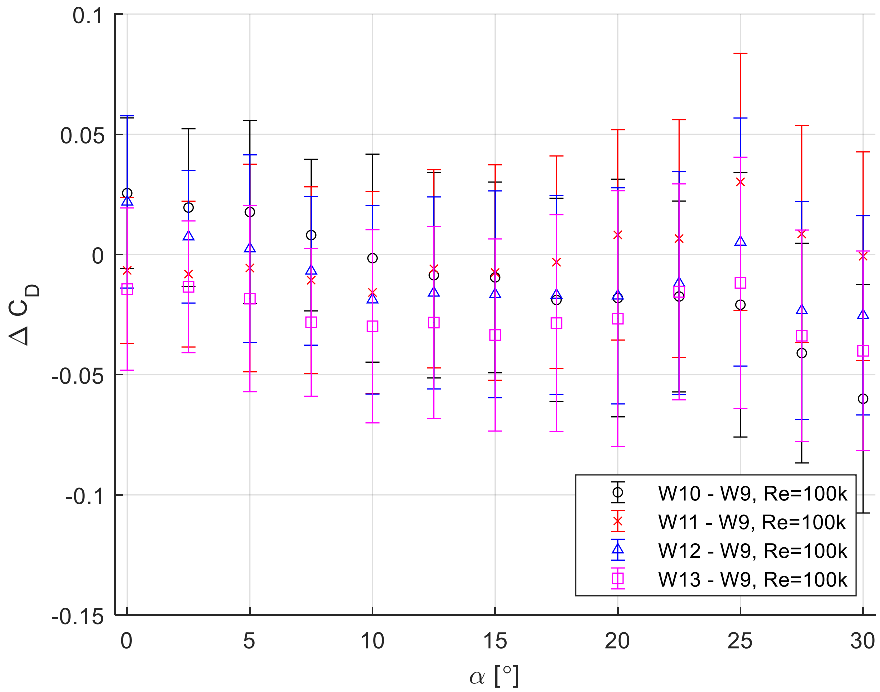

Figure 5.8. ΔC_D of serrated TE samples – W9, *Re* ≈ 100,000.

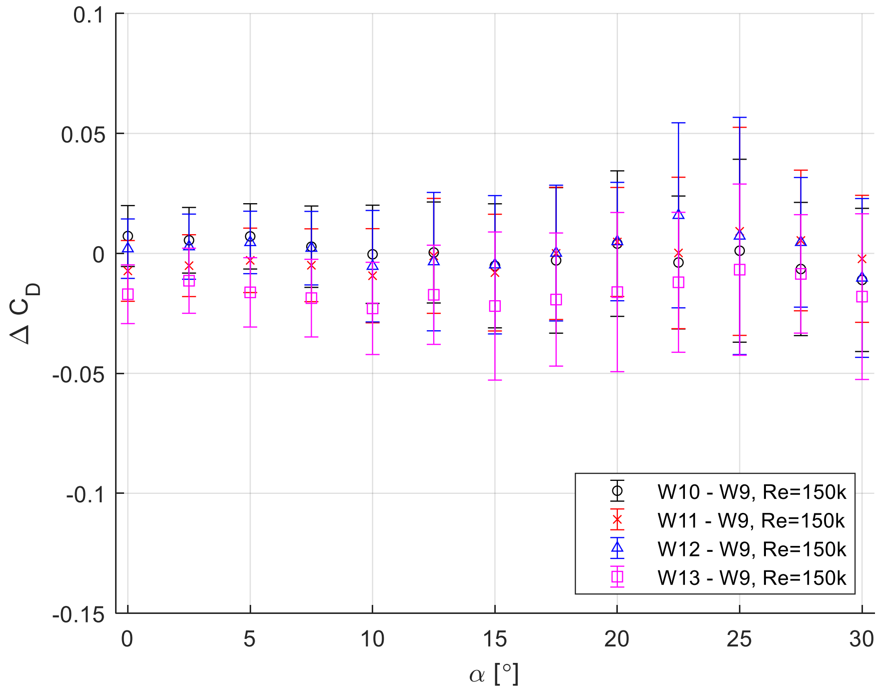

Figure 5.9. ΔC_D of serrated TE samples – W9, *Re* ≈ 150,000.

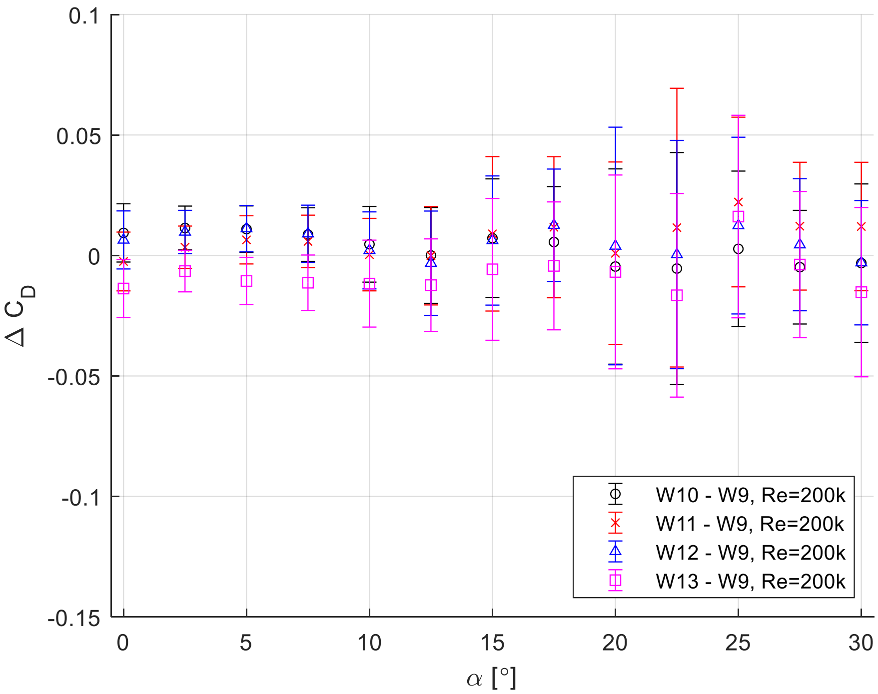

Figure 5.10. ΔC_D of serrated TE samples – W9, Re ≈ 200,000.

Analyzing these results, it was expected that W10, W11, W12, and W13 would have lower C_D than baseline W9. W11 and W13 sustained this assumption at both *Re* ≈ 100,000 and 150,000, while W10 and W12 did not achieve consistently similar beneficial results (see Figure 5.8-9 and Table 5.3). This translated to a 10% reduction in C_D for W11 and 17% for W13, both at *Re* ≈ 100,000 and α = 2.5˚. The difference in performance of each sample was attributed to the shape of serrations, which would affect the serration-generated vortices' intensity and consequently their ability to attenuate the vortex shedding energy. Under this consideration, the bird feather-like serration was the best shape tested. In turn, W13's drag reduction was attributed to the TE's tapering, which alleviated the energy of the TE's periodic vortex shedding. Results at *Re* ≈ 200,000, displayed a decrease in the positive impact noticed at the lower *Re* (see Figure 5.10 and Table 5.3). This, therefore, indicated that the desired improvements in aerodynamic performance associated with employing serrated TEs was dependent on low *Re*, given the specifications of this study.

Table 5.3. ΔC_D of wing specimens (serrated TE sample -W9).

Wing ID	**W10**			**W11**			**W12**			**W13**		
Re	1 x 10^5	1.5 x 10^5	2 x 10^5	1 x 10^5	1.5 x 10^5	2 x 10^5	1 x 10^5	1.5 x 10^5	2 x 10^5	1 x 10^5	1.5 x 10^5	2 x 10^5
α	-----	-----	-----	-----	-----	-----	-----	-----	-----	-----	-----	-----
0˚	0.026	0.007	0.009	-0.007	-0.007	-0.002	0.022	0.002	0.006	-0.014	-0.017	-0.014
2.5˚	0.020	0.005	0.011	-0.008	-0.005	0.003	0.007	0.002	0.010	-0.013	-0.011	-0.006
5˚	0.018	0.007	0.011	-0.006	-0.003	0.006	0.002	0.005	0.011	-0.018	-0.016	-0.011
7.5˚	0.008	0.003	0.009	-0.011	-0.005	0.006	-0.007	0.002	0.009	-0.028	-0.019	-0.011
10˚	-0.002	-0.000	0.005	-0.016	-0.009	0.000	-0.019	-0.005	0.002	-0.030	-0.023	-0.012
12.5˚	-0.009	0.000	0.000	-0.006	-0.001	-0.000	-0.016	-0.003	-0.003	-0.028	-0.017	-0.012
15˚	-0.010	-0.005	0.007	-0.008	-0.008	0.009	-0.017	-0.005	0.006	-0.033	-0.022	-0.006
17.5˚	-0.019	-0.003	0.006	-0.003	-0.000	0.012	-0.017	0.000	0.013	-0.029	-0.019	-0.004
20˚	-0.018	0.004	-0.005	0.008	0.005	0.001	-0.017	0.005	0.004	-0.027	-0.016	-0.007
22.5˚	-0.017	-0.004	-0.005	0.007	0.000	0.012	-0.012	0.016	0.000	-0.016	-0.012	-0.017
25˚	-0.021	0.001	0.003	0.030	0.009	0.022	0.005	0.007	0.012	-0.012	-0.007	0.016
27.5˚	-0.041	-0.007	-0.005	0.009	0.005	0.012	-0.023	0.005	0.004	-0.034	-0.009	-0.004
30˚	-0.060	-0.011	-0.003	-0.001	-0.002	0.012	-0.025	-0.010	-0.003	-0.040	-0.018	-0.015

5.4 LIFT-TO-DRAG RATIO

The following plots show $\Delta C_L/C_D$ measured by subtracting W9's C_L/C_D from each individual serrated TE sample (see Figures 5.11-13). The data is also presented in Table 5.4, summarizing the mean $\Delta C_L/C_D$ values of each wing sample for a given *Re* and *α*. Considering Figure 5.11 (*Re* ≈ 100,000), there was a higher distinction between each sample's average measurements at $\alpha <$ 10˚. In this range of *α*, W11 and W13 presented an improvement in C_L/C_D compared to W9. Meanwhile, W10 and W12 performed worse than W9. Past 10˚, there was a convergency in the results across all samples considered, with negligible differences among them. A similar trend was also seen in the *L/D* data provided by other experiments on modified TE, such as in Nedić & Vassilicos' data [22].

Figure 5.12 shows the C_L/C_D performance of every sample at $Re \approx 150{,}000$. At this flow condition, the C_L/C_D curve represented a general increase in performance compared to the one presented for $Re \approx 100{,}000$. A similar aerodynamic behavior was also noticed where most of the data points' differences were present at $\alpha < 10^\circ$, with W11 and W13 being the ones capable of improvements. Nonetheless, this difference between samples' results substantially decreased.

At $Re \approx 200{,}000$, a change was observed with a significant worsening in aerodynamic performance across the serrated TE wing sections (see Figure 5.13). In this case, only W13 appeared to marginally outperform W9. This pointed to a decrease in aerodynamic effectivity of serrated TEs, suggesting that serrations were especially beneficial at lower *Re*, those analogous to the flight conditions of most small sized MAVs.

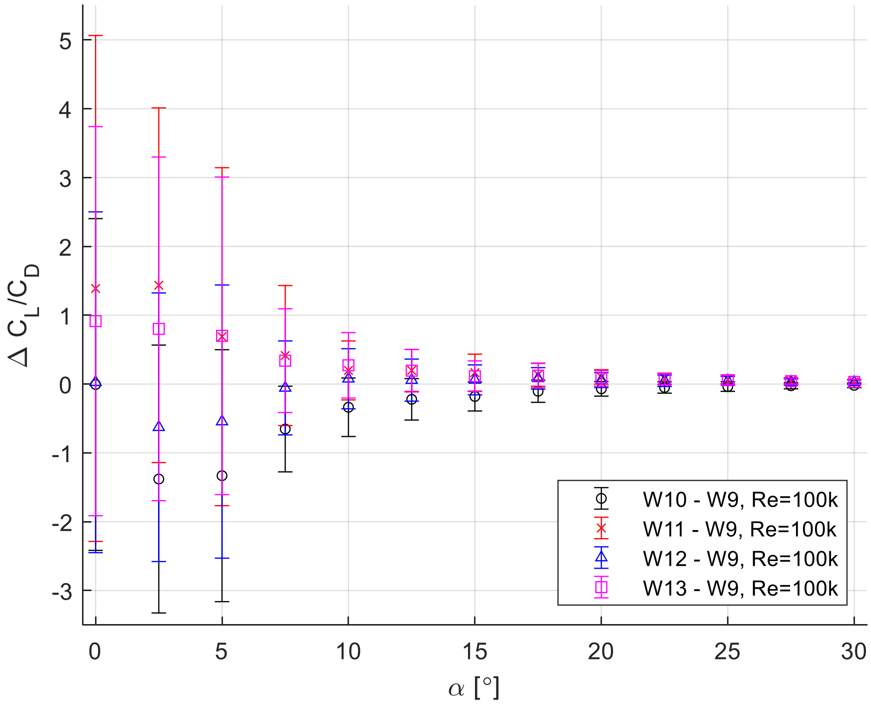

Figure 5.11. $\Delta C_L/C_D$ of serrated TE samples – W9, $Re \approx 100{,}000$ [2]

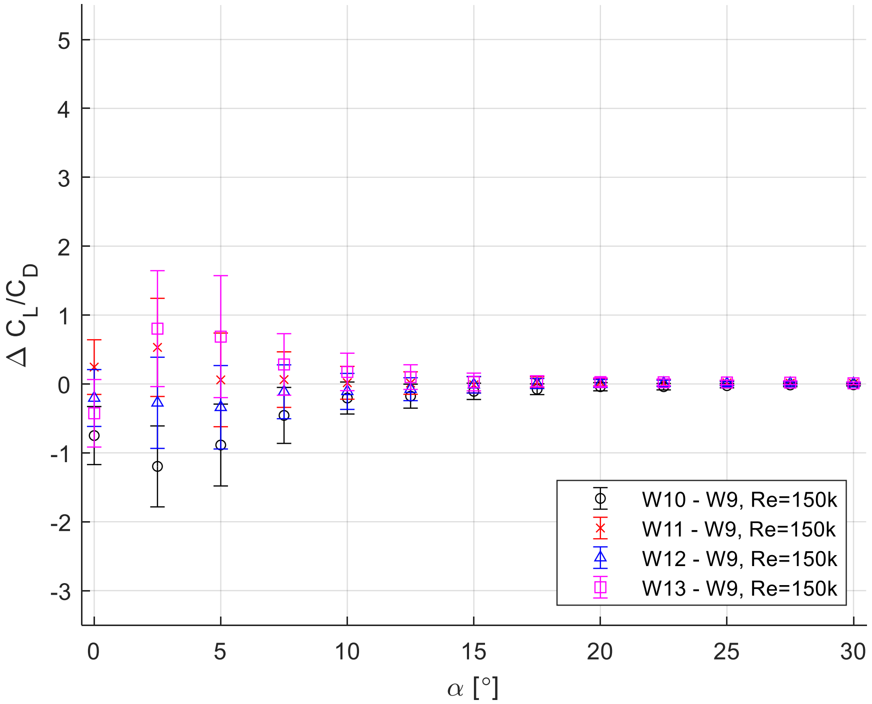

Figure 5.12. $\Delta C_L/C_D$ of serrated TE samples – W9, *Re* ≈ 150,000 [2]

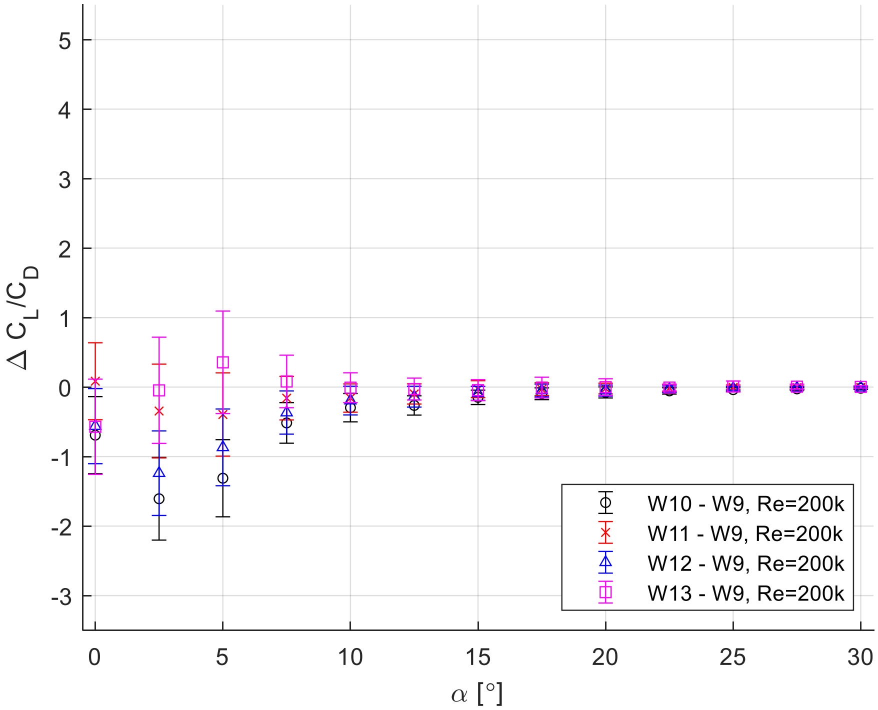

Figure 5.13. $\Delta C_L/C_D$ of serrated TE samples – W9, *Re* ≈ 200,000 [2]

The C_L/C_D results, as influenced by each individual parameter's results, continued to reflect W11's and W13's dominating performance (see Table 5.4 and Figure 5.11-13). This was mostly noticed at $\alpha < 10^\circ$. For example, a 44% C_L/C_D improvement for W11 and a 25% for W13 was observed when compared to W9 at $\alpha = 2.5^\circ$ and $Re \approx 100{,}000$. At $\alpha \geq 10^\circ$, all wing samples behaved similarly, indicating the prevalence of flow separation effects on the wing section's aerodynamic performance over the serrations' effects of *D* reduction.

Table 5.4. $\Delta C_L/C_D$ of wing specimens (serrated TE sample -W9).

Wing ID	**W10**			**W11**			**W12**			**W13**		
Re	1 x 10^5	1.5 x 10^5	2 x 10^5	1 x 10^5	1.5 x 10^5	2 x 10^5	1 x 10^5	1.5 x 10^5	2 x 10^5	1 x 10^5	1.5 x 10^5	2 x 10^5
α	-----	-----	-----	-----	-----	-----	-----	-----	-----	-----	-----	-----
0˚	-0.007	-0.749	-0.692	1.388	0.245	0.085	0.026	-0.204	-0.562	0.913	-0.426	-0.571
2.5˚	-1.380	-1.197	-1.607	1.435	0.530	-0.345	-0.628	-0.274	-1.239	0.801	0.802	-0.046
5˚	-1.332	-0.887	-1.311	0.688	0.059	-0.394	-0.545	-0.339	-0.867	0.700	0.686	0.356
7.5˚	-0.654	-0.456	-0.515	0.414	0.063	-0.159	-0.056	-0.114	-0.366	0.339	0.283	0.081
10˚	-0.337	-0.204	-0.296	0.198	0.017	-0.158	0.076	-0.108	-0.194	0.272	0.174	-0.009
12.5˚	-0.222	-0.177	-0.264	0.198	0.013	-0.099	0.057	-0.076	-0.138	0.194	0.099	-0.028
15˚	-0.181	-0.077	-0.147	0.166	-0.013	-0.030	0.060	-0.011	-0.090	0.114	0.028	-0.044
17.5˚	-0.105	-0.040	-0.096	0.136	0.027	-0.029	0.082	0.006	-0.048	0.123	0.039	-0.007
20˚	-0.070	-0.040	-0.077	0.102	0.025	-0.021	0.058	0.007	-0.051	0.082	0.027	-0.001
22.5˚	-0.051	-0.025	-0.055	0.078	0.016	-0.012	0.047	0.010	-0.031	0.069	0.024	-0.008
25˚	-0.037	-0.014	-0.037	0.068	0.016	-0.004	0.046	0.004	-0.018	0.057	0.021	0.009
27.5˚	-0.025	-0.015	-0.025	0.047	0.012	-0.006	0.029	0.007	-0.014	0.041	0.019	0.006
30˚	-0.019	-0.013	-0.017	0.034	0.008	-0.005	0.024	0.003	-0.008	0.031	0.009	0.003

5.5 LIFT-DRAG/WEIGHT

The *(C_L/C_D)/weight* results were collected to determine the efficiency of each wing sample. They are shown in Figures 5.14-16. The data is also presented in Table 5.5, summarizing the mean *Δ(C_L/C_D)/weight* values of each wing sample for a given *Re* and *α*. Given that small dimensions of MAVs limit efficiency factors such as propulsion capabilities, weight changes became a key factor in determining their payload capacities, flight range or necessary airspeed. In the case of these wing sections, the serrations were created by cutting the TE, a process that reduced the overall weight of each serrated wing section by different amounts depending on their geometry. Tapering the TE further reduced W13's weight.

The results collected, therefore, revealed a positive impact associated with weight reductions related to employing serrations (see Table 5.5). At *Re* ≈ 100,000, W11 and W13 still were the two samples that consistently outperformed W9 (see Figure 5.14). W12 was also competitive, while W10 remained as the worst performing sample. Figure 5.15 shows the performance of the specimens at *Re* ≈ 150,000. Similar to what was described in the case considering a *Re* ≈ 100,000, W11 and W13 presented an advantage over W9. W12 also outperformed W9 at $\alpha \geq 7.5^{\circ}$. Figure 5.16 shows the performance of the specimens at *Re* ≈ 200,000. In these flow conditions, only W13 represented a consistent positive $\Delta(C_L/C_D)/weight$ across all α.

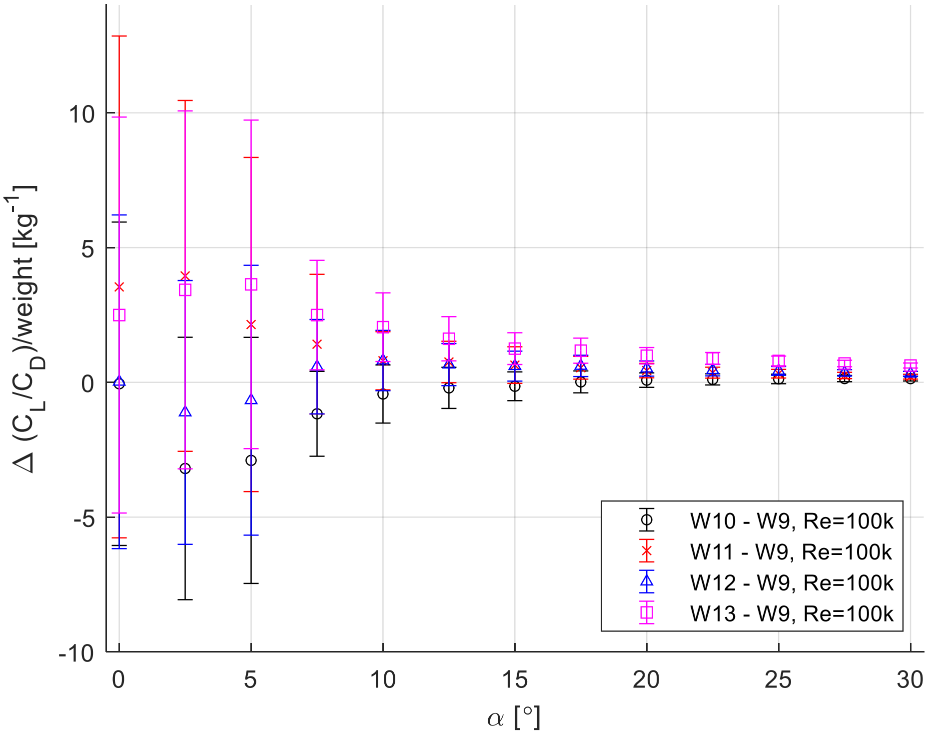

Figure 5.14. $\Delta(C_L/C_D)/weight$ of serrated TE samples – W9, *Re* ≈ 100,000 [2]

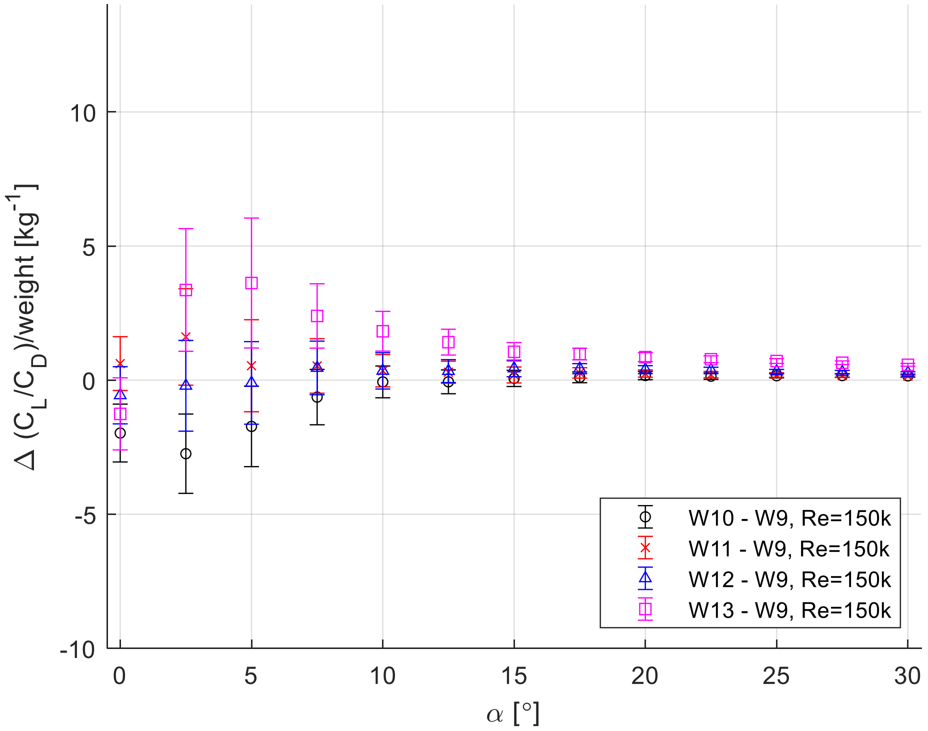

Figure 5.15. $\Delta(C_L/C_D)$*/weight* of serrated TE samples – W9, *Re* ≈ 150,000 [2]

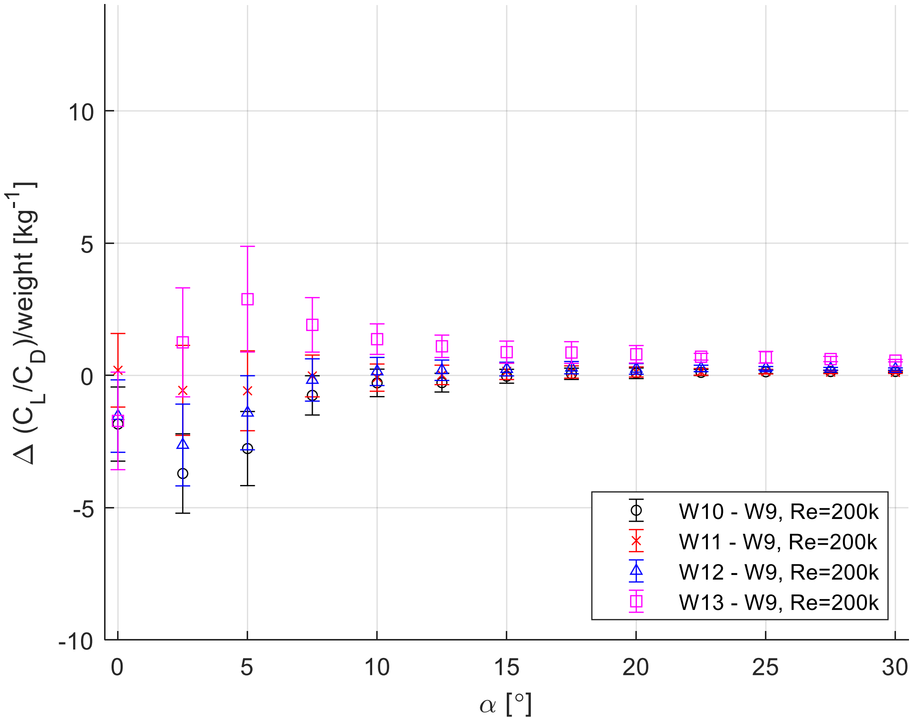

Figure 5.16. $\Delta(C_L/C_D)$*/weight* of serrated TE samples – W9, *Re* ≈ 200,000 [2]

Table 5.5. $\Delta(C_L/C_D)$/*weight* of wing specimens (serrated TE sample -W9) [kg^{-1}].

Wing ID	**W10**			**W11**			**W12**			**W13**		
Re	1 x 10^5	1.5 x 10^5	2 x 10^5	1 x 10^5	1.5 x 10^5	2 x 10^5	1 x 10^5	1.5 x 10^5	2 x 10^5	1 x 10^5	1.5 x 10^5	2 x 10^5
α	-----	-----	-----	-----	-----	-----	-----	-----	-----	-----	-----	-----
0°	-0.052	-1.972	-1.838	3.540	0.617	0.195	0.022	-0.565	-1.537	2.497	-1.259	-1.719
2.5°	-3.195	-2.743	-3.707	3.949	1.611	-0.565	-1.116	-0.212	-2.629	3.431	3.361	1.250
5°	-2.896	-1.726	-2.764	2.146	0.537	-0.580	-0.663	-0.103	-1.411	3.635	3.620	2.882
7.5°	-1.167	-0.632	-0.754	1.416	0.529	-0.020	0.581	0.455	-0.171	2.495	2.392	1.911
10°	-0.433	-0.066	-0.282	0.801	0.350	-0.083	0.809	0.345	0.150	2.046	1.822	1.372
12.5°	-0.205	-0.063	-0.273	0.755	0.295	0.020	0.659	0.337	0.196	1.617	1.415	1.101
15°	-0.145	0.063	-0.031	0.641	0.192	0.156	0.602	0.435	0.240	1.251	1.056	0.881
17.5°	0.017	0.104	0.062	0.541	0.269	0.129	0.610	0.428	0.294	1.175	0.973	0.866
20°	0.083	0.170	0.082	0.437	0.245	0.131	0.512	0.390	0.248	0.987	0.857	0.801
22.5°	0.110	0.146	0.113	0.359	0.206	0.136	0.453	0.365	0.265	0.887	0.779	0.707
25°	0.126	0.164	0.137	0.322	0.191	0.143	0.424	0.321	0.268	0.794	0.712	0.686
27.5°	0.140	0.170	0.146	0.255	0.168	0.124	0.354	0.301	0.251	0.700	0.648	0.619
30°	0.139	0.159	0.150	0.210	0.147	0.115	0.320	0.269	0.241	0.624	0.571	0.559

5.6 STABILITY

Regarding wing section stability, C_M vs α was used as a metric (see Figure 5.17-19). This was done to establish the way by which each sample would respond when their α was changed. A stable specimen would respond to an increase in α with a negative C_M, indicating a tendency to return to a neutral α. C_M was measured relative to the quarter point of each wing's *c*. Table 5.6, summarizes the mean ΔC_M values of each wing sample for a given *Re* and α.

Considering Figure 5.17, all samples demonstrated a stable behavior at $Re \approx 100,000$. The serrated TE wing sections, however, showed a less stable condition where ΔC_M continued to increase as α was raised. The serrated samples' less stable behavior observed at $Re \approx 100,000$, continued to be the case as *Re* was changed to 150,000 (see Figure 5.18). Little change in general was noticed between the data from these two *Re*. Figure 5.19 shows C_M at $Re \approx 200,000$. At this flow condition, the same less stable behavior compared to the baseline W9 was observed for wing sections with a serrated TE. However, the standard deviation of the averaged data points' time-dependent fluctuations presented a drastic increase at $\alpha \geq 15^{\circ}$, indicating an increase in an unstable flow condition.

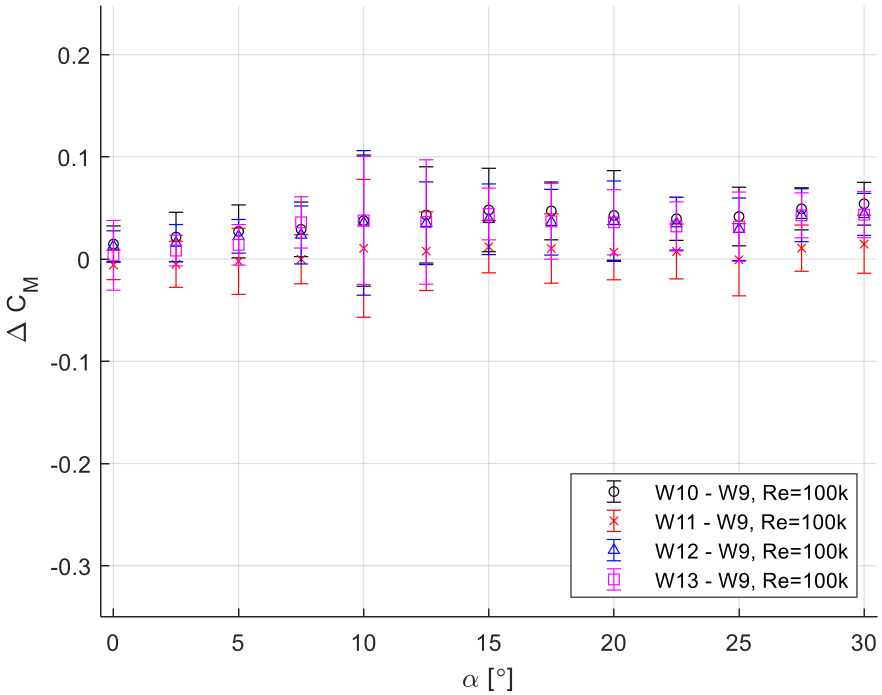

Figure 5.17. ΔC_M of serrated TE samples – W9, *Re* ≈ 100,000 [2]

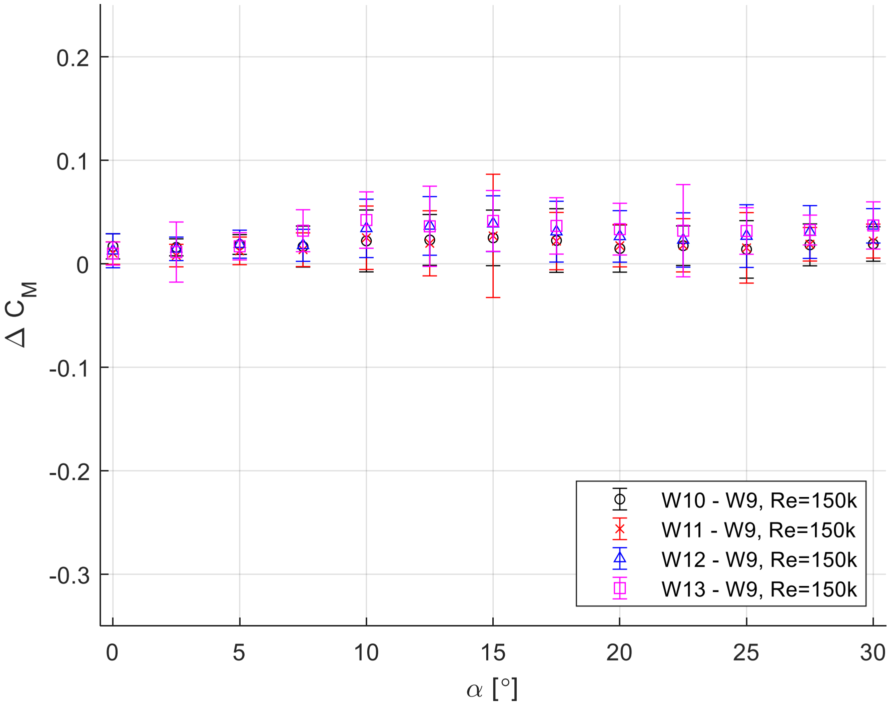

Figure 5.18. ΔC_M of serrated TE samples – W9, *Re* ≈ 150,000 [2]

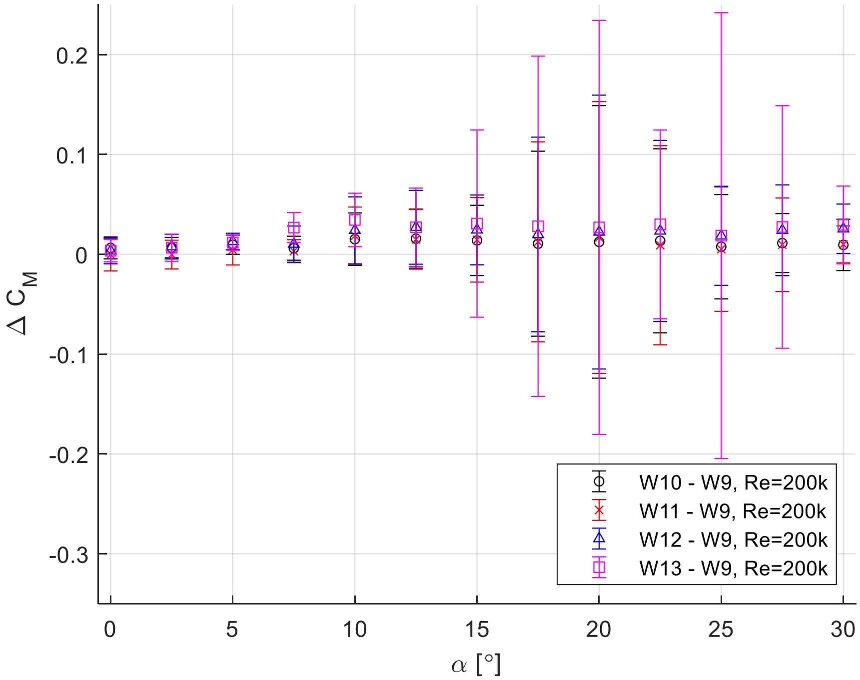

Figure 5.19. ΔC_M of serrated TE samples – W9, *Re* ≈ 200,000 [2]

Overall, W11 had the best results among the serrated samples, rivaling the flat plate at the lowest tested *Re* (see Table 5.6 and Figure 5.17-19). In fact, the stability of serrated specimens seemed to decrease as the mean chord length (c_{mean}) was reduced, indicating a correlation between both parameters. This reduction of the wing's c_{mean} was caused by the implementation of serrations cut into each sample. The difference between c and c_{mean} affected the effective aerodynamic center of pressure, moving it forward. This induced a decrease in intensity of C_M in reference to the c's quarter point.

Table 5.6. ΔC_M of wing specimens (serrated TE sample -W9).

Wing ID	**W10**			**W11**			**W12**			**W13**		
Re	1 x 10^5	1.5 x 10^5	2 x 10^5	1 x 10^5	1.5 x 10^5	2 x 10^5	1 x 10^5	1.5 x 10^5	2 x 10^5	1 x 10^5	1.5 x 10^5	2 x 10^5
α	-----	-----	-----	-----	-----	-----	-----	-----	-----	-----	-----	-----
0°	0.015	0.017	0.006	-0.006	0.010	-0.000	0.013	0.013	0.003	0.004	0.010	0.004
2.5°	0.022	0.016	0.007	-0.005	0.008	-0.000	0.016	0.014	0.008	0.008	0.011	0.007
5°	0.027	0.019	0.010	-0.002	0.012	0.004	0.022	0.019	0.013	0.014	0.017	0.012
7.5°	0.029	0.017	0.006	-0.000	0.014	0.003	0.024	0.018	0.010	0.036	0.032	0.027
10°	0.038	0.022	0.015	0.010	0.025	0.019	0.035	0.034	0.024	0.038	0.042	0.034
12.5°	0.043	0.023	0.016	0.008	0.020	0.015	0.035	0.037	0.027	0.036	0.036	0.027
15°	0.048	0.025	0.014	0.012	0.027	0.014	0.039	0.039	0.024	0.044	0.041	0.031
17.5°	0.047	0.022	0.011	0.010	0.022	0.013	0.036	0.031	0.020	0.037	0.037	0.028
20°	0.043	0.015	0.012	0.007	0.017	0.017	0.037	0.026	0.022	0.036	0.033	0.027
22.5°	0.039	0.017	0.014	0.007	0.018	0.009	0.035	0.023	0.023	0.032	0.032	0.030
25°	0.042	0.014	0.008	-0.001	0.015	0.005	0.029	0.027	0.018	0.032	0.032	0.019
27.5°	0.049	0.018	0.011	0.011	0.019	0.010	0.043	0.031	0.024	0.043	0.033	0.027
30°	0.054	0.019	0.009	0.015	0.022	0.010	0.044	0.037	0.026	0.043	0.037	0.029

5.7 PERFORMANCE SUMMARY

Based on results presented, a multivariable analysis of the wing samples was performed with the use of radar charts to rank them. Five metrics related to the 3’ x 3’ WT data were selected for this analysis according to the ones previously described: stability (related to C_M vs α), C_L, C_D, C_L/C_D, and *(C_L/C_D)/weight* (see Figures 5.20-21). For each parameter, a worse performance was indicated by a sample being closer to the center of a chart. These categories were selected as they represented relevant measurement criteria for low-speed, low thrust vehicles.

A few observations were made that applied to the wing sections in general. One of them was an association between the decrease in *Re* from 200,000 to 100,000 and an increase in aerodynamic benefits from serrated TEs. This was clear in Figure 5.20, with W9’s performance gradually surpassing the serrated samples as *Re* was changed from 100,000 to 150,000 and 200,000. The increase in effectivity of serrated TEs at lower *Re* was attributed to a thicker boundary layer. Such an increase in boundary layer thickness results in an expansion of the region affected by vortex shedding near the blunt TE, amplifying the latter's contribution to the overall *D*. Consequently, the *D* reduction associated with the interaction between serration-generated vortices and blunt TE-induced periodic vortex shedding was magnified [54]. This indicated that employing serrated TEs was especially beneficial at lower *Re*, a range similar to most small sized, fixed-wing MAVs' flight conditions.

Another consideration worth mentioning was the differences observed between Figure 5.20 and Figure 5.21. Instead of the gradual changes that characterized each sample's performance as *Re* increased for $\alpha < 10^\circ$, past 10° these were more abrupt. The unstable aerodynamic behavior of the specimens at $\alpha \geq 10^\circ$ was attributed to flow separation. This could be illustrated by observing W9's C_L/C_D performance. At $Re \approx 150{,}000$, it ranked second worst and became the best at $Re \approx 200{,}000$, as seen in Figure 5.21 (B) and (C). With the flow around the wings becoming detached, serrations would play a minor role on affecting a sample's aerodynamic performance. Therefore, most of the analysis in this project focused primarily on low α, pre-separation.

In summary, W11 and W13 demonstrated to be most consistently the two best configurations analyzed in this thesis, when considering pre-flow separation conditions. While W11's improved performance was related to the benefits of the bird feather-like serrations, W13's outstanding results were considered to be mostly influenced by the implementation of a tapered TE. This became evident by contrasting the results between W12 (serrated blunt TE) and W13 (serrated tapered TE), with W13 regularly outperforming W12 in the parameters analyzed.

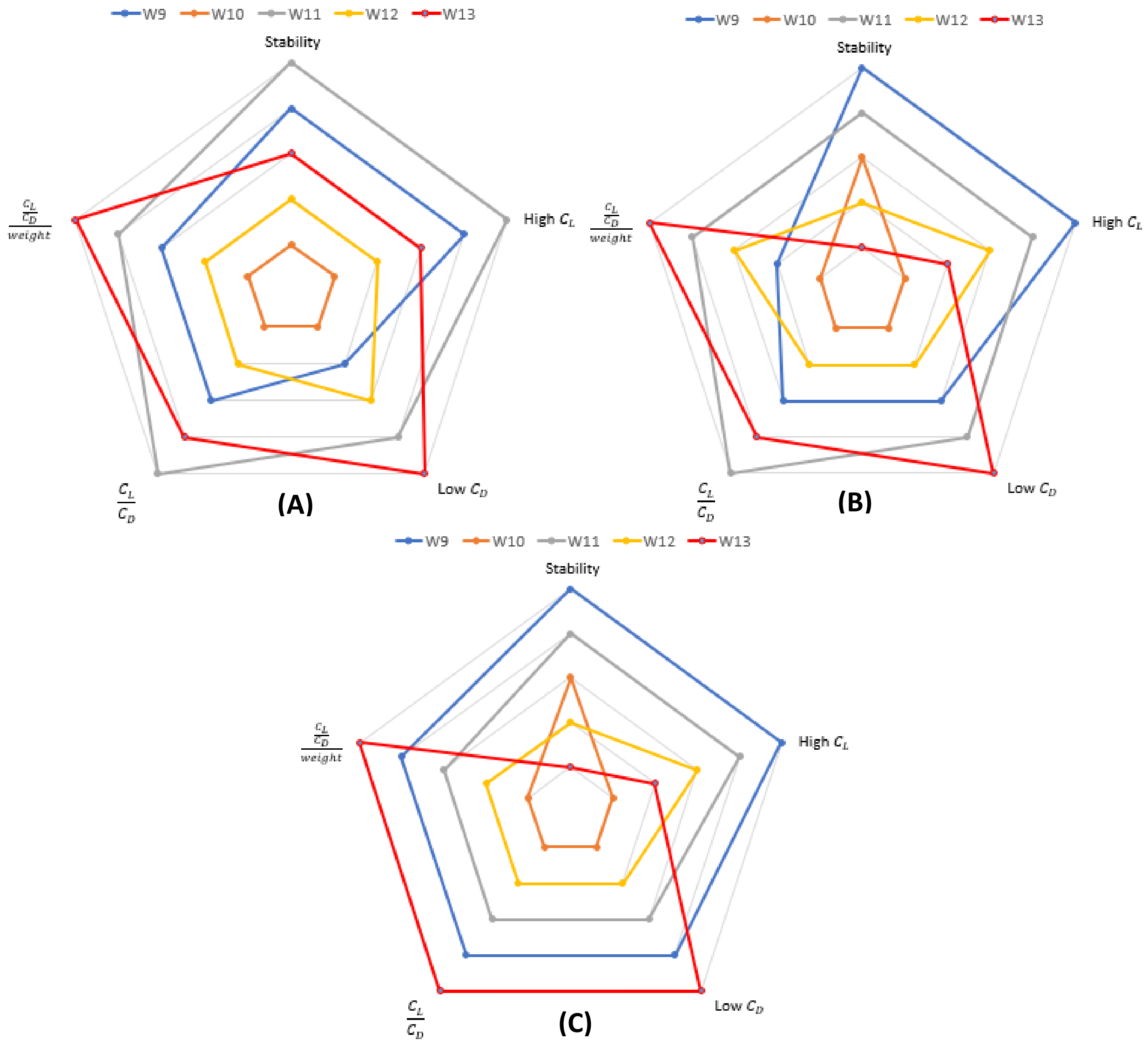

Figure 5.20. Wing performance, α < 10˚, *Re* ≈ (A) 1x10^5, (B) 1.5x10^5, (C) 2x10^5 [2].

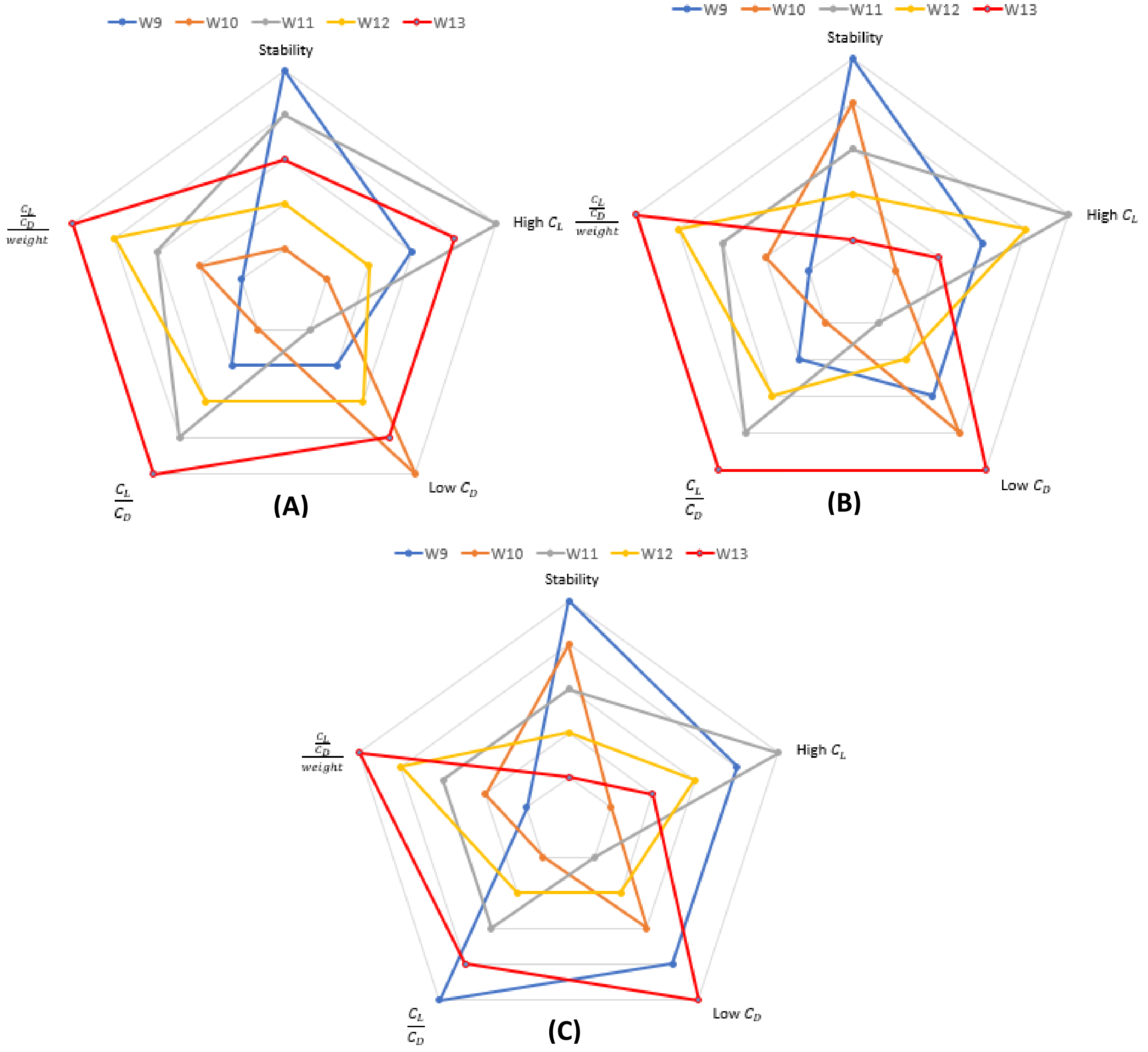

Figure 5.21. Wing performance, α ≥ 10˚, *Re* ≈ (A) $1\text{x}10^5$, (B) $1.5\text{x}10^5$, (C) $2\text{x}10^5$ [2].

5.8 FLOW VISUALIZATION

For the flow visualization, two methods were used with (i) tufts serving as a primary tool and (ii) smoke visualization as a secondary one. This was done as the tufts allowed for continuous 3D observations of the flow past the wing section across all α. The smoke visualization, aided by a laser, contributed to a more specific detailing of the flow field on a 2D plane.

The tufts observations allowed for some comparisons. The moment in which the separation bubble and full separation were noticed gradually changed to a slightly higher α as *Re* increased (see Figure 5.22). The smoke visualization images contributed to the comprehension of this process (see Figure 5.23). At $\alpha = 7.5^\circ$ a separation bubble was noticed, where the flow near the LE started to separate but later reattached to the wing's surface (see blue arrows at the left column of Figure 5.23). Full separation, then, happened at $\alpha \geq 10^\circ$, as highlighted by the blue arrows at the right column of Figure 5.23. Table 5.7 summarizes stall angles for each sample.

Regarding the visual difference observed when considering changes in the TE configuration, the focus shifted to the second row of tufts, nearest to the TE, capable of showing regional effects caused by the serrations. For this reason, a focus on a specific α between 7.5° and 10° was key. Figure 5.24 presents a comparison between all wing configurations at $\alpha = 8.5^\circ$ and $Re \approx 100{,}000$ ($U_\infty = 15$ m/s). Small variations were observed in most cases with the main exception being W13 with its tapered TE which indicated delayed separation when contrasted with the others. This suggested an aerodynamic benefit from the tapered configuration.

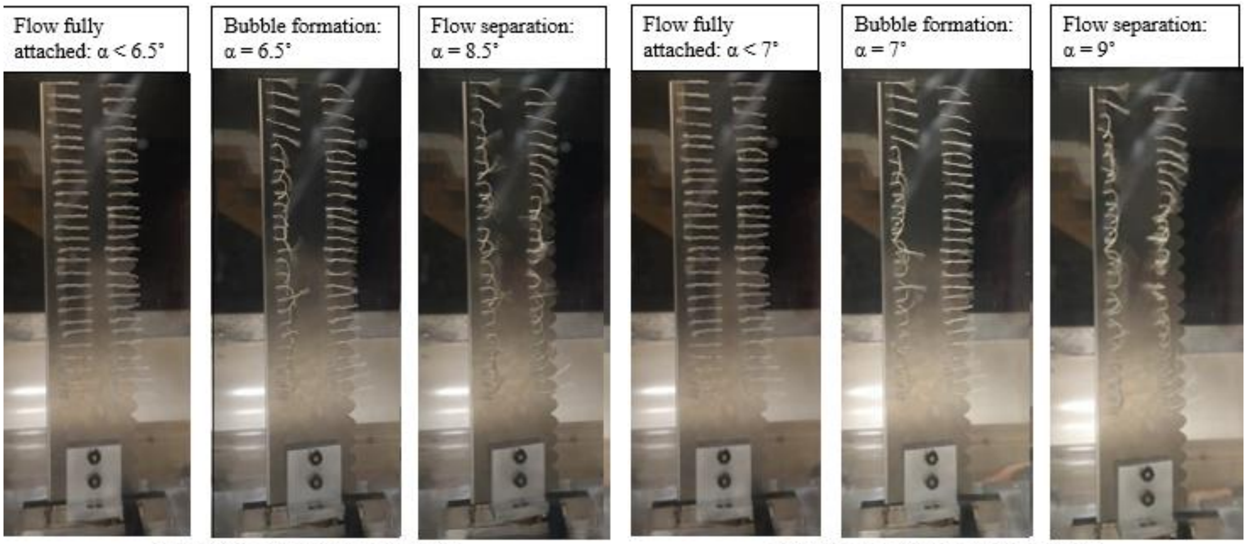

W11 at U∞ = 15 m/s ($Re \approx 100,00$) W11 at U∞ = 22.5 m/s ($Re \approx 150,00$)

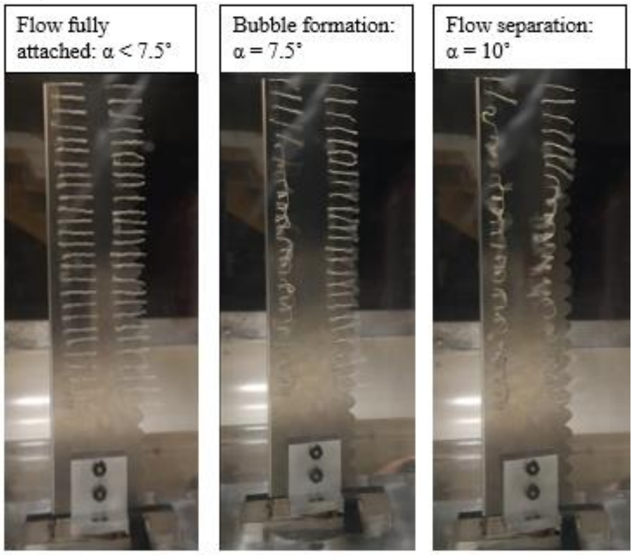

W11 at U∞ = 30 m/s ($Re \approx 200,00$)

Figure 5.22. Flow past W11: fully attached, separation bubble and full separation.

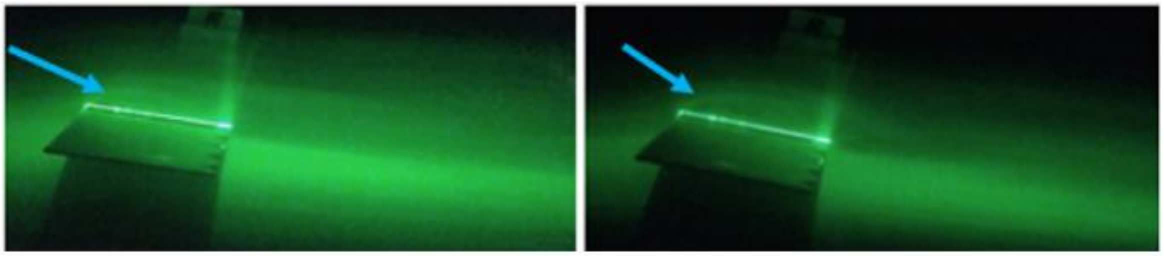

$\alpha = 7.5^\circ$, $Re \approx 100{,}000$ **$\alpha = 10^\circ$, $Re \approx 100{,}000$**

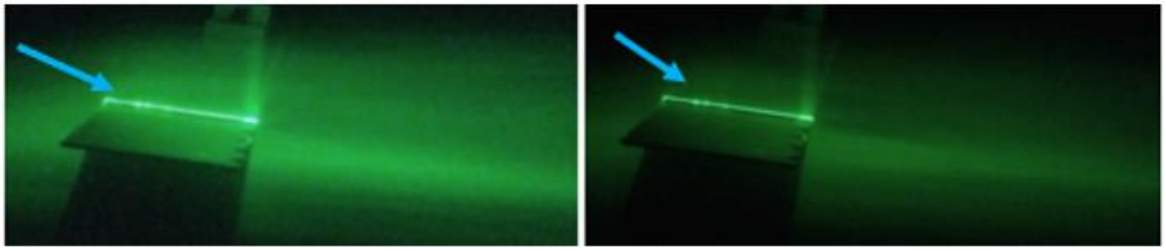

$\alpha = 7.5^\circ$, $Re \approx 150{,}000$ **$\alpha = 10^\circ$, $Re \approx 150{,}000$**

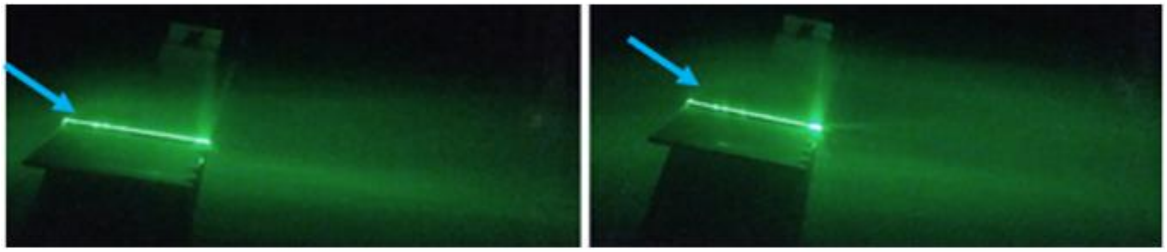

$\alpha = 7.5^\circ$, $Re \approx 200{,}000$ **$\alpha = 10^\circ$, $Re \approx 200{,}000$**

Figure 5.23. Flow past W11: separation bubble and full separation (smoke + laser) [2]

Table 5.7. Wing section dimensions for the 3'x3' WT.

Wing ID	**Re**	**Partial separation**	**Full separation**
W9	1×10^5	$\alpha = 6.5^\circ$	$\alpha = 9^\circ$
W9	1.5×10^5	$\alpha = 7^\circ$	$\alpha = 9^\circ$
W9	2×10^5	$\alpha = 7^\circ$	$\alpha = 9.5^\circ$
W10	1×10^5	$\alpha = 7^\circ$	$\alpha = 8.5^\circ$
W10	1.5×10^5	$\alpha = 7^\circ$	$\alpha = 8.5^\circ$
W10	2×10^5	$\alpha = 7^\circ$	$\alpha = 9^\circ$
W11	1×10^5	$\alpha = 6.5^\circ$	$\alpha = 8.5^\circ$
W11	1.5×10^5	$\alpha = 7^\circ$	$\alpha = 9^\circ$
W11	2×10^5	$\alpha = 7.5^\circ$	$\alpha = 10^\circ$
W12	1×10^5	$\alpha = 6.5^\circ$	$\alpha = 9^\circ$
W12	1.5×10^5	$\alpha = 7^\circ$	$\alpha = 9^\circ$
W12	2×10^5	$\alpha = 7^\circ$	$\alpha = 9^\circ$
W13	1×10^5	$\alpha = 7.5^\circ$	$\alpha = 9.5^\circ$
W13	1.5×10^5	$\alpha = 7.5^\circ$	$\alpha = 9.5^\circ$
W13	2×10^5	$\alpha = 7.5^\circ$	$\alpha = 10^\circ$

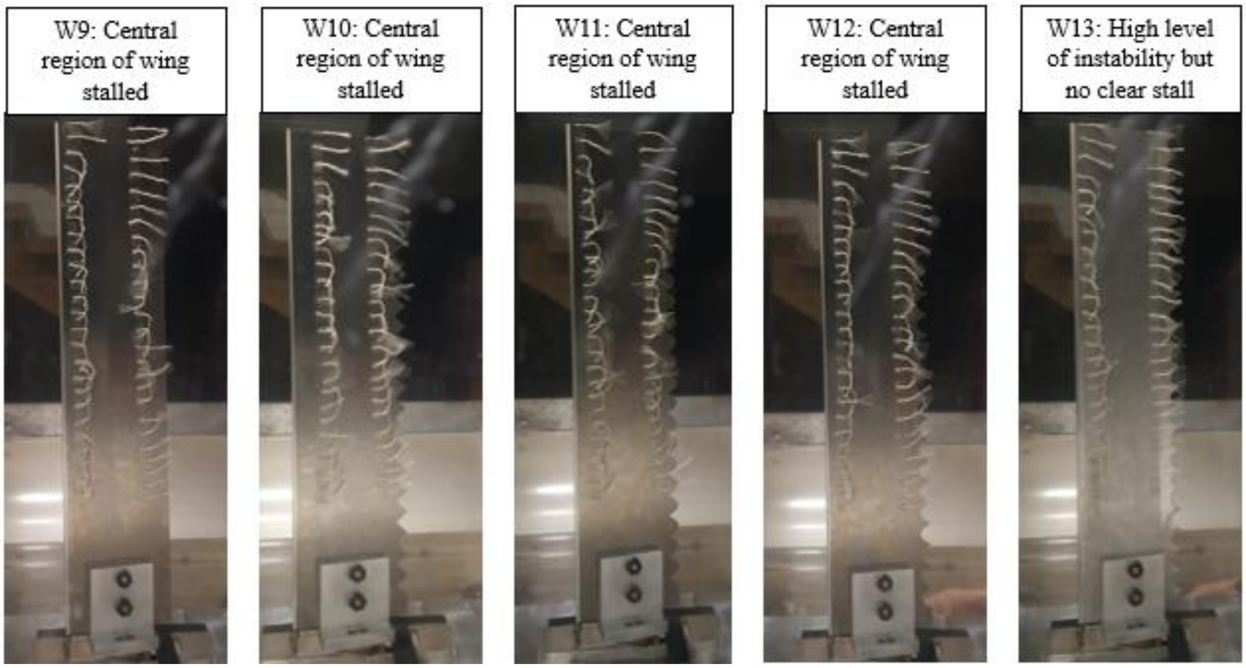
W9: Central region of wing stalled

W10: Central region of wing stalled

W11: Central region of wing stalled

W12: Central region of wing stalled

W13: High level of instability but no clear stall

Figure 5.24. Comparison of flow state between different wings, $\alpha = 8.5^{\circ}$, $Re \approx 100{,}000$

Chapter 6. CONCLUSIONS

This thesis evaluated the influence of different serrated TEs in the aerodynamic performance of wing sections at low *Re*, flight conditions analogous to MAVs. Chapters 1 and 2 respectively provided an overview of the inspiration for this project as well as a background on existing literature relevant to the research on serrated TEs for wings at low *Re*, below 200,000. As identified in previous studies, the expected benefits associated with the introduction of these passive aerodynamic devices, such as drag reduction, were discussed. Chapter 3 described the test samples used for this project, including one control flat plate and a series of serrated specimens with varying d, λ, and shape of serrations. The quantitative and qualitative experimental setups at the µWT and 3’ x 3’ WT were explained.

Two methods of testing were performed at the µWT: wake survey and force balance measurements. In total, eight samples with differing d, λ, and shape were designed and tested, at a $Re < 40{,}000$. These two sets of tests provided an understanding of the flow behavior past each wing section and of their aerodynamic performance. Together they were successful at identifying a few points:

- Key stages in the flow development were noticed such as signs of flow separation occurring at $5^\circ < \alpha \leq 10^\circ$.
- Large d (W4) proved to have a negative impact on the sample’s performance by primarily reducing C_L of such a wing section.
- There was a noticeable impact related to the frequency by which the pair of streamwise counterrotating vortices generated by TE serrations and the aerodynamic performance of the samples tested. The optimal configuration, W5, was that which avoided both the extremes of narrow and wide serrations.

- W5 represented the best combination of *d* and λ (C_L/C_D 9% higher than baseline W1 at $\alpha = 5^\circ$). This allowed for the subsequent phases of this project to be focused on serration shape while maintaining the same proportions of *d* and λ.

The tests performed at the μWT were followed by a series of tests at the 3' x 3' WT facility at the University of Washington. In this case, the *Re* considered were higher, set at 100,000, 150,000 and 200,000. Qualitative and quantitative studies were conducted. This included flow visualization aided by smoke and tufts, and force measurements, using an ATI Mini45. There were five samples fabricated: a baseline sample W9, three differently shaped serrations — triangular W10, bird feather-like W11 and membrane-like W12 —, and W13 which consider the effect of combining TE tapering with serrations. The 3' x 3' WT results led to a few conclusions:

- There was a correlation between raising *Re* from 100,000 to 200,000 and a decrease in the beneficial aerodynamic impact associated with employing serrated TEs. For example, W11's $\Delta C_L/C_D$ relative to W9 went from a 15% improvement ($Re \approx 100{,}000$ and $\alpha = 5^\circ$) to a decline measured at -7.5% ($Re \approx 200{,}000$ and $\alpha = 5^\circ$). This was attributed to the significant changes related to flow characteristics, including a decrease in boundary layer thickness, which impacted wing sections at low *Re* ranges, as described in Chapter 2 and observed in Chapter 5.
- Post flow separation ($\alpha \geq 10^\circ$), the serrations' impact in aerodynamic performance was minor and, therefore, most of the attention related to studying serrated TEs in this project focused on low α.
- The stable tendency present for all specimens tested generally decreased with the introduction of serrations. The more intense negative C_M-α curve for W9 indicated higher

stability compared to W10-W13. W10 exemplified this scenario well, with a ΔC_M increase of 0.014 relative to W9 between $\alpha = 0^\circ$ ($\Delta C_M = 0.015$) and $\alpha = 7.5^\circ$ ($\Delta C_M = 0.029$) at $Re \approx 100{,}000$.

- The shape of serration proved to have a significant impact on the performance of these wing sections. Among the shapes tested, W11's bird feather-like serrations yielded best results. W11's C_L/C_D reached a 62% improvement when compared to W10 at $Re \approx 100{,}000$ and $\alpha = 5^\circ$. This difference was attributed to the change in intensity of the serration-generated vortices. Further studies on this area would provide additional insight.
- W11 and W13 yielded the best results out of the models studied. W11 outperformed the baseline W9, reaching a maximum $\Delta C_L/C_D = 1.44$ at $Re \approx 100{,}000$ and $\alpha = 2.5^\circ$. Meanwhile, W13 achieved a $\Delta C_L/C_D = 0.80$ relative to W9 at the same flow conditions.
- The combination of serrated and tapered TE was considered effective. Comparing W13 (tapering + serrations) and W12 (serrations only), a maximum $\Delta C_L/C_D = 1.43$ was achieved at $Re \approx 100{,}000$ and $\alpha = 2.5^\circ$.
- The flight efficiency of W11 and W13 was magnified. This was a result of weight reductions for all serrated samples ranging from 3% for W11 to 13% in the case of W13. W11's $(C_L/C_D)/weight$ accounted for a 19% improvement relative to W9 at $Re \approx 100{,}000$ and $\alpha = 5^\circ$.

In summary, this thesis was successful at confirming the hypothesis that the two topologies inspired by natural shapes, the membrane-like (W12) and bird feather-like serrations (W11), presented improvements over the triangular shaped ones (W10). W13 also represented an improvement over W10. It was also confirmed that properly serrated TE wing sections, such as W11 and W13, could aerodynamically outperform W9, given a low $Re \leq 150{,}000$. This made such designs applicable to fixed-wing MAVs flying at $45{,}000 \leq Re \leq 180{,}000$. As expected, these aerodynamic improvements were linked to a C_D reduction. Therefore, the positive performance of serrated wings at low *Re*, partnered with affordable manufacturing processes such as 3d-printing and small-scale CNC, makes employing TE serrations at fixed-wing MAVs economically viable.

Chapter 7. FUTURE WORK

The potential next steps following this thesis would focus on flow conditions of $Re \leq 150{,}000$. It is suggested that these tests combine the features deemed to provide the best impact on the wing section's aerodynamic performance: bird feather-like serrations and tapered TE. In order to evaluate this, three samples are recommended: (i) baseline wing, (ii) bird feather-like serrated TE wing and (iii) bird feather-like serration + tapering.

Based on the outcome of this study, another evaluation could be performed. This would compare the aerodynamic impact of TE serrations in a thick versus a thin profile wing. While thin profiles are generally used for fixed-wing MAVs, understanding the potential impact of wing profile thickness on the effectiveness of TE serrations would be useful as there is still a minority of MAVs employing thicker wing profiles. The effects of employing serrated TE at a cambered thin plate would also be recommended for further analysis.

More studies investigating the effects of varying the flow's boundary layer thickness on C_D reduction associated with employing of TE serrations are also proposed. By adjusting *Re*, and experimentally measuring the boundary layer thickness as flow conditions changed while collecting data on C_L and C_D would further contribute to quantifying its impact on the aerodynamic performance of serrated wing samples. This would, therefore, expand upon the discussion in this thesis project, on how changing *Re* affects the performance of TE serrations.

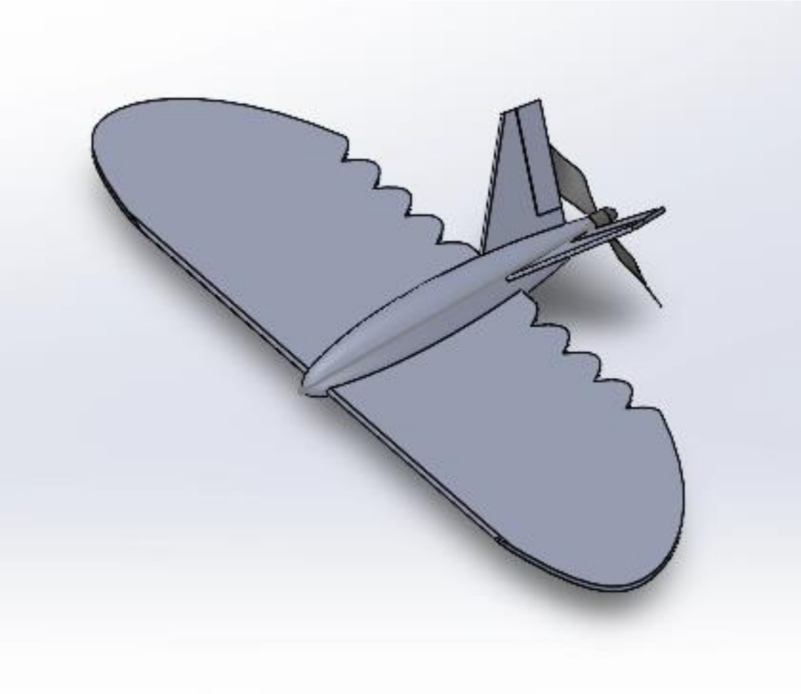

Figure 7.1. Prototype fixed-wing MAV concept.

Finally, a prototype of a fixed-wing MAV could be designed, employing serrated TEs in a configuration that resembles that of an owl [8]. A potential concept model is presented in Figure 7.1. The performance of a prototype like this could be evaluated according to various real-world conditions, aiming at an average *Re* ≤ 150,000. In-flight measuring systems, such as accelerometers, could be used for data collection to validate the results from wind tunnel testing.

BIBLIOGRAPHY

[1] Bron Simplicio, I., Nino, G. F., and Breidenthal, R., "Aerodynamic Effects of Trailing Edge Serrations on a Wing at Low Reynolds Number-Work in Progress," *AIAA PNW Section, 2020 Tech Symposium Poster*, Nov. 2020.

[2] Bron Simplicio, I., Nino, G. F., and Breidenthal, R., "Aerodynamic Effects of Trailing Edge Serrations at Low Reynolds Numbers," AIAA 2022-1957. *AIAA SCITECH 2022 Forum*, Jan. 2022.
https://doi.org/10.2514/6.2022-1957

[3] Wier, S. K., "Superbly Small: Alberto Santos-Dumont and his Demoiselle Airplanes," May 2019.
http://www.westernexplorers.us/Demoiselle-original-history.pdf

[4] Raffel, M., Wienke, F., and Dillmann, A., "Flight-Testing Stability and Controllability of Otto Lilienthal's Monoplane Design from 1893," *AIAA, Journal of Aircraft*, Jun. 2019.
https://doi.org/10.2514/1.C035399

[5] Bartoli, G., Borsani, A., Borri, C., Martelli, A., Procino, L., Vezzosi, A., "Leonardo, the wind and the flying sphere," *5th European and African Conference on Wind Engineering,* Jul. 2009.

[6] Thomareis, N., and Papadakis, G., "Effect of trailing edge shape on the separated flow characteristics around an airfoil at low Reynolds number," *Physics of Fluids*, Vol. 29, Jan. 2017.
https://doi.org/10.1063/1.4973811

[7] Hedenström, A., and Johansson, L. C., "Bat flight: aerodynamics, kinematics and flight morphology," *Journal of Experimental Biology*, Mar. 2015.
https://doi.org/10.1242/jeb.031203

[8] "Owl wing design reduces aircraft, wind turbine noise pollution," Available:
https://phys.org/news/2022-01-owl-wing-aircraft-turbine-noise.html

[9] Fish, F. E., and Battle, J. M., "Hydrodynamic design of the humpback flipper," *Journal of Morphology*, Jul. 1995.
https://doi.org/10.1002/jmor.1052250105

[10] Fish, F. E., Weber, P. W., Murray, M. M., and Howle, L. E., "The Tubercles on Humpback Whales' Flippers: Application of Bio-Inspired Technology," *Integrative and Comparative Biology,* Vol. 51, No. 1, May 2011.
https://doi.org/10.1093/icb/icr016

[11] Lee, S., and Lee, S., "Wind turbine noise reduction by means of serrated trailing edges," INTER-NOISE and NOISE-CON Congress and Conference Proceedings, Vol. 2012, No. 9, Aug 2012 pp. 2283–2288.
http://aancl.snu.ac.kr/aancl/research/International%20Conference/100.pdf

[12] Llorente, E., and Ragni, D., “Trailing-edge serrations effect on the performance of a wind turbine.” *Renewable Energy*, Vol. 147, 2020. https://doi.org/10.1016/j.renene.2019.08.128

[13] “NASA Helps Create a More Silent Night”, NASA, Available: https://www.nasa.gov/topics/aeronautics/features/bridges_chevron_events.html.

[14] “Mercedes brings serrated rear wing design back”, Motorsport, Available: https://www.motorsport.com/f1/news/mercedes-serrated-wing-azerbaijan/4375718/

[15] Michelson, R. C., “Overview of Micro Air Vehicle System Design and Integration Issues,” *Encyclopedia of Aerospace Engineering*, Sept. 2010. https://doi.org/10.1002/9780470686652.eae401

[16] Galinski, C., “Influence of MAV characteristics on their applications,” *Aviation,* Vol. 9, No. 4, 2005. https://doi.org/10.1080/16487788.2005.9635913

[17] “The NACA airfoil series,” Stanford, Available: https://web.stanford.edu/~cantwell/AA200_Course_Material/The%20NACA%20airfoil%20series.pdf

[18] De Paula, A. A., “The airfoil thickness effects on wavy leading edge phenomena at low Reynolds number regime,” Ph.D. Dissertation, Technischen Universität Berlin, 2016. www.teses.usp.br

[19] Houghton, E. L., Carpenter, P. W., Collicott, S. H., and Valentine, D. T., “Aerodynamics for Engineering Students,” 6th ed., Elsevier, Waltham, 2013.

[20] Tanner, M., “REDUCTION OF BASE DRAG,” Progress in Aerospace Sciences, Vol. 16, No. 4, 1975, pp. 369–384. https://doi.org/10.1016/0376-0421(75)90003-2

[21] Anusha, K., and Thanigaiarasu, S., “Computational Analysis of Blunt Trailing Edge NACA 0012 Airfoil,” *International Journal of Advanced Research in Biology Engineering Science and Technology (IJARBEST),* Vol. 2, No. 14, Nov. 2015. https://www.ijarbest.com/conference/spcl14/770

[22] Nedić, J., and Vassilicos, J. C., “Vortex Shedding and Aerodynamic Performance of Airfoil with Multiscale Trailing-Edge Modifications,” Annual Review of Fluid Mechanics, Vol. 53, No. 11, Nov. 2015. https://doi.org/10.2514/1.J053834

[23] Vijgen, P. M. H. W., Howard, F. G., Bushnell, D. M., and Holmes, B. J., “Serrated Trailing Edges For Improving Lift And Drag Characteristics Of Lifting Surfaces,” *U.S. Patent No.5088665,* February 18, 1992.

[24] Obrecht, J. M., and Steingrimsson, A. T., “Trailing Edge Modifications For Wind Turbine Airfoil,” *U.S. Patent No.9670901 B2,* June 6, 2017.

[25] Pechlivanoglou, G., “Passive and active flow control solutions for wind turbine blades,” Ph.D. Dissertation, Technischen Universität Berlin, 2013.

[26] Hussian, U., Malook, S. U., Shabir, B., Ali, O., and Ahmad, S. M., “Effect of trailing edge serration on the lift and drag characteristics of NACA0012 airfoil wing,” AIAA AVIATION Forum, 35th AIAA Applied Aerodynamics Conference, 5–9 Jun. 2017. https://doi.org/10.2514/6.2017-4470

[27] Moreau, D. J., and Doolan, C. J., “On the noise reduction mechanism of a flat plate serrated trailing edge,” *AIAA Journal*, Oct. 2013. https://doi.org/0.2514/1.J052436

[28] Loughnane, F. A., Supina, R., Mongin, M. P., and Gunasekaran, S. "Effect of Airfoil-Preserved Undulations on Wing Performance," *AIAA Scitech 2020 Forum*, Jan. 2020. https://doi.org/10.2514/6.2020-1784

[29] Liu, X., Jawahar, H. K., Azarpeyvand, M., and Theunissen, R., "Wake Development of Airfoils with Serrated Trailing Edges," AIAA 2016-2817. *22nd AIAA/CEAS Aeroacoustics Conference*. May 2016. https://doi.org/10.2514/6.2016-2817

[30] Mueller, T. J., and DeLaurier, J. D., “Aerodynamics of Small Vehicles,” *AIAA Journal*, Vol. 35:89-111, Jan. 2003. https://doi.org/10.1146/annurev.fluid.35.101101.161102

[31] Koning, W. J., Romander, E. A., and Johnson, W., "Optimization of Low Reynolds Number Airfoils for Martian Rotor Applications Using an Evolutionary Algorithm," AIAA 2020-0084. *AIAA Scitech 2020 Forum*. Jan. 2020. https://doi.org/10.2514/6.2020-0084

[32] Lissaman, P. B. S., “LOW-REYNOLDS-NUMBER AIRFOILS,” *Annual Review of Fluid Mechanics*, vol. 15, Jan. 1983, pp. 223–239 https://doi.org/10.1146/annurev.fl.15.010183.001255

[33] Carmichael, B. H., “Low Reynolds Number Airfoil Survey, Volume 1,” NASA Contractor Report 165803, Low Energy Transportation Systems Capistrano Beach, CA, 1982.

[34] Yarusevych, S., Sullivan, P. E., and Kawall, J. G., “On vortex shedding from an airfoil in low-Reynolds-number flows,” *Journal of Fluid Mechanics*, Vol. 632, 2009, pp. 245-271. https://doi.org/10.1017/S0022112009007058

[35] McMasters, J., and Henderson, M., “Low-Speed Single-Element Airfoil Synthesis,” *Technical Soaring*, Vol. 6, No. 2, 1979, pp. 1–21.

[36] Wilcox, D. C., “Basic Fluid Mechanics,” 5th ed., DCW Industries, 2012.

[37] Placek, R., “Errors and problems while conducting research studies in a wind tunnel-selected examples,” *Transactions of the Institute of Aviation*, Vol. 245, No. 4, Dec. 2016, pp. 169-177.
https://doi.org/10.5604/05096669.1226885

[38] Barlow, J. B., William Jr., H. R., Pope, A., “Low-Speed Wind Tunnel Testing,” 3rd ed., John Wiley & Sons, 1999.

[39] “Types of Wind Tunnels”, NASA, Available:
https://www.grc.nasa.gov/www/k-12/airplane/tuntype.html

[40] Santos, L., Avelar, A., Chiseaki, M., and Mello, O, “Drag Estimation by Wake Survey Performed Measuring Velocities and Measuring Total and Static Pressures,” *11th Brazilian Congress of Thermal Sciences and Engineering*, Dec. 2006.

[41] Pifer, E. A., and Bramesfeld, G., "Measuring Wing Profile Drag Using an Integrating Wake Rake," *Technical Soaring*, Vol. 36, No. 3, 2012.
https://journals.sfu.ca/ts/index.php/ts/article/view/289/271

[42] Talamelli, A., “Drag Measurements Through Wake Analysis”, Mar. 2015.
http://www2.mech.kth.se/courses/5C1211/labInstr06.pdf

[43] “AIRFOIL DRAG BY WAKE SURVEY USING LDV”, University of Toronto, Available:
http://www.aerospace.utoronto.ca/pdf_files/closed_subsonic.pdf

[44] “Internal Force Balance”, NASA, Available:
https://www.grc.nasa.gov/www/k-12/airplane/tunbalint.html

[45] Tintoré, I. B., “Design of a Three-axis Wind Tunnel Force Balance”, Undergraduate Thesis, University of Zagreb, Jul. 2018.
https://urn.nsk.hr/urn:nbn:hr:119:249595

[46] Post, S., and Morris, M., “Force Balance Design For Educational Wind Tunnels,” 2010 ASEE Annual Conference, Jun. 2010
https://doi.org/10.18260/1-2--15891.

[47] Tomin, M., Scipioni, M., and Gatti, B., “Design, Construction and Testing of a 3-Component Force Balance for Educational Wind Tunnels in Undergraduate Aerodynamics,” *Journal of Aviation/Aerospace Education & Research*, Vol. 29, No. 1, 2020.
https://doi.org/10.15394/jaaer.2020.1809.

[48] Weber, L., Nino, G., Han, B., and Breidenthal, R., "Manipulation of Streamwise Vortices by Air Injection on Vortex Generators," AIAA 2021-1193, *AIAA Scitech 2021 Forum*. Jan. 2021.
https://doi.org/10.2514/6.2021-1193

[49] Schroeder, E. J., “Low Reynolds Number Flow Validation Using Computational Flow Dynamics with Application to Micro Air Vehicles”, Master Thesis, University of Maryland, 2015. https://www.proquest.com/openview/86be02f5ac5c3b8b0607c627c14577df/1?pq-origsite=gscholar&cbl=18750&diss=y

[50] “3x3 Low-Speed Wind Tunnel”, William E. Boeing Department of Aeronautics & Astronautics, Available: https://www.aa.washington.edu/AERL/3x3.

[51] “F/T Sensor: Mini45”, ATI Industrial Automation, Available: https://www.ati-ia.com/products/ft/ft_models.aspx?id=Mini45.

[52] Traub, L. W., and Coffman, C., “Efficient Low-Reynolds-Number Airfoils,” *Journal Of Aircraft,* Vol. 56, No. 5, Sept. 2019. https://doi.org/10.2514/1.C035515

[53] Selig, M. S., Deters, R. W., and Williamson, G. A., “Wind Tunnel Testing Airfoils at Low Reynolds Numbers,” *49th AIAA Aerospace Sciences Meeting*, 4-7 Jan. 2011. https://doi.org/10.2514/6.2011-875

[54] Krentel, D., and Nitsche, W, “Investigation of the near and far wake of a bluff airfoil model with trailing edge modifications using time-resolved particle image velocimetry,” *Experiments in fluids*, Vol. 54, No. 7, May. 2013. https://doi.org/10.1007/s00348-013-1551-1

[55] Smith, H. A. and Schaefer, R. F., “Aerodynamic Characteristics at Reynolds Numbers of 3.0 x 106 and 6.0 x 106 of Three Airfoil Sections Formed by Cutting Off Various Amounts From the Rear Portion of the NACA 0012 Airfoil Section,” *Tech. rep., NACA TN-2074,* 1950.

APPENDIX A: INTRUMENTATION SETUPS

This appendix describes steps used to setup the different experiments performed in this project.

µWT wake survey:

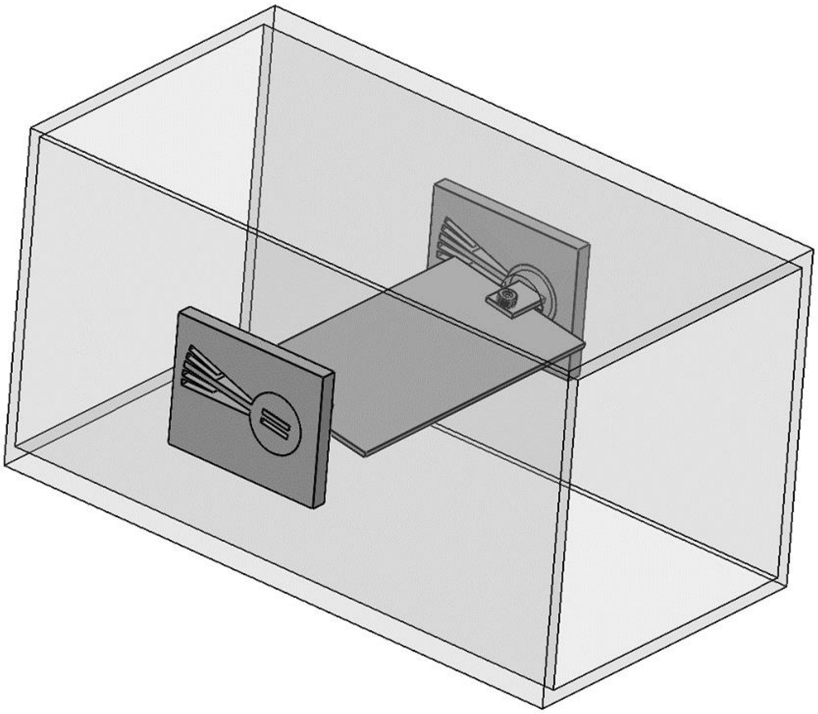

Figure A.1. Fully assembled wake survey wing sample within test section.

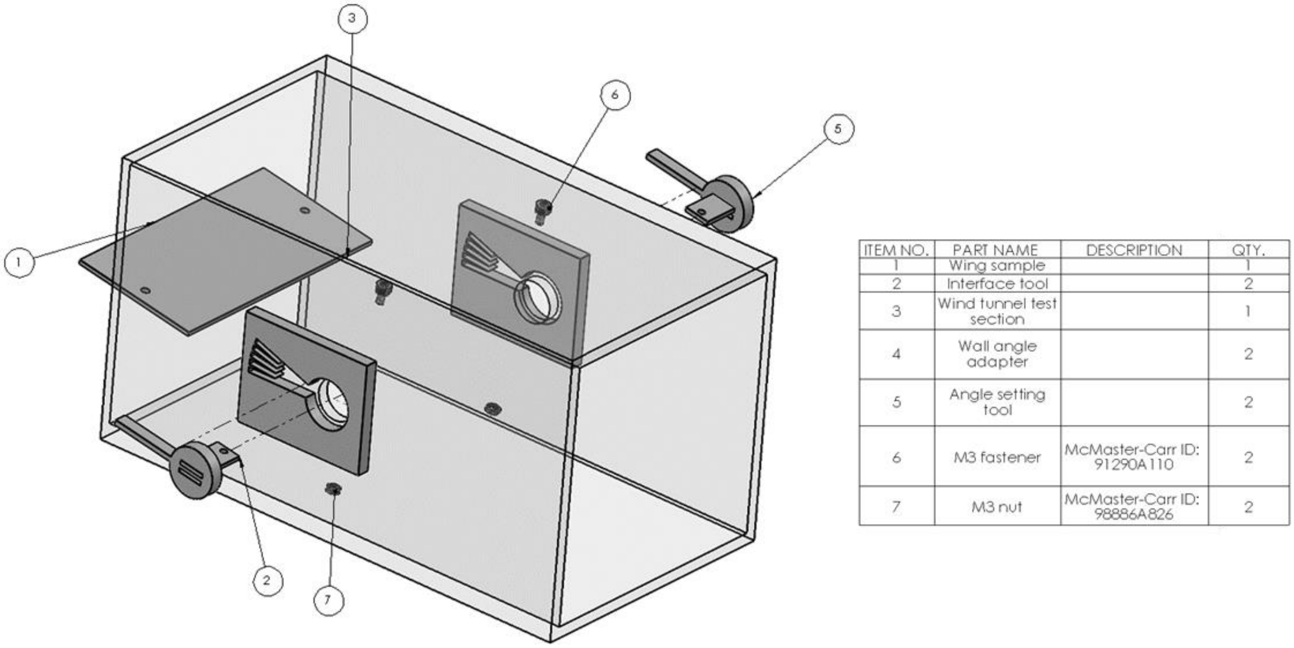

ITEM NO.	PART NAME	DESCRIPTION	QTY.
1	Wing sample		1
2	Interface tool		2
3	Wind tunnel test section		1
4	Wall angle adapter		2
5	Angle setting tool		2
6	M3 fastener	McMaster-Carr ID: 91290A110	2
7	M3 nut	McMaster-Carr ID: 98886A826	2

Figure A.2. Exploded view of assembly with description of parts.

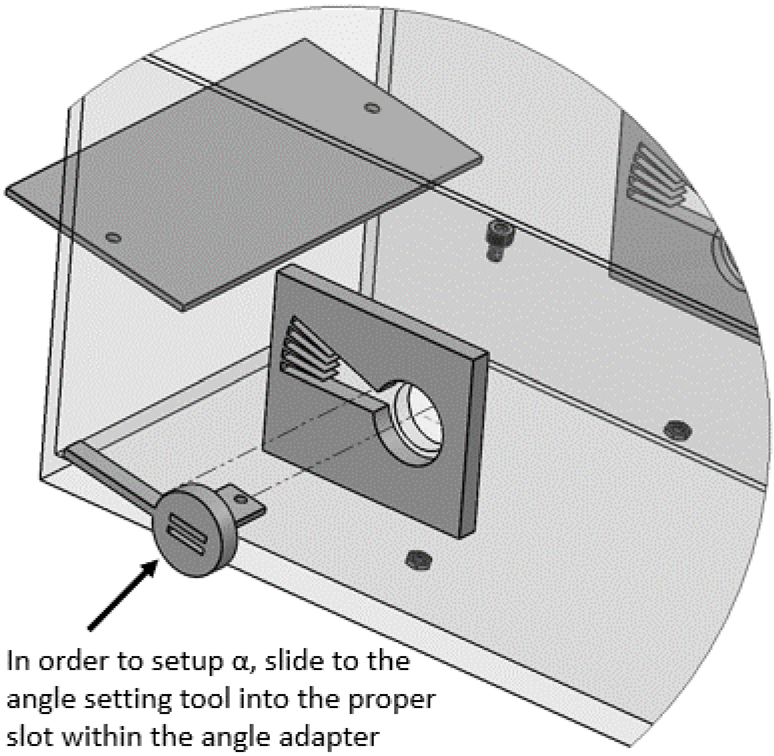

Figure A.3. Detail view of angle adjustment setup (exploded view).

µWT force balance:

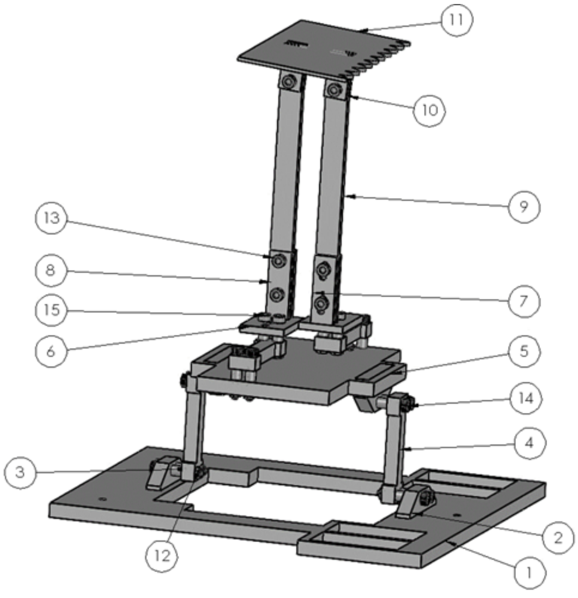

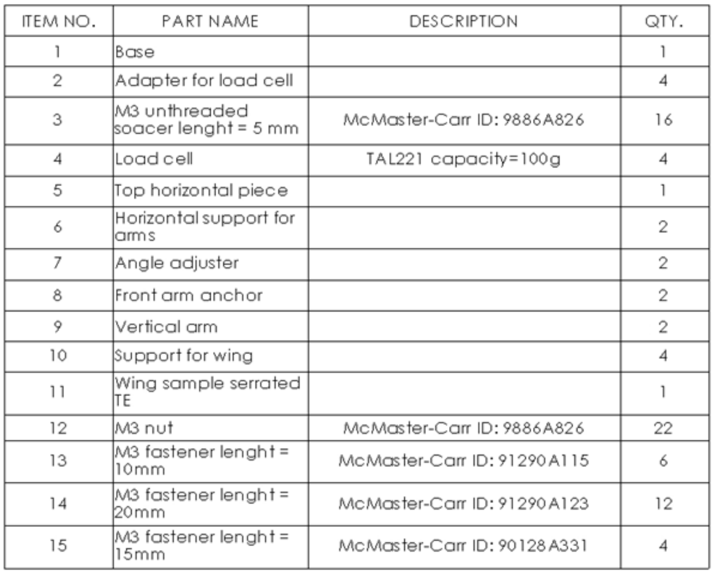

ITEM NO.	PART NAME	DESCRIPTION	QTY.
1	Base		1
2	Adapter for load cell		4
3	M3 unthreaded soacer lenght = 5 mm	McMaster-Carr ID: 9886A826	16
4	Load cell	TAL221 capacity=100g	4
5	Top horizontal piece		1
6	Horizontal support for arms		2
7	Angle adjuster		2
8	Front arm anchor		2
9	Vertical arm		2
10	Support for wing		4
11	Wing sample serrated TE		1
12	M3 nut	McMaster-Carr ID: 9886A826	22
13	M3 fastener lenght = 10mm	McMaster-Carr ID: 91290A115	6
14	M3 fastener lenght = 20mm	McMaster-Carr ID: 91290A123	12
15	M3 fastener lenght = 15mm	McMaster-Carr ID: 90128A331	4

Figure A.4. Fully assembled force balance with description of parts.

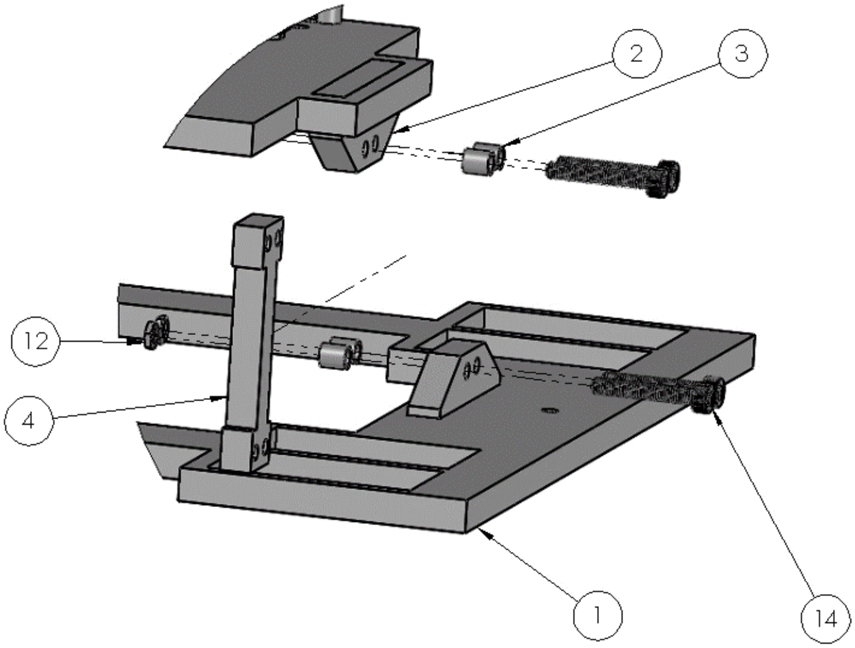

Figure A.5. Detail view of base-drag load cell-intermediary platform (exploded view).

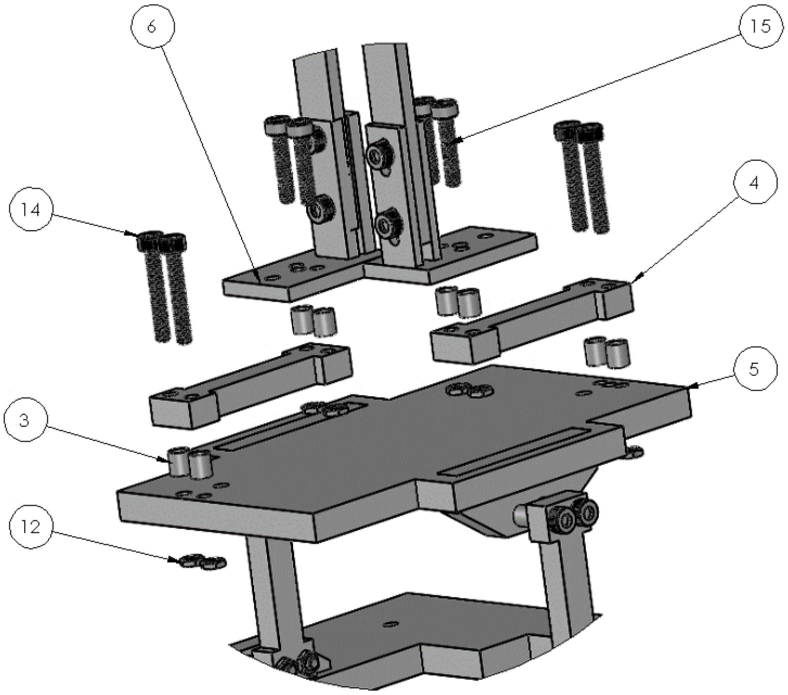

Figure A.6. Detail view of intermediary platform-lift load cell-vertical arm (exploded view).

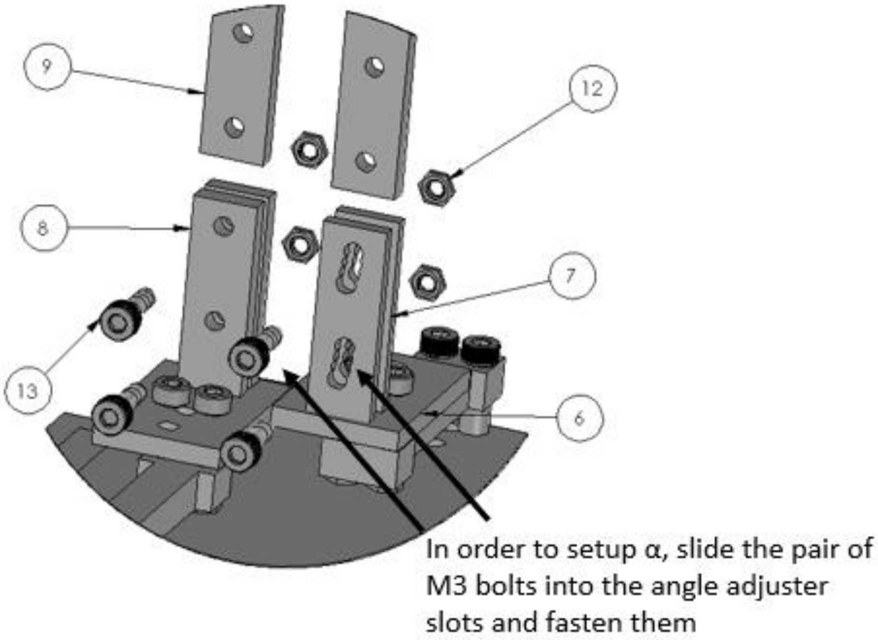

In order to setup α, slide the pair of M3 bolts into the angle adjuster slots and fasten them

Figure A.7. Detail view of the mechanism used for setting the wing samples' α (exploded view).

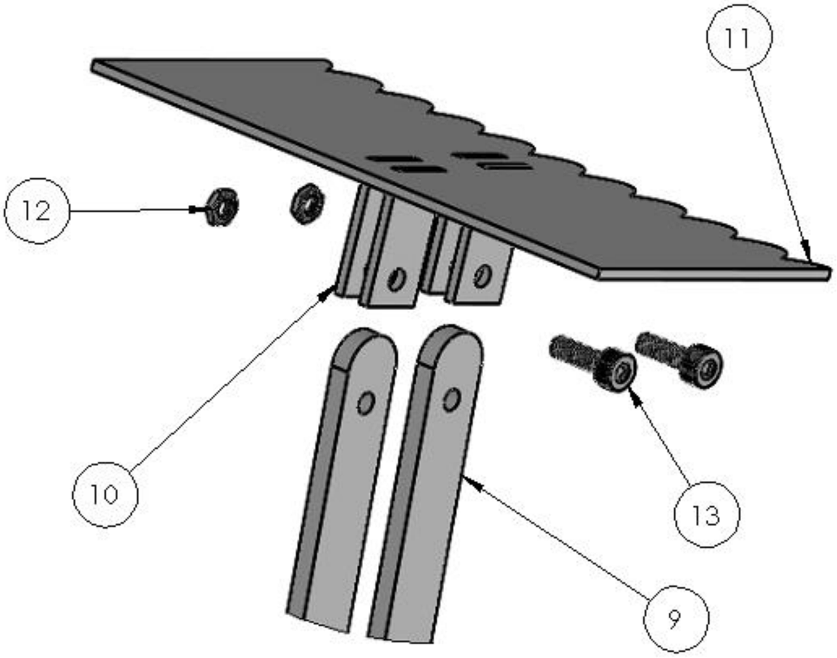

Figure A.8. Detail view of wing sample-vertical arms sub-assembly (exploded view).

3’ x 3’ WT:

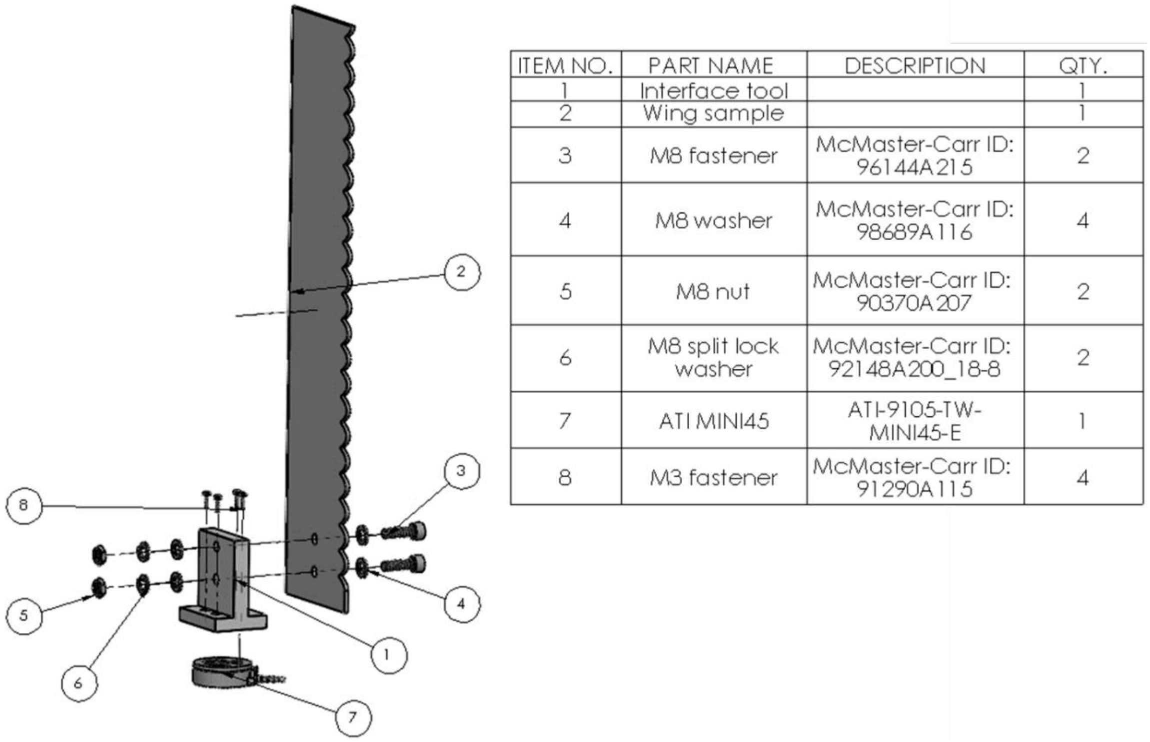

ITEM NO.	PART NAME	DESCRIPTION	QTY.
1	Interface tool		1
2	Wing sample		1
3	M8 fastener	McMaster-Carr ID: 96144A215	2
4	M8 washer	McMaster-Carr ID: 98689A116	4
5	M8 nut	McMaster-Carr ID: 90370A207	2
6	M8 split lock washer	McMaster-Carr ID: 92148A200_18-8	2
7	ATI MINI45	ATI-9105-TW-MINI45-E	1
8	M3 fastener	McMaster-Carr ID: 91290A115	4

Figure A.9. Assembly of 3’ x 3’ WT’s wing setup (exploded view).

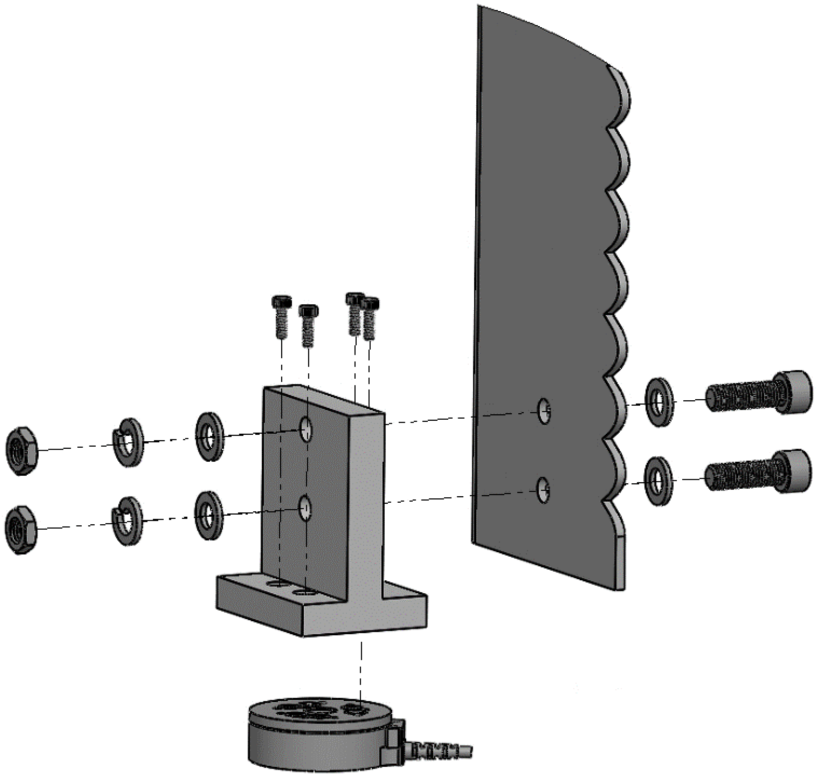

Figure A.10. Detail view of attachment between ATI 45Mini and wing sample (exploded view).

APPENDIX B: INSTRUMENTATION DESIGN AND DRAWINGS

µWT wake survey:

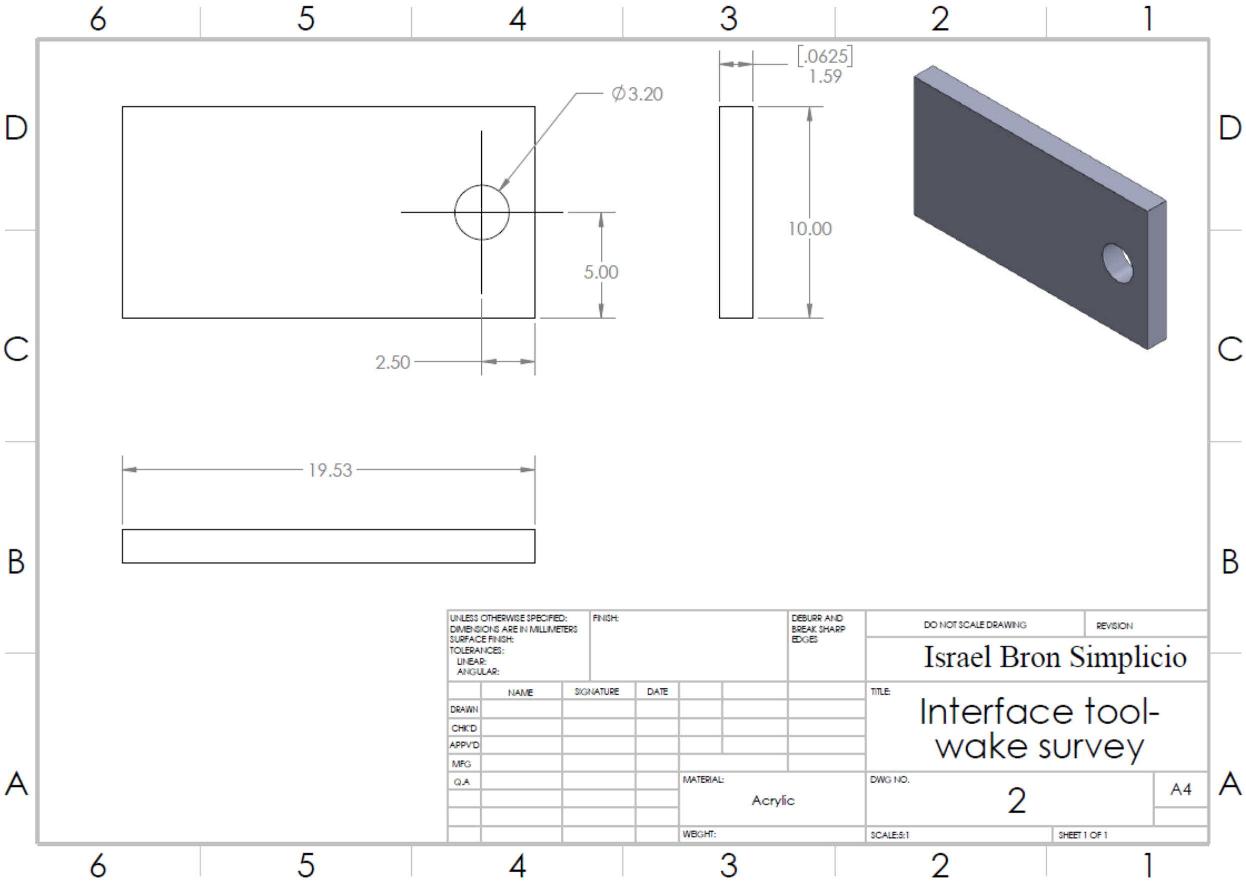

Israel Bron Simplicio

TITLE: Interface tool-wake survey

MATERIAL: Acrylic

DWG NO. 2

A4

SCALE:5:1

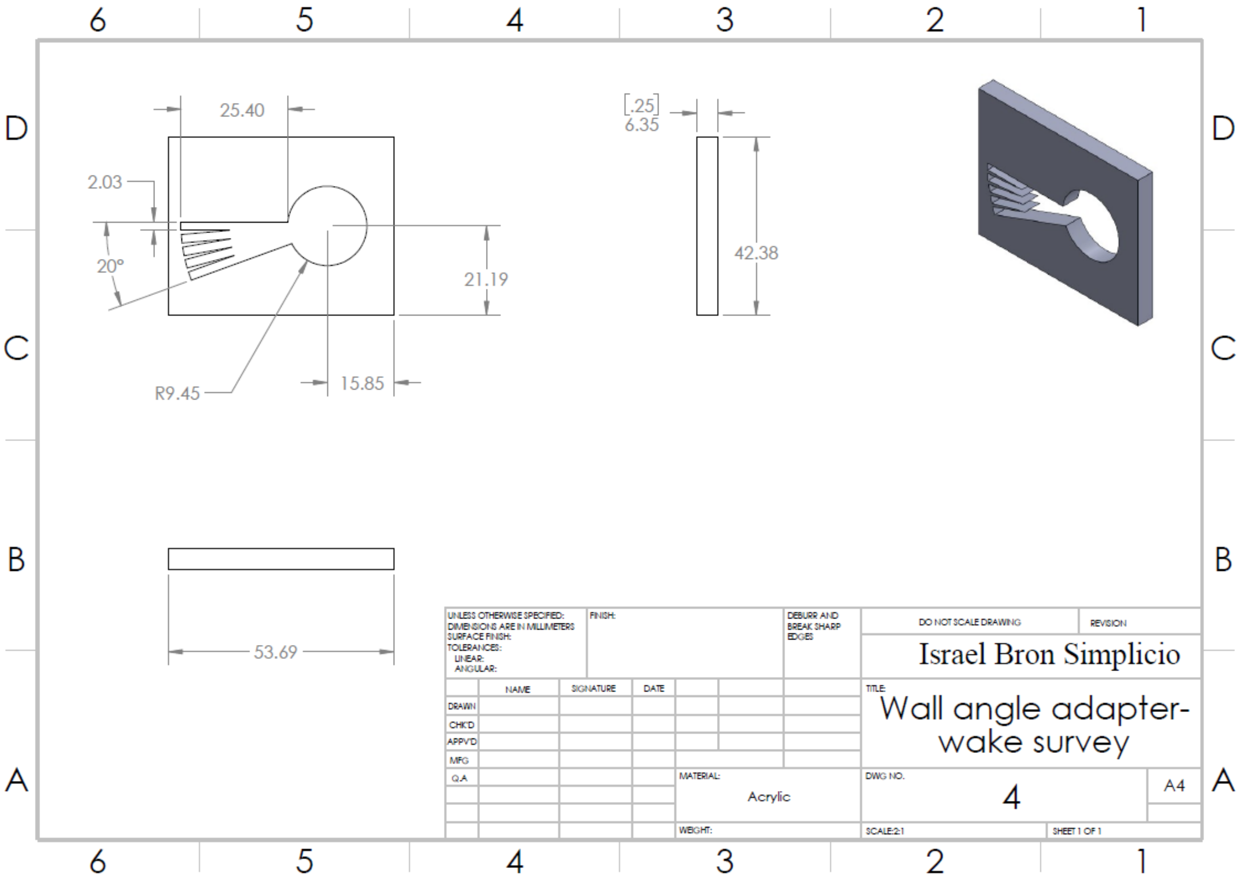
25.40
2.03
20°
R9.45
15.85
21.19
[.25]
6.35
42.38
53.69
UNLESS OTHERWISE SPECIFIED:
DIMENSIONS ARE IN MILLIMETERS
SURFACE FINISH:
TOLERANCES:
LINEAR:
ANGULAR:
FINISH:
DEBURR AND BREAK SHARP EDGES
DO NOT SCALE DRAWING
REVISION
Israel Bron Simplicio
NAME
SIGNATURE
DATE
DRAWN
CHK'D
APPV'D
MFG
Q.A
TITLE:
Wall angle adapter-wake survey
MATERIAL:
Acrylic
DWG NO.
4
A4
WEIGHT:
SCALE:2:1
SHEET 1 OF 1
6
5
4
3
2
1
D
C
B
A

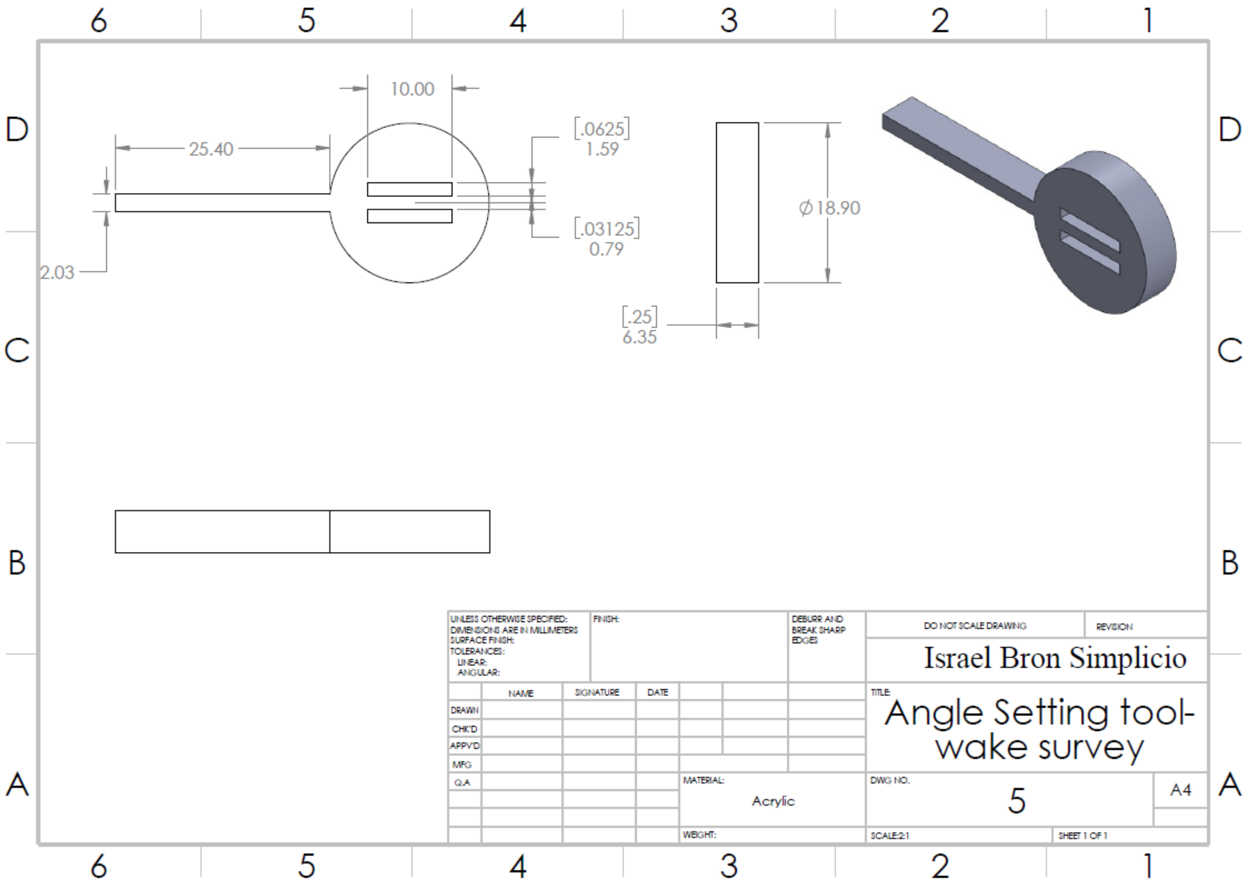

10.00
25.40
2.03
[.0625]
1.59
[.03125]
0.79
Ø18.90
[.25]
6.35
UNLESS OTHERWISE SPECIFIED:
DIMENSIONS ARE IN MILLIMETERS
SURFACE FINISH:
TOLERANCES:
LINEAR:
ANGULAR:
FINISH:
DEBURR AND BREAK SHARP EDGES
DO NOT SCALE DRAWING
REVISION
Israel Bron Simplicio
NAME
SIGNATURE
DATE
DRAWN
CHK'D
APPV'D
MFG
Q.A
TITLE:
Angle Setting tool-
wake survey
MATERIAL:
Acrylic
DWG NO.
5
A4
WEIGHT:
SCALE:2:1
SHEET 1 OF 1
6
5
4
3
2
1
D
C
B
A

µWT force balance:

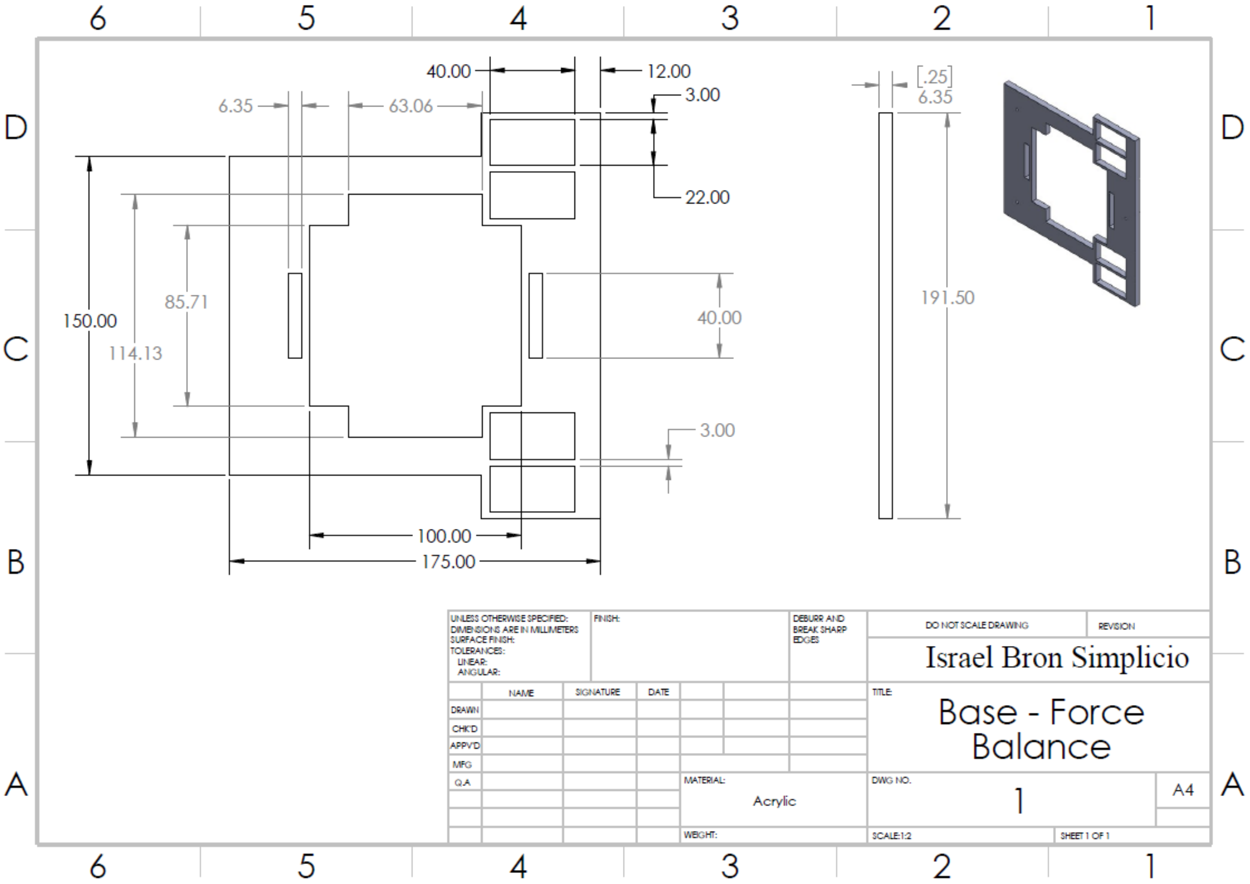

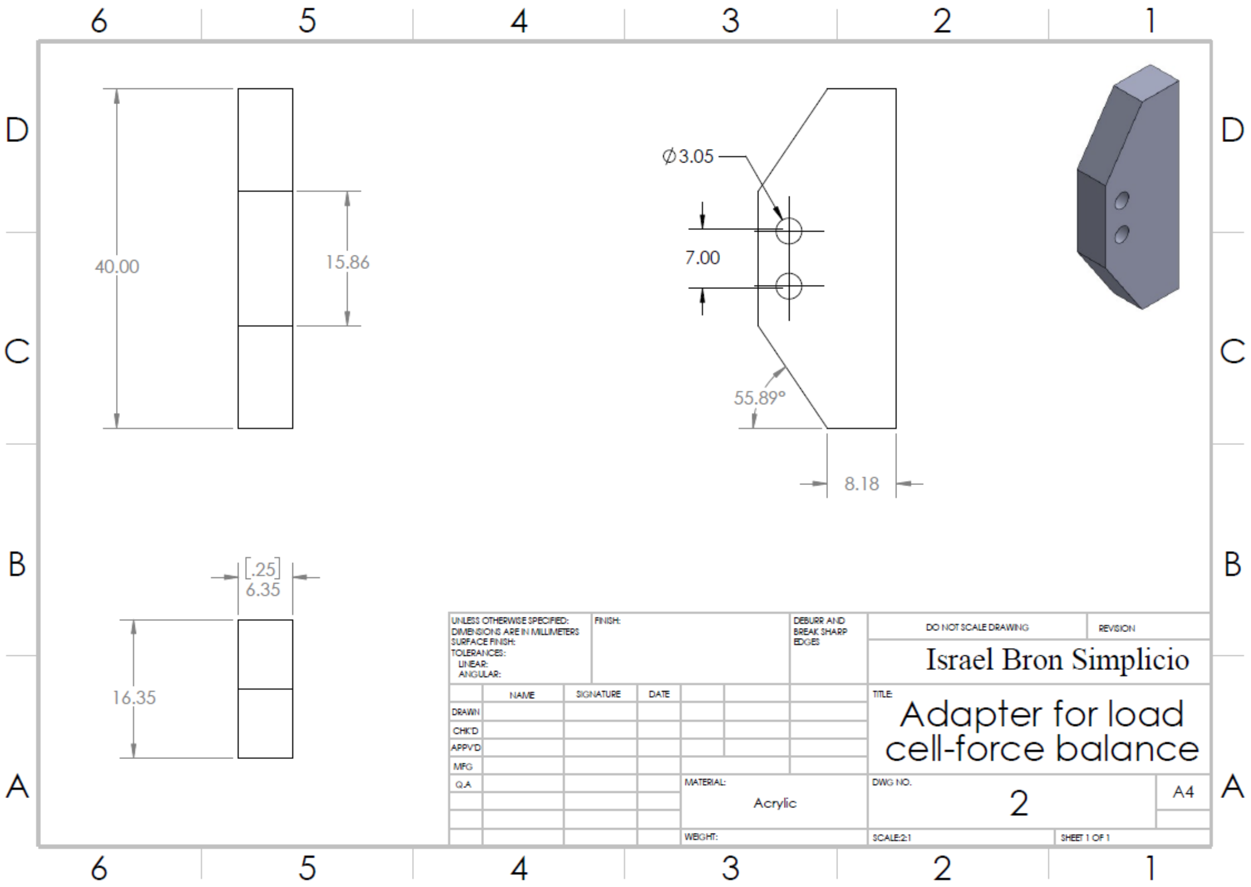

UNLESS OTHERWISE SPECIFIED:
DIMENSIONS ARE IN MILLIMETERS
SURFACE FINISH:
TOLERANCES:
LINEAR:
ANGULAR:

FINISH:

DEBURR AND
BREAK SHARP
EDGES

DO NOT SCALE DRAWING

REVISION

Israel Bron Simplicio

	NAME	SIGNATURE	DATE
DRAWN			
CHK'D			
APPV'D			
MFG			
Q.A			

TITLE:
Adapter for load
cell-force balance

MATERIAL:
Acrylic

WEIGHT:

DWG NO.
2

A4

SCALE:2:1

SHEET 1 OF 1

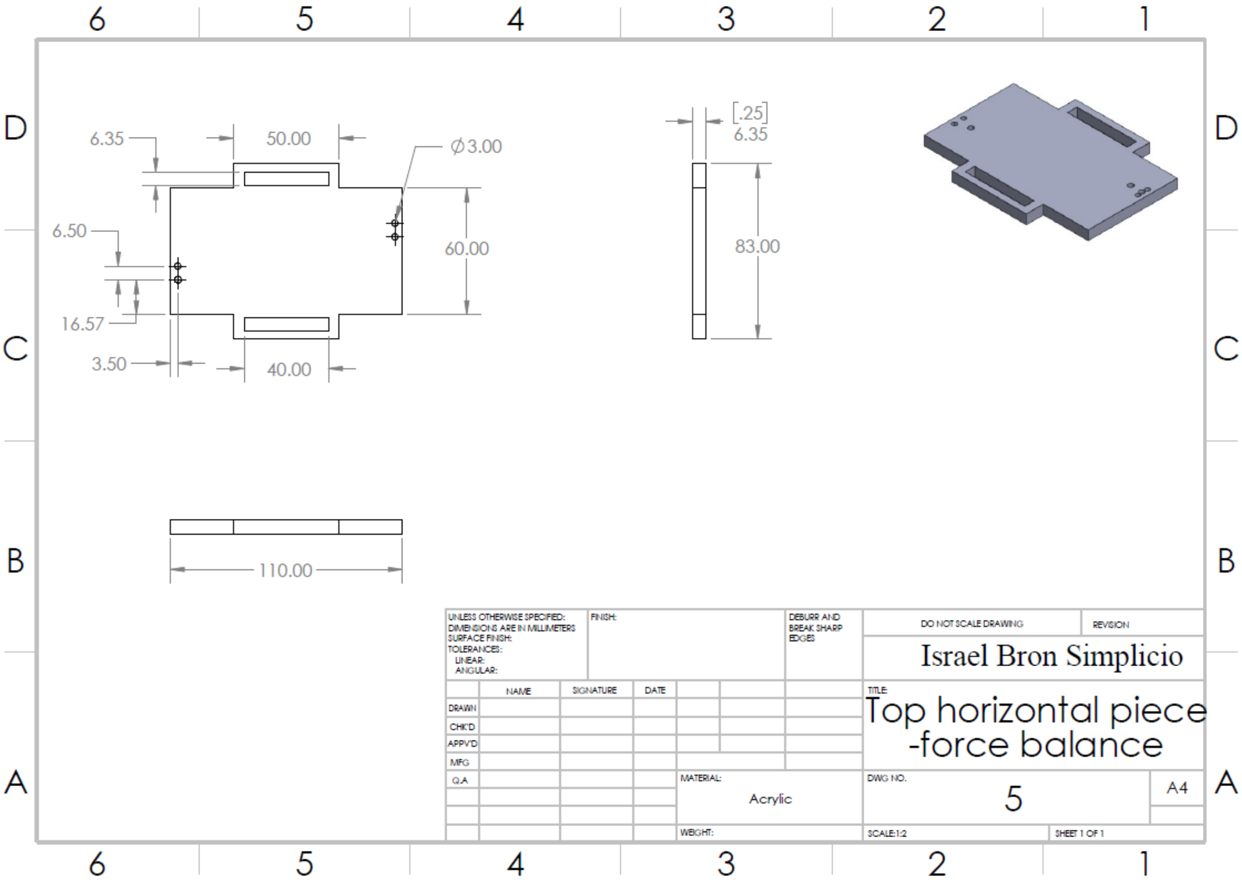

UNLESS OTHERWISE SPECIFIED:
DIMENSIONS ARE IN MILLIMETERS
SURFACE FINISH:
TOLERANCES:
LINEAR:
ANGULAR:

FINISH:

DEBURR AND BREAK SHARP EDGES

DO NOT SCALE DRAWING

REVISION

Israel Bron Simplicio

	NAME	SIGNATURE	DATE
DRAWN			
CHK'D			
APPV'D			
MFG			
Q.A			

TITLE: Top horizontal piece -force balance

MATERIAL: Acrylic

WEIGHT:

DWG NO. 5

A4

SCALE:1:2

SHEET 1 OF 1

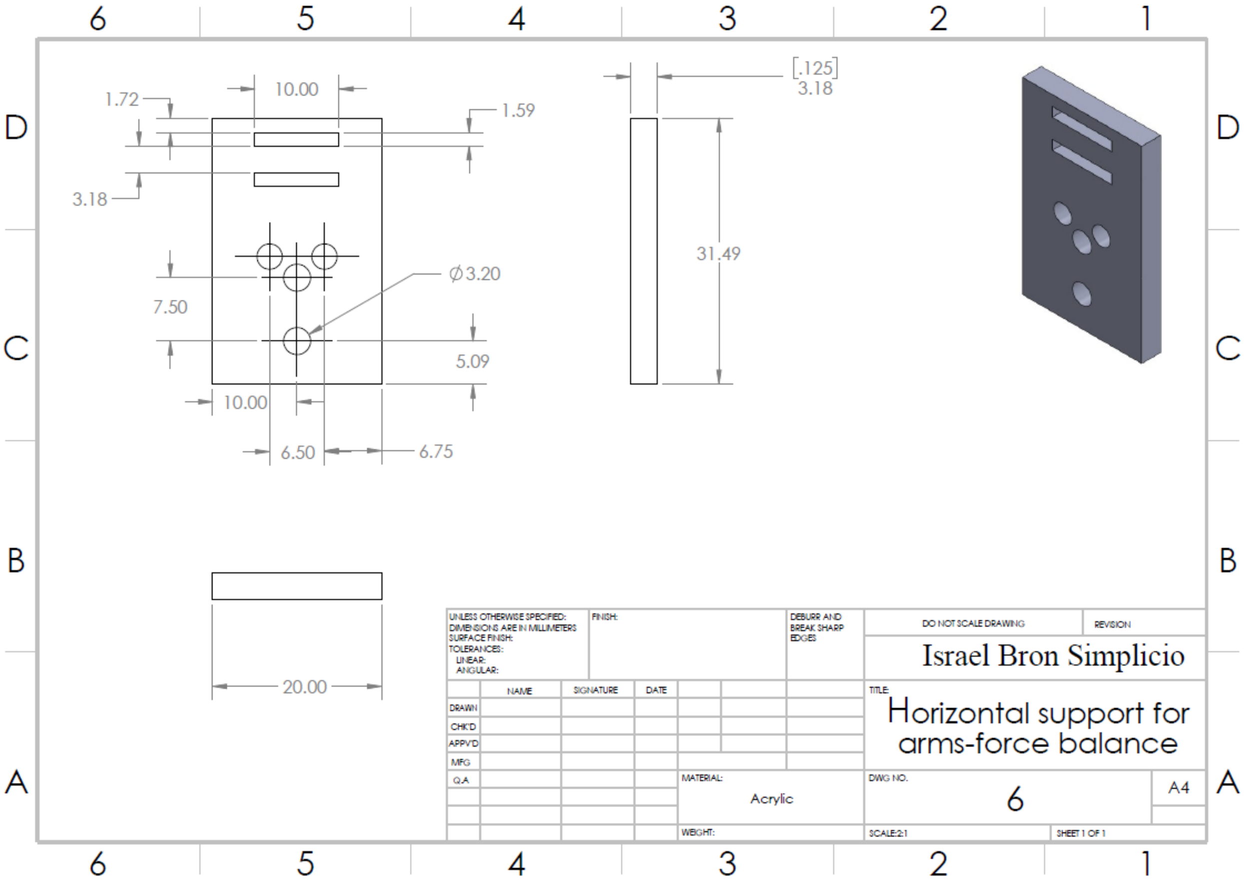
1.72
10.00
1.59
3.18
7.50
∅3.20
5.09
10.00
6.50
6.75
[.125]
3.18
31.49
20.00
UNLESS OTHERWISE SPECIFIED:
DIMENSIONS ARE IN MILLIMETERS
SURFACE FINISH:
TOLERANCES:
LINEAR:
ANGULAR:
FINISH:
DEBURR AND BREAK SHARP EDGES
DO NOT SCALE DRAWING
REVISION
Israel Bron Simplicio
NAME
SIGNATURE
DATE
DRAWN
CHK'D
APPV'D
MFG
Q.A
TITLE:
Horizontal support for arms-force balance
MATERIAL:
Acrylic
DWG NO.
6
A4
WEIGHT:
SCALE:2:1
SHEET 1 OF 1

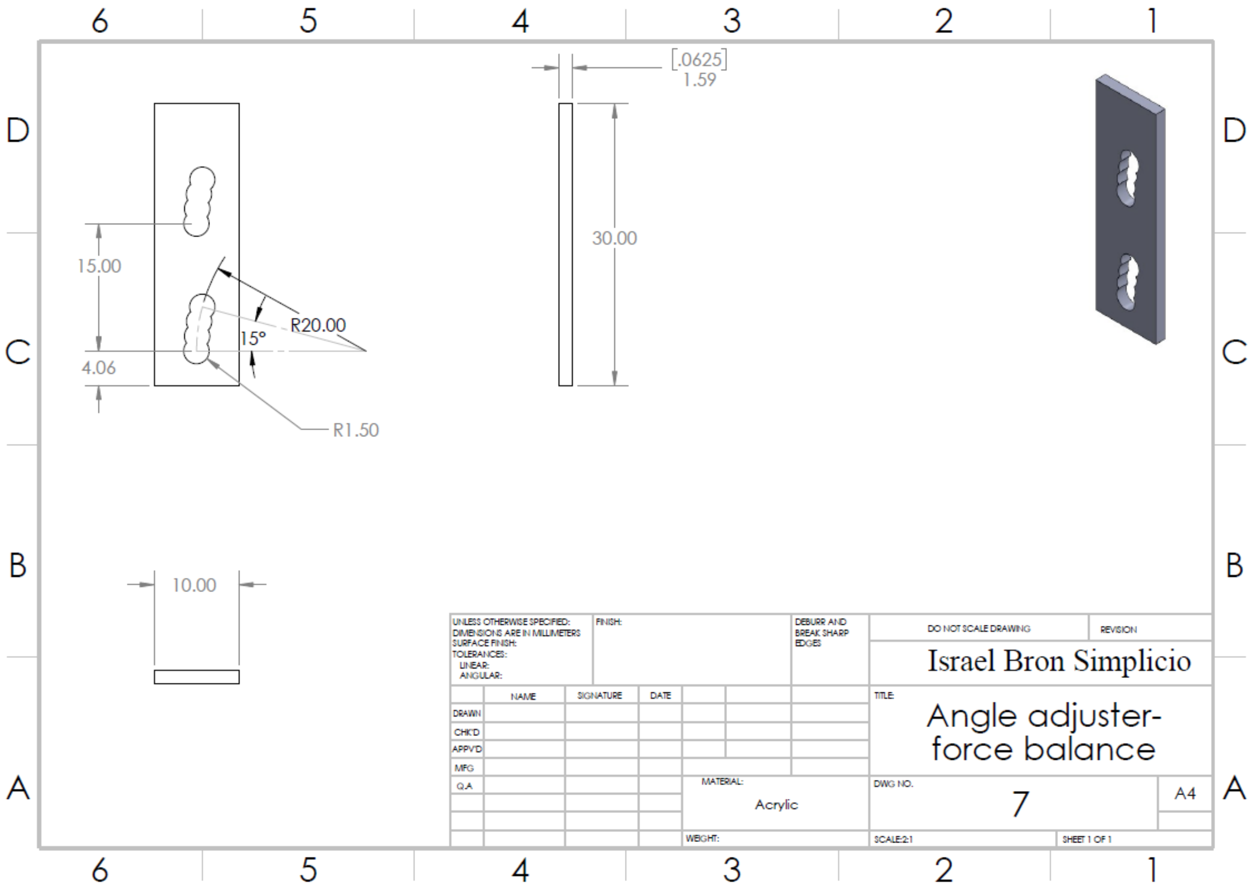
[.0625]
1.59
30.00
15.00
4.06
15°
R20.00
R1.50
10.00
UNLESS OTHERWISE SPECIFIED:
DIMENSIONS ARE IN MILLIMETERS
SURFACE FINISH:
TOLERANCES:
LINEAR:
ANGULAR:
FINISH:
DEBURR AND BREAK SHARP EDGES
DO NOT SCALE DRAWING
REVISION
Israel Bron Simplicio
NAME
SIGNATURE
DATE
DRAWN
CHK'D
APPV'D
MFG
Q.A
TITLE:
Angle adjuster-force balance
MATERIAL:
Acrylic
DWG NO.
7
A4
WEIGHT:
SCALE:2:1
SHEET 1 OF 1
6
5
4
3
2
1
D
C
B
A

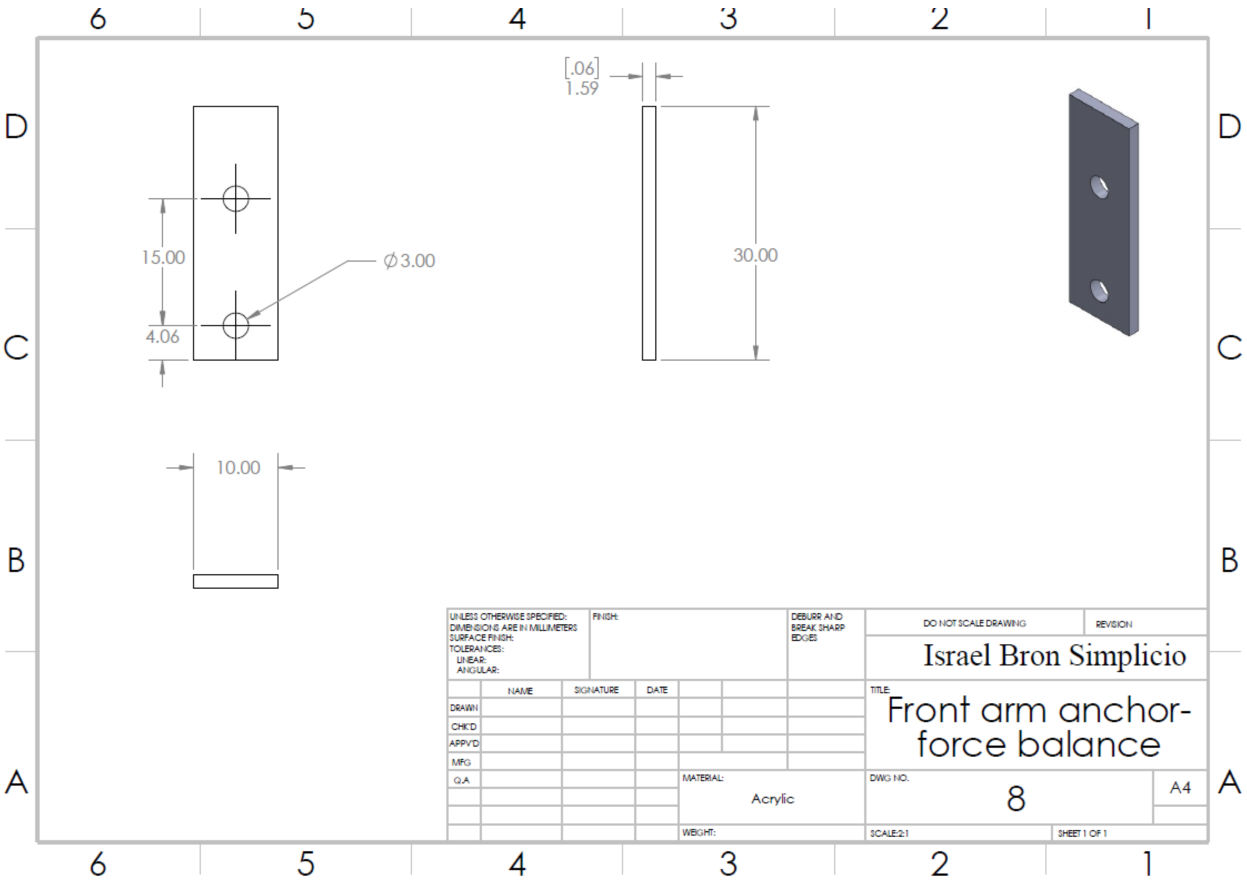

UNLESS OTHERWISE SPECIFIED:
DIMENSIONS ARE IN MILLIMETERS
SURFACE FINISH:
TOLERANCES:
LINEAR:
ANGULAR:

FINISH:

DEBURR AND BREAK SHARP EDGES

DO NOT SCALE DRAWING

REVISION

Israel Bron Simplicio

	NAME	SIGNATURE	DATE
DRAWN			
CHK'D			
APPV'D			
MFG			
Q.A			

TITLE: Front arm anchor-force balance

MATERIAL: Acrylic

DWG NO. 8

A4

WEIGHT:

SCALE:2:1

SHEET 1 OF 1

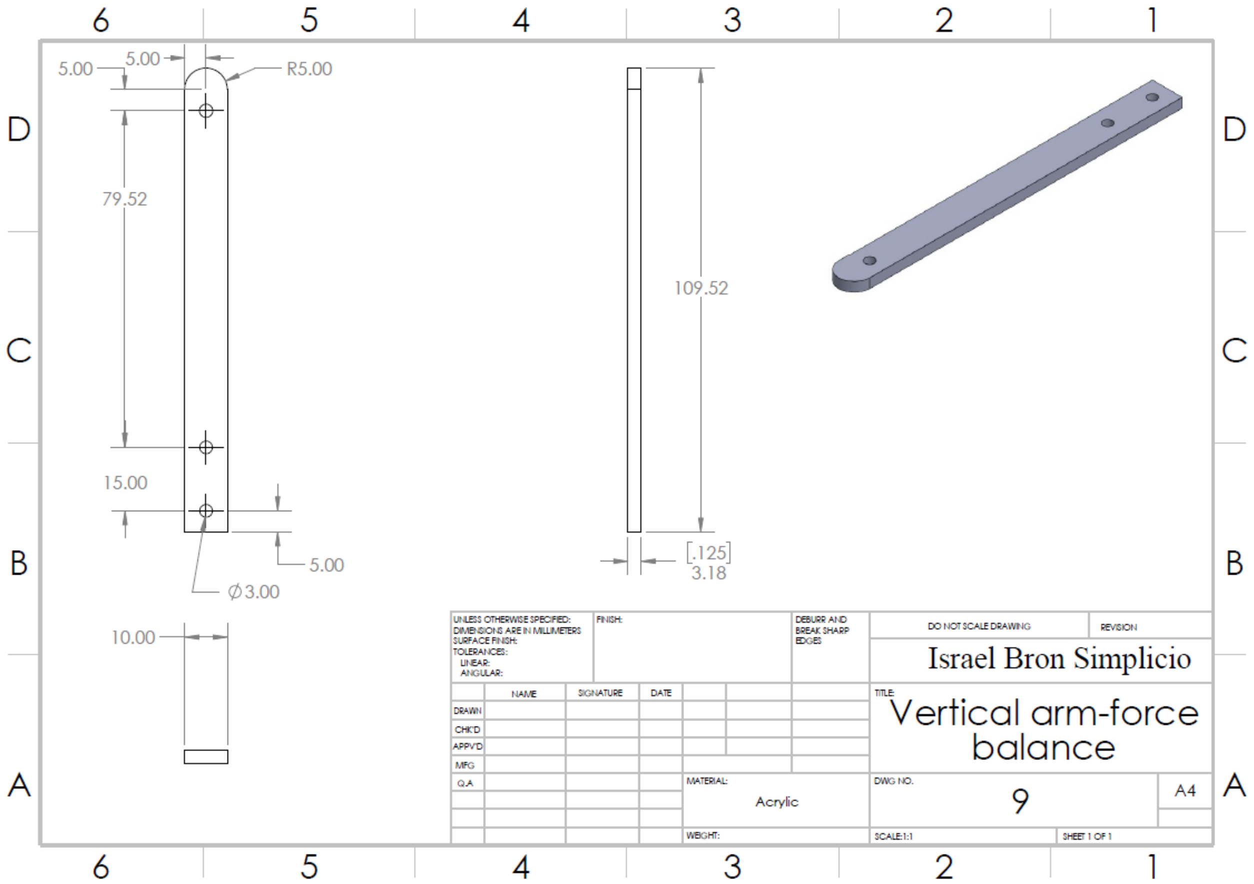

UNLESS OTHERWISE SPECIFIED:
DIMENSIONS ARE IN MILLIMETERS
SURFACE FINISH:
TOLERANCES:
LINEAR:
ANGULAR:

FINISH:

DEBURR AND BREAK SHARP EDGES

DO NOT SCALE DRAWING

REVISION

Israel Bron Simplicio

TITLE: Vertical arm-force balance

MATERIAL: Acrylic

DWG NO. 9

WEIGHT:

SCALE:1:1

SHEET 1 OF 1

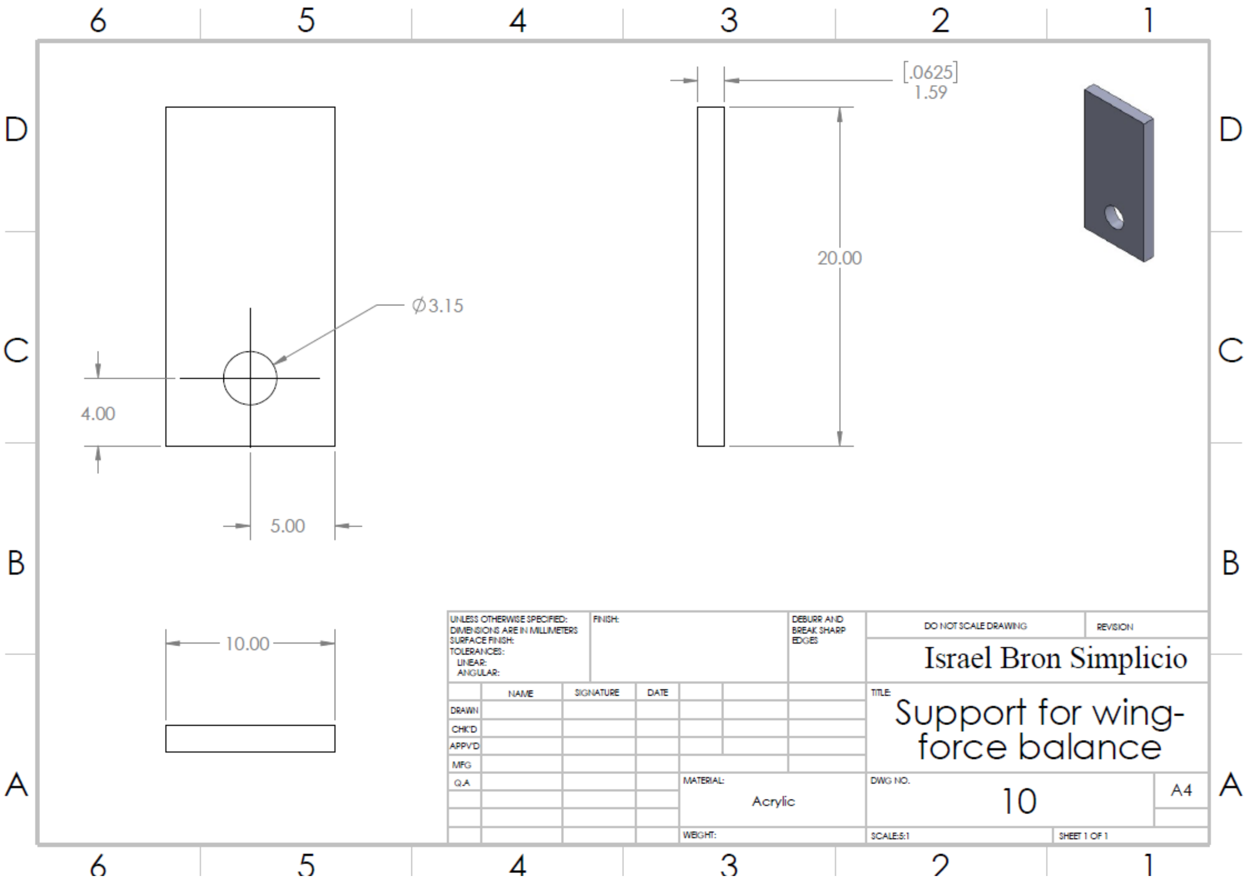
[.0625]
1.59
20.00
∅3.15
4.00
5.00
10.00
UNLESS OTHERWISE SPECIFIED:
DIMENSIONS ARE IN MILLIMETERS
SURFACE FINISH:
TOLERANCES:
LINEAR:
ANGULAR:
FINISH:
DEBURR AND BREAK SHARP EDGES
DO NOT SCALE DRAWING
REVISION
Israel Bron Simplicio
NAME
SIGNATURE
DATE
DRAWN
CHK'D
APPV'D
MFG
Q.A
TITLE:
Support for wing-force balance
MATERIAL:
Acrylic
DWG NO.
10
A4
WEIGHT:
SCALE:5:1
SHEET 1 OF 1

3’ x 3’ WT:

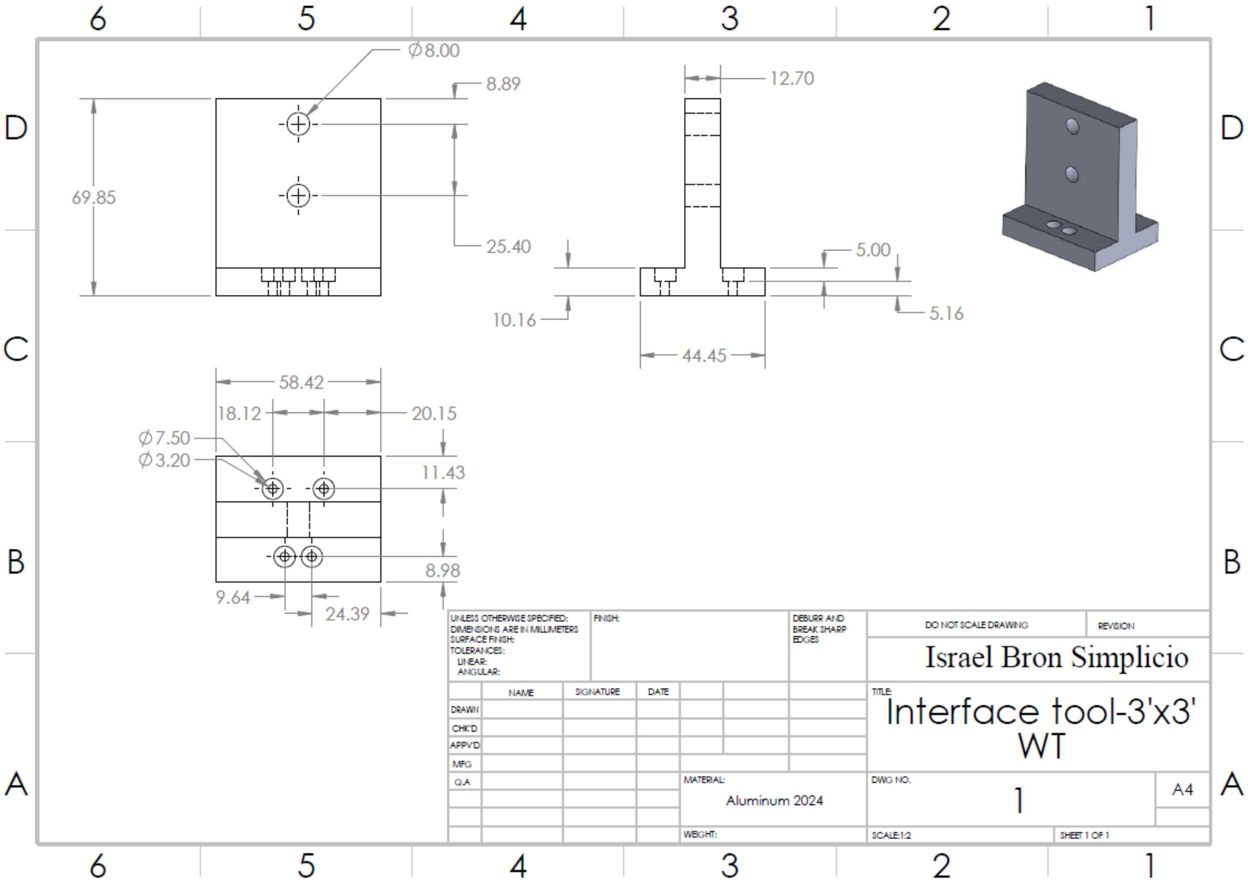
Ø8.00
8.89
12.70
69.85
25.40
5.00
10.16
5.16
44.45
58.42
18.12
20.15
Ø7.50
Ø3.20
11.43
8.98
9.64
24.39
UNLESS OTHERWISE SPECIFIED:
DIMENSIONS ARE IN MILLIMETERS
SURFACE FINISH:
TOLERANCES:
LINEAR:
ANGULAR:
FINISH:
DEBURR AND BREAK SHARP EDGES
DO NOT SCALE DRAWING
REVISION
Israel Bron Simplicio
NAME
SIGNATURE
DATE
DRAWN
CHK'D
APPV'D
MFG
Q.A
TITLE:
Interface tool-3'x3' WT
MATERIAL:
Aluminum 2024
DWG NO.
1
A4
WEIGHT:
SCALE:1:2
SHEET 1 OF 1
A
B
C
D
1
2
3
4
5
6

APPENDIX C: WAKE SURVEY ANALYSIS MATLAB POST-PROCESSING CODE

```
clc
clear all
close all

% Import
cd('C:\Users\isbro\Documents\LabVIEW Data\velocity_fields');
addpath('C:\Users\isbro\Downloads\drive-download-20201103T001100Z-001');
ordner = dir('meas*.lvm');
dateiliste = {ordner.name};
cal=importfile_cal('calib_001.lvm');
cal2=importfile_cal('calib_002.lvm');
cal_new =
[linspace(cal(1),cal2(1),length(dateiliste));linspace(cal(2),cal2(2),length(d
ateiliste))];
% Automatic scanning
for i = 1:length(dateiliste)
    p_temp = importfile_press_new(dateiliste{1,i});
    p_raw(i,1:2) = mean(rmoutliers(p_temp(500:end-1,:)));
    koord(i,1:2) = importfile_koord(dateiliste{1,i});
    i
end
%p_stat = p_raw(:,1)-cal(1);
%p_tot = p_raw(:,2)-cal(2);
%p_stat = p_raw(:,1)-cal_new(1,:)';
%p_tot = p_raw(:,2)-cal_new(2,:)';
p_tot = p_raw(:,1)-cal_new(1,:)';
p_stat = p_raw(:,2)-cal_new(2,:)';
%% q/qmax, q, and v_
q_list = -(p_tot-p_stat);
q_point = q_list;
q_max = max(q_list);
q_list = q_list/q_max;
v_points = sqrt(406.27*q_point);
v_points = real(v_points);

%q_list = q_list/q_max*30.01;
%q_list = q_list - min(q_list);
%minev_list = sqrt(2*(q_list*30.01)/1.225);
%v_list = sqrt(2*(q_list*248.84)/1.225);



%% Tecplot Export (q/qmax)

fid = fopen(['C:\Users\isbro\Documents\literature survey Masters\data for
research\flat plate\triangular 20 5\zero
angle\triangularmediumnarrow0.dat'],'wt');
fprintf(fid, 'VARIABLES = "x", "y", "q/q_max"\n');
fprintf(fid, ['ZONE T="export_new_calib"','\n']);
for i = 1:length(q_list)
    fprintf(fid, '%4.6f %4.6f %4.6f\n',[koord(i,1);koord(i,2);q_list(i)]);
```

```
end
fclose(fid);

%% Tecplot Export (velocity)

fid = fopen(['C:\Users\isbro\Documents\literature survey Masters\data for
research\flat plate\concave down 10 10\20 angle\concaved20.dat'],'wt');
fprintf(fid, 'VARIABLES = "x", "y", "velocity"\n');
fprintf(fid, ['ZONE T="export_new_calib"','\n']);
for i = 1:length(q_list)
    fprintf(fid, '%4.6f %4.6f %4.6f\n',[koord(i,1);koord(i,2);v_points(i)]);
end
fclose(fid);

%% Excel Export (q/q_max, and velocity)

t=1;
for i = 1:length(q_list)
    if koord(i,1) == koord(16,1)
        xldata(t,1) = koord(i,1);
        xldata(t,2) = koord(i,2);
        xldata(t,3) = q_list(i);
        xldata(t,4) = v_points(i);
        t=t+1;
    end
end
%% wake survey option 1
%
rho=1.225;
delta_y = (koord(31,2)-koord(30,2))/1000;
t=1;
x=1;

for b=4:24
    for i = 1:length(q_list)
        if koord(i,1) == koord(b,1)
            if koord (i,2) >= koord (152,2) && koord (i,2) <= koord (781,2)
                    U(t,x) = v_points(i);
                    t=t+1;
            end
        end
    end
    U_inf(x)=max(U(:,x));
    t=1;
    x=x+1;
end

[row,col] = size(U);

%areas at the moment f.p.: 4900; 10 20, 10 10 and 10 5: 4655; c.up. 4735.82;
% c.d.: 4574.28; 5 5: 4777.5; 20 5: 4410
chord = input('write the area of the wing in mm^2: ')/(98*1000);
drag = zeros(1,col);

for i=1:col
```

```
    for b = 1:row
        drag(i) = drag(i) + U(b,i)*(U_inf (i)-U(b,i))*delta_y;
        %cd(i) = cd(i) + U(b,i)*(6.5-U(b,i))*delta_y;
    end
    cd(i) = drag(i)*2/(chord*(U_inf(i))^2);
    %cd(i) = cd(i)*2/(chord*(6.5)^2);
end

Cd = mean(cd);
```

APPENDIX D: FORCE BALANCE ARDUINO CODE [45]

```
#include "HX711-multi.h"
#define CLK A0 // clock pin to the load cell
#define N 4 // # of channels
#define DOUT1 A1 // 1st load cell Lift 1
#define DOUT2 A2 // 2nd load cell Lift 2
#define DOUT3 A3 // 3rd load cell Drag 1
#define DOUT4 A4 // 4rd load cell Drag 2

#define TARE_TIMEOUT_SECONDS 4

// Inputs
double x01 = 0.015; // distance between the leading edge and the first load cell [m]
double v = 8.5; // speed of the wind [m/s]
double rho = 1.225; // density [kg/m^3]
double S = 0.0049; // wing surface [m^2] f.p.: 0.0049; 10 20, 10 10 and 10 5: 0.004655; c.up.
0.00473582; c.d.: 0.00457428; 5 5: 0.0047775; 20 5: 0.004410
double C = 0.05; // chord length [m]

//CALLIBRATION OF THE BALANCE
float measurements[N] = {310574.00/25.00, -301024.00/25.00, -237500.00/25.00,
216000.00/25.00}; // measured SCALES parameters

// MAIN CODE

// Init
byte DOUTS[N] = {DOUT1, DOUT2, DOUT3,DOUT4};
long int results[N];
double weights[N];
double go = 9.80662;
double lift;
```

```
double Lift;
double drag;
double Drag;
double Mle;
double F1;
double F2;
double F3;
double F4;
double x02 = 0.02;
double x12 = x01 + x02;
double xcp;
double Cl;
double Cd;
double Cm;

HX711MULTI scales(N, DOUTS, CLK);

void setup() {
Serial.begin(115200);
Serial.flush();
tare();
scales.set_scales(measurements);
}

void tare() {
bool tareSuccessful = false;
unsigned long tareStartTime = millis();
while (!tareSuccessful && millis() < (tareStartTime + TARE_TIMEOUT_SECONDS
* 1000)) {
tareSuccessful = scales.tare(20, 10000); //reject 'tare' if still ringing
}
```

```
}
void sendWeightData() {
scales.get_units(weights);
for (int i = 0; i < scales.get_count(); ++i) {
Serial.print(-weights[i]);
Serial.print((i != scales.get_count() - 1) ? "\t" : "\n");
}
delay(1000);
}
void loop() {
Serial.println("WEIGHT DATA BELOW");
sendWeightData();
Serial.println();
//calculate forces in N
F1 = weights[0]*go/1000.0; //[N]
F2 = weights[1]*go/1000.0; //[N]
lift = F1 + F2;
F3 = (weights[2])*go/1000.0; //[N] new 4 load cells
F4 = (weights[3])*go/1000.0; //[N] new 4 load cells
drag = F3 + F4; //[N] new 4 load cells
Mle = x01 * F1 + x02 *F2; // [N*m]
xcp = (x02 * F2 + x01 * F2) / (F1 + F2)*1000.0;

//aerodynamic coefficients
Cl = (lift*2)/(rho*v*v*S);
Cd = (drag*2)/(rho*v*v*S);
Cm = (Mle*2)/(rho*v*v*S*C);
Drag = drag*1000; //mN
Lift = lift*1000; //mN
Serial.print("lift = ");
Serial.print(Lift);
```

```
Serial.println(" [mN]");
Serial.print("drag = ");
Serial.print(Drag);
Serial.println(" [mN]");
Serial.print("momentum at the leading edge = ");
Serial.print(Mle);
Serial.println(" [N*m]");
Serial.print("position of the centre of pressure: ");
Serial.print(xcp);
Serial.println(" [mm]");
Serial.println();
Serial.println("Aerodynamic coefficients");
Serial.print("Cl = ");
Serial.println(Cl);
Serial.print("Cd = ");
Serial.println(Cd);
Serial.print("Cm = ");
Serial.println(Cm);
Serial.println();
// On serial data (any data), re-tare
if (Serial.available() > 0) {
while (Serial.available()) {
Serial.read();
}
tare();
}
}
```

APPENDIX E: DATA TABLES

µWT

Table D.1 C_L.

Wing ID	W1		W2		W3		W4		W5		W6		W7		W8	
	AVG	STD DEV	AVG	STD DEV	AVG	STD DEV	AVG	STD DEV	AVG	STD DEV	AVG	STD DEV	AVG	STD DEV	AVG	STD DEV
α	-----	-----	-----	-----	-----	-----	-----	-----	-----	-----	-----	-----	-----	-----	-----	-----
0˚	0.24	0.011	0.11	0.005	0.21	0.005	0.20	0.005	0.26	0.005	0.21	0.003	0.14	0.005	0.20	0.005
5˚	0.67	0.018	0.55	0.009	0.77	0.014	0.62	0.009	0.78	0.014	0.70	0.012	0.66	0.017	0.69	0.006
10˚	0.88	0.019	0.90	0.015	0.90	0.019	0.84	0.016	0.91	0.025	0.91	0.022	0.90	0.017	0.76	0.021
15˚	0.92	0.023	0.94	0.018	0.88	0.014	0.83	0.021	0.92	0.026	0.92	0.028	0.91	0.021	0.91	0.032

Table D.2 C_D.

Wing ID	W1		W2		W3		W4		W5		W6		W7		W8	
	AVG	STD DEV	AVG	STD DEV	AVG	STD DEV	AVG	STD DEV	AVG	STD DEV	AVG	STD DEV	AVG	STD DEV	AVG	STD DEV
α	-----	-----	-----	-----	-----	-----	-----	-----	-----	-----	-----	-----	-----	-----	-----	-----
0˚	0.17	0.006	0.16	0.004	0.15	0.003	0.16	0.004	0.15	0.004	0.13	0.006	0.15	0.003	0.15	0.003
5˚	0.26	0.011	0.22	0.011	0.31	0.010	0.26	0.007	0.28	0.006	0.29	0.008	0.26	0.008	0.25	0.008
10˚	0.39	0.012	0.42	0.013	0.45	0.014	0.44	0.013	0.42	0.015	0.45	0.013	0.40	0.012	0.33	0.014
15˚	0.47	0.018	0.52	0.009	0.47	0.009	0.50	0.019	0.43	0.014	0.48	0.014	0.50	0.018	0.42	0.013

Table D.3 C_M.

Wing ID	W1		W2		W3		W4		W5		W6		W7		W8	
	AVG	STD DEV	AVG	STD DEV	AVG	STD DEV	AVG	STD DEV	AVG	STD DEV	AVG	STD DEV	AVG	STD DEV	AVG	STD DEV
α	-----	-----	-----	-----	-----	-----	-----	-----	-----	-----	-----	-----	-----	-----	-----	-----
0˚	0.07	0.007	0.04	0.004	0.06	0.005	0.06	0.007	0.09	0.004	0.06	0.005	0.04	0.003	0.04	0.003
5˚	0.22	0.015	0.17	0.020	0.25	0.016	0.19	0.005	0.25	0.011	0.22	0.005	0.22	0.008	0.23	0.007
10˚	0.28	0.018	0.29	0.013	0.28	0.017	0.26	0.014	0.29	0.011	0.29	0.014	0.3	0.011	0.25	0.011
15˚	0.3	0.02	0.27	0.015	0.27	0.01	0.26	0.013	0.26	0.017	0.29	0.012	0.28	0.01	0.3	0.009

3’ X 3’ WT

Table D.4 W9, Re = 100,000

Coefficient	**C_L**		**C_D**		**C_M**	
	AVG	STD DEV	AVG	STD DEV	AVG	STD DEV
α	-----	-----	-----	-----	-----	-----
0°	-0.01	0.026	0.054	0.02393	-0.022	0.009
2.5°	0.26	0.026	0.080	0.02035	-0.019	0.009
5°	0.53	0.024	0.115	0.03226	-0.021	0.009
7.5°	0.81	0.043	0.190	0.02256	-0.049	0.015
10°	0.97	0.100	0.274	0.03243	-0.108	0.048
12.5°	1.00	0.073	0.335	0.03152	-0.136	0.027
15°	1.00	0.044	0.388	0.02948	-0.155	0.016
17.5°	1.03	0.051	0.445	0.03354	-0.166	0.020
20°	1.08	0.060	0.511	0.03378	-0.177	0.019
22.5°	1.09	0.043	0.568	0.03005	-0.181	0.015
25°	1.09	0.066	0.619	0.04229	-0.185	0.021
27.5°	1.14	0.048	0.702	0.03454	-0.202	0.015
30°	1.16	0.042	0.772	0.03321	-0.214	0.015

Table D.5 W9, Re = 150,000

Coefficient	**C_L**		**C_D**		**C_M**	
	AVG	STD DEV	AVG	STD DEV	AVG	STD DEV
α	-----	-----	-----	-----	-----	-----
0°	-0.023	0.014	0.041	0.008	-0.007	0.010
2.5°	0.211	0.017	0.055	0.009	-0.002	0.029
5°	0.407	0.054	0.076	0.011	0.002	0.012
7.5°	0.631	0.039	0.134	0.012	-0.009	0.019
10°	0.759	0.042	0.196	0.014	-0.052	0.019
12.5°	0.816	0.039	0.250	0.015	-0.079	0.036
15°	0.801	0.073	0.291	0.024	-0.089	0.024
17.5°	0.832	0.048	0.340	0.019	-0.102	0.021
20°	0.870	0.068	0.394	0.029	-0.110	0.023
22.5°	0.906	0.047	0.450	0.023	-0.118	0.043
25°	0.938	0.025	0.510	0.015	-0.125	0.014
27.5°	0.944	0.025	0.562	0.017	-0.133	0.011
30°	0.950	0.041	0.620	0.027	-0.142	0.021

Table D.6 W9, Re = 200,000

Coefficient	**C_L**		**C_D**		**C_M**	
	AVG	STD DEV	AVG	STD DEV	AVG	STD DEV
α	-----	-----	-----	-----	-----	-----
0°	-0.013	0.018	0.047	0.011	-0.005	0.008
2.5°	0.201	0.016	0.052	0.006	-0.004	0.005
5°	0.398	0.045	0.076	0.007	-0.006	0.004
7.5°	0.620	0.024	0.132	0.008	-0.033	0.008
10°	0.751	0.035	0.192	0.011	-0.084	0.021
12.5°	0.795	0.048	0.241	0.014	-0.099	0.015
15°	0.775	0.064	0.276	0.020	-0.112	0.021
17.5°	0.792	0.047	0.320	0.019	-0.119	0.091
20°	0.855	0.073	0.381	0.033	-0.131	0.135
22.5°	0.873	0.080	0.429	0.038	-0.136	0.088
25°	0.864	0.050	0.467	0.026	-0.137	0.042
27.5°	0.879	0.030	0.522	0.018	-0.146	0.013
30°	0.899	0.031	0.583	0.021	-0.158	0.015

Table D.7 W10, Re = 100,000

Coefficient	**C_L**		**C_D**		**C_M**	
	AVG	STD DEV	AVG	STD DEV	AVG	STD DEV
α	-----	-----	-----	-----	-----	-----
0°	-0.022	0.033	0.079	0.020	-0.007	0.015
2.5°	0.183	0.028	0.099	0.026	0.002	0.023
5°	0.434	0.030	0.133	0.020	0.006	0.024
7.5°	0.719	0.050	0.198	0.022	-0.020	0.022
10°	0.876	0.075	0.272	0.029	-0.071	0.042
12.5°	0.900	0.067	0.327	0.029	-0.093	0.038
15°	0.912	0.043	0.378	0.027	-0.107	0.037
17.5°	0.939	0.049	0.426	0.026	-0.119	0.019
20°	1.003	0.074	0.493	0.036	-0.134	0.039
22.5°	1.032	0.037	0.550	0.026	-0.142	0.015
25°	1.035	0.057	0.598	0.035	-0.143	0.019
27.5°	1.060	0.041	0.661	0.030	-0.153	0.014
30°	1.052	0.048	0.712	0.034	-0.160	0.015

Table D.8 W10, Re = 150,000

Coefficient	**C_L**		**C_D**		**C_M**	
	AVG	STD DEV	AVG	STD DEV	AVG	STD DEV
α	-----	-----	-----	-----	-----	-----
0°	-0.057	0.018	0.065	0.009	0.000	0.011
2.5°	0.131	0.017	0.072	0.009	0.003	0.007
5°	0.376	0.037	0.099	0.009	0.004	0.007
7.5°	0.618	0.037	0.155	0.013	-0.024	0.018
10°	0.764	0.057	0.218	0.016	-0.072	0.023
12.5°	0.800	0.037	0.267	0.015	-0.093	0.020
15°	0.806	0.047	0.308	0.018	-0.105	0.021
17.5°	0.831	0.054	0.356	0.022	-0.116	0.025
20°	0.887	0.060	0.414	0.026	-0.129	0.020
22.5°	0.894	0.043	0.459	0.021	-0.132	0.016
25°	0.928	0.036	0.518	0.020	-0.143	0.022
27.5°	0.928	0.034	0.564	0.021	-0.148	0.018
30°	0.947	0.030	0.627	0.021	-0.160	0.013

Table D.9 W10, Re = 200,000

Coefficient	**C_L**		**C_D**		**C_M**	
	AVG	STD DEV	AVG	STD DEV	AVG	STD DEV
α	-----	-----	-----	-----	-----	-----
0°	-0.054	0.016	0.057	0.005	0.001	0.007
2.5°	0.143	0.019	0.064	0.006	0.003	0.009
5°	0.341	0.079	0.087	0.007	0.004	0.009
7.5°	0.588	0.023	0.141	0.008	-0.027	0.009
10°	0.710	0.040	0.197	0.011	-0.069	0.015
12.5°	0.732	0.051	0.241	0.014	-0.083	0.026
15°	0.754	0.036	0.283	0.014	-0.098	0.028
17.5°	0.775	0.028	0.325	0.012	-0.108	0.019
20°	0.816	0.054	0.376	0.023	-0.119	0.022
22.5°	0.839	0.063	0.423	0.030	-0.122	0.028
25°	0.852	0.035	0.470	0.019	-0.130	0.030
27.5°	0.858	0.023	0.517	0.015	-0.135	0.026
30°	0.884	0.039	0.580	0.025	-0.148	0.021

Table D.10 W11, Re = 100,000

Coefficient	**C_L**		**C_D**		**C_M**	
	AVG	STD DEV	AVG	STD DEV	AVG	STD DEV
α	-----	-----	-----	-----	-----	-----
0°	0.052	0.028	0.047	0.019	-0.028	0.011
2.5°	0.334	0.029	0.072	0.022	-0.024	0.021
5°	0.580	0.025	0.110	0.029	-0.023	0.031
7.5°	0.842	0.035	0.179	0.032	-0.049	0.019
10°	0.968	0.091	0.258	0.027	-0.098	0.047
12.5°	1.046	0.058	0.329	0.027	-0.128	0.027
15°	1.049	0.055	0.380	0.034	-0.143	0.019
17.5°	1.080	0.051	0.442	0.029	-0.156	0.027
20°	1.146	0.048	0.519	0.028	-0.170	0.019
22.5°	1.152	0.077	0.574	0.039	-0.173	0.022
25°	1.192	0.054	0.649	0.033	-0.185	0.028
27.5°	1.191	0.038	0.710	0.029	-0.192	0.016
30°	1.180	0.034	0.771	0.028	-0.199	0.024

Table D.11 W11, Re = 150,000

Coefficient	**C_L**		**C_D**		**C_M**	
	AVG	STD DEV	AVG	STD DEV	AVG	STD DEV
α	-----	-----	-----	-----	-----	-----
0°	0.006	0.014	0.050	0.009	-0.006	0.009
2.5°	0.218	0.019	0.061	0.008	-0.005	0.010
5°	0.422	0.058	0.089	0.009	-0.002	0.012
7.5°	0.663	0.029	0.147	0.010	-0.027	0.014
10°	0.779	0.047	0.209	0.015	-0.069	0.024
12.5°	0.846	0.064	0.266	0.019	-0.096	0.028
15°	0.827	0.036	0.305	0.015	-0.103	0.057
17.5°	0.875	0.045	0.359	0.019	-0.116	0.021
20°	0.915	0.036	0.415	0.017	-0.126	0.018
22.5°	0.927	0.054	0.463	0.026	-0.132	0.023
25°	0.964	0.054	0.526	0.029	-0.142	0.029
27.5°	0.963	0.036	0.576	0.023	-0.147	0.014
30°	0.973	0.022	0.636	0.016	-0.157	0.013

Table D.12 W11, Re = 200,000

Coefficient	**C_L**		**C_D**		**C_M**	
	AVG	STD DEV	AVG	STD DEV	AVG	STD DEV
α	-----	-----	-----	-----	-----	-----
0°	-0.008	0.014	0.045	0.006	-0.005	0.014
2.5°	0.195	0.018	0.056	0.006	-0.004	0.013
5°	0.399	0.082	0.083	0.007	-0.001	0.014
7.5°	0.626	0.021	0.138	0.008	-0.030	0.008
10°	0.722	0.035	0.193	0.011	-0.065	0.019
12.5°	0.771	0.052	0.241	0.015	-0.084	0.026
15°	0.792	0.077	0.285	0.025	-0.097	0.036
17.5°	0.811	0.059	0.331	0.022	-0.106	0.042
20°	0.849	0.043	0.382	0.018	-0.114	0.020
22.5°	0.891	0.097	0.440	0.044	-0.127	0.047
25°	0.903	0.042	0.489	0.024	-0.132	0.046
27.5°	0.897	0.031	0.534	0.019	-0.137	0.045
30°	0.914	0.025	0.595	0.017	-0.148	0.010

Table D.13 W12, Re = 100,000

Coefficient	**C_L**		**C_D**		**C_M**	
	AVG	STD DEV	AVG	STD DEV	AVG	STD DEV
α	-----	-----	-----	-----	-----	-----
0°	-0.019	0.030	0.075	0.027	-0.009	0.012
2.5°	0.226	0.034	0.087	0.019	-0.004	0.016
5°	0.477	0.028	0.118	0.022	0.001	0.014
7.5°	0.774	0.042	0.183	0.021	-0.025	0.024
10°	0.926	0.053	0.255	0.022	-0.073	0.052
12.5°	0.969	0.048	0.319	0.025	-0.101	0.030
15°	0.985	0.075	0.371	0.031	-0.116	0.030
17.5°	1.023	0.048	0.428	0.024	-0.130	0.025
20°	1.068	0.054	0.494	0.030	-0.140	0.034
22.5°	1.097	0.067	0.556	0.035	-0.146	0.021
25°	1.132	0.047	0.624	0.030	-0.155	0.022
27.5°	1.125	0.039	0.678	0.029	-0.160	0.021
30°	1.135	0.030	0.746	0.025	-0.170	0.014

Table D.14 W12, Re = 150,000

Coefficient	**C_L**		**C_D**		**C_M**	
	AVG	STD DEV	AVG	STD DEV	AVG	STD DEV
α	-----	-----	-----	-----	-----	-----
0°	-0.020	0.018	0.060	0.008	-0.004	0.016
2.5°	0.190	0.023	0.069	0.009	0.001	0.010
5°	0.419	0.044	0.097	0.008	0.004	0.012
7.5°	0.668	0.028	0.154	0.010	-0.023	0.013
10°	0.767	0.074	0.213	0.019	-0.060	0.021
12.5°	0.815	0.091	0.264	0.025	-0.079	0.025
15°	0.837	0.066	0.308	0.022	-0.091	0.021
17.5°	0.868	0.051	0.359	0.020	-0.107	0.023
20°	0.908	0.040	0.415	0.019	-0.117	0.023
22.5°	0.956	0.073	0.478	0.034	-0.127	0.024
25°	0.954	0.070	0.524	0.037	-0.130	0.025
27.5°	0.958	0.031	0.575	0.020	-0.135	0.024
30°	0.958	0.038	0.628	0.026	-0.142	0.013

Table D.15 W12, Re = 200,000

Coefficient	**C_L**		**C_D**		**C_M**	
	AVG	STD DEV	AVG	STD DEV	AVG	STD DEV
α	-----	-----	-----	-----	-----	-----
0°	-0.045	0.014	0.054	0.005	-0.002	0.010
2.5°	0.162	0.019	0.062	0.006	0.004	0.011
5°	0.380	0.064	0.087	0.007	0.007	0.007
7.5°	0.611	0.034	0.141	0.009	-0.023	0.016
10°	0.721	0.042	0.194	0.012	-0.060	0.026
12.5°	0.752	0.054	0.238	0.017	-0.072	0.034
15°	0.767	0.052	0.282	0.018	-0.087	0.028
17.5°	0.807	0.031	0.332	0.013	-0.099	0.036
20°	0.844	0.090	0.385	0.037	-0.109	0.025
22.5°	0.861	0.061	0.429	0.029	-0.113	0.022
25°	0.878	0.049	0.480	0.026	-0.119	0.026
27.5°	0.880	0.035	0.526	0.020	-0.122	0.043
30°	0.889	0.022	0.580	0.015	-0.132	0.019

Table D.16 W13, Re = 100,000

Coefficient	**C_L**		**C_D**		**C_M**	
	AVG	STD DEV	AVG	STD DEV	AVG	STD DEV
α	-----	-----	-----	-----	-----	-----
0°	0.025	0.027	0.039	0.024	-0.018	0.033
2.5°	0.267	0.028	0.066	0.018	-0.011	0.012
5°	0.514	0.032	0.097	0.021	-0.007	0.018
7.5°	0.748	0.039	0.162	0.021	-0.013	0.020
10°	0.933	0.043	0.244	0.024	-0.070	0.040
12.5°	0.974	0.049	0.307	0.024	-0.100	0.054
15°	0.959	0.056	0.354	0.027	-0.111	0.019
17.5°	1.012	0.059	0.416	0.030	-0.129	0.031
20°	1.059	0.088	0.484	0.041	-0.141	0.025
22.5°	1.102	0.060	0.552	0.033	-0.149	0.019
25°	1.108	0.049	0.607	0.031	-0.153	0.026
27.5°	1.116	0.038	0.668	0.027	-0.160	0.016
30°	1.118	0.031	0.731	0.025	-0.170	0.017

Table D.17 W13, Re = 150,000

Coefficient	**C_L**		**C_D**		**C_M**	
	AVG	STD DEV	AVG	STD DEV	AVG	STD DEV
α	-----	-----	-----	-----	-----	-----
0°	-0.023	0.014	0.041	0.008	-0.007	0.010
2.5°	0.211	0.017	0.055	0.009	-0.002	0.029
5°	0.407	0.054	0.076	0.011	0.002	0.012
7.5°	0.631	0.039	0.134	0.012	-0.009	0.019
10°	0.759	0.042	0.196	0.014	-0.052	0.019
12.5°	0.816	0.039	0.250	0.015	-0.079	0.036
15°	0.801	0.073	0.291	0.024	-0.089	0.024
17.5°	0.832	0.048	0.340	0.019	-0.102	0.021
20°	0.870	0.068	0.394	0.029	-0.110	0.023
22.5°	0.906	0.047	0.450	0.023	-0.118	0.043
25°	0.938	0.025	0.510	0.015	-0.125	0.014
27.5°	0.944	0.025	0.562	0.017	-0.133	0.011
30°	0.950	0.041	0.620	0.027	-0.142	0.021

Table D.18 W13, Re = 200,000

Coefficient	**C_L**		**C_D**		**C_M**	
	AVG	STD DEV	AVG	STD DEV	AVG	STD DEV
α	-----	-----	-----	-----	-----	-----
0°	-0.028	0.016	0.034	0.005	-0.001	0.008
2.5°	0.174	0.017	0.046	0.006	0.003	0.013
5°	0.366	0.044	0.066	0.007	0.006	0.006
7.5°	0.577	0.029	0.121	0.009	-0.006	0.013
10°	0.704	0.062	0.181	0.014	-0.049	0.016
12.5°	0.748	0.046	0.228	0.014	-0.072	0.036
15°	0.747	0.065	0.270	0.021	-0.081	0.091
17.5°	0.779	0.040	0.315	0.018	-0.091	0.144
20°	0.840	0.047	0.374	0.023	-0.104	0.158
22.5°	0.836	0.038	0.412	0.019	-0.106	0.035
25°	0.898	0.048	0.483	0.033	-0.118	0.219
27.5°	0.876	0.036	0.518	0.024	-0.119	0.121
30°	0.877	0.044	0.568	0.028	-0.128	0.036

APPENDIX F: AUXILIARY TABLES

μWT

Table C.1 %ΔC_L.

Wing ID	**W2**	**W3**	**W4**	**W5**	**W6**	**W7**	**W8**
α	-----	-----	-----	-----	-----	-----	-----
5˚	-17.8%	14.6%	-7.76%	16.4%	4.32%	-1.04%	3.13%
10˚	1.93%	1.93%	-4.54%	3.06%	3.29%	2.27%	-13.4%
15˚	2.07%	-3.93%	-9.49%	0%	0%	-0.98%	-1.20%

Table C.2 %ΔC_D.

Wing ID	**W2**	**W3**	**W4**	**W5**	**W6**	**W7**	**W8**
α	-----	-----	-----	-----	-----	-----	-----
5˚	-16.5%	18.8%	-1.15%	6.92%	10.8%	0%	3.85%
10˚	6.92%	15.4%	12.6%	6.67%	14.4%	2.56%	-15.1%
15˚	10.8%	-0.42%	6.16%	-7.64%	1.70%	6.79%	-11.0%

Table C.3 %ΔC_L/C_D.

Wing ID	**W2**	**W3**	**W4**	**W5**	**W6**	**W7**	**W8**
α	-----	-----	-----	-----	-----	-----	-----
5˚	-1.38%	-3.61%	-6.78%	8.75%	-5.93%	-1.16%	7.19%
10˚	-4.65%	-11.6%	-15.2%	-3.36%	-9.71%	-0.31%	2.04%
15˚	-7.99%	-3.60%	-14.8%	8.16%	-1.79%	-7.35%	10.9%

Table C.4. %ΔC_M.

Wing ID	**W2**	**W3**	**W4**	**W5**	**W6**	**W7**	**W8**
α	-----	-----	-----	-----	-----	-----	-----
5˚	-22.73%	13.64%	-13.64%	13.64%	0.00%	0.00%	4.55%
10˚	3.57%	0.00%	-7.14%	3.57%	3.57%	7.14%	-10.71%
15˚	-10.00%	-10.00%	-13.33%	-13.33%	-3.33%	-6.67%	0.00%

3' X 3' WT

Table C.5 %ΔC_L.

Wing ID	**W10**			**W11**			**W12**			**W13**		
Re	1 x 10^5	1.5 x 10^5	2 x 10^5	1 x 10^5	1.5 x 10^5	2 x 10^5	1 x 10^5	1.5 x 10^5	2 x 10^5	1 x 10^5	1.5 x 10^5	2 x 10^5
α	-----	-----	-----	-----	-----	-----	-----	-----	-----	-----	-----	-----
2.5˚	-28.8%	-34.7%	-28.8%	29.7%	8.53%	-2.93%	-12.0%	-5.24%	-19.4%	3.79%	4.87%	-13.5%
5˚	-18.1%	-12.8%	-14.3%	9.35%	-1.92%	0.33%	-10.0%	-2.67%	-4.40%	-3.13%	-5.48%	-8.04%
7.5˚	-11.7%	-8.64%	-5.11%	3.50%	-1.88%	0.88%	-4.86%	-1.17%	-1.50%	-8.11%	-6.66%	-6.98%
10˚	-9.99%	-5.67%	-5.35%	-0.54%	-3.83%	-3.87%	-4.89%	-5.29%	-3.94%	-4.10%	-6.29%	-6.27%
12.5˚	-9.85%	-5.46%	-7.98%	4.77%	0.02%	-3.02%	-2.94%	-3.67%	-5.47%	-2.47%	-3.52%	-5.93%
15˚	-9.25%	-5.52%	-2.78%	4.35%	-3.02%	2.17%	-2.05%	-1.93%	-1.03%	-4.63%	-6.05%	-3.61%
17.5˚	-8.59%	-3.97%	-2.18%	5.15%	1.13%	2.44%	-0.39%	0.29%	1.89%	-1.45%	-3.85%	-1.65%
20˚	-6.74%	-0.86%	-4.59%	6.54%	2.32%	-0.71%	-0.72%	1.52%	-1.25%	-1.53%	-2.76%	-1.83%
22.5˚	-5.64%	-2.81%	-3.93%	5.25%	0.85%	2.06%	0.27%	3.93%	-1.43%	0.76%	-1.45%	-4.22%
25˚	-5.39%	-1.15%	-1.41%	8.94%	2.68%	4.52%	3.48%	1.65%	1.66%	1.25%	-0.15%	3.94%
27.5˚	-7.28%	-2.03%	-2.42%	4.14%	1.66%	1.97%	-1.62%	1.21%	0.04%	-2.41%	-0.35%	-0.39%
30˚	-8.95%	-2.55%	-1.62%	2.15%	0.17%	1.75%	-1.71%	-1.38%	-1.04%	-3.22%	-2.24%	-2.44%

Table C.6 %ΔC_D.

Wing ID	**W10**			**W11**			**W12**			**W13**		
Re	1 x 10^5	1.5 x 10^5	2 x 10^5	1 x 10^5	1.5 x 10^5	2 x 10^5	1 x 10^5	1.5 x 10^5	2 x 10^5	1 x 10^5	1.5 x 10^5	2 x 10^5
α	-----	-----	-----	-----	-----	-----	-----	-----	-----	-----	-----	-----
2.5˚	24.5%	8.22%	21.9%	-10.2%	-7.69%	6.58%	9.26%	4.21%	18.7%	-16.9%	-17.1%	-12.4%
5˚	15.3%	7.68%	14.4%	-4.88%	-3.14%	8.52%	2.09%	4.94%	14.6%	-15.9%	-17.6%	-13.9%
7.5˚	4.24%	1.83%	6.58%	-5.63%	-3.25%	4.42%	-3.60%	1.43%	6.83%	-14.8%	-12.2%	-8.56%
10˚	-0.56%	-0.17%	2.42%	-5.78%	-4.27%	0.19%	-6.89%	-2.45%	1.10%	-10.9%	-10.5%	-6.06%
12.5˚	-2.57%	0.14%	0.01%	-1.78%	-0.39%	-0.04%	-4.77%	-1.29%	-1.32%	-8.44%	-6.46%	-5.11%
15˚	-2.46%	-1.66%	2.61%	-1.94%	-2.56%	3.26%	-4.27%	-1.52%	2.25%	-8.64%	-7.01%	-2.08%
17.5˚	-4.25%	-0.82%	1.75%	-0.72%	-0.00%	3.67%	-3.79%	0.04%	3.93%	-6.42%	-5.36%	-1.35%
20˚	-3.55%	1.00%	-1.20%	1.60%	1.16%	0.24%	-3.37%	1.20%	1.03%	-5.22%	-3.94%	-1.79%
22.5˚	-3.08%	-0.82%	-1.26%	1.17%	0.04%	2.69%	-2.10%	3.43%	0.09%	-2.74%	-2.61%	-3.85%
25˚	-3.38%	0.22%	0.59%	4.89%	1.78%	4.75%	0.84%	1.41%	2.65%	-1.91%	-1.31%	3.46%
27.5˚	-5.85%	-1.14%	-0.93%	1.22%	0.94%	2.33%	-3.32%	0.81%	0.86%	-4.82%	-1.50%	-0.72%
30˚	-7.78%	-1.73%	-0.54%	-0.09%	-0.36%	2.06%	-3.28%	-1.60%	-0.51%	-5.19%	-2.82%	-2.61%

Table C.7 %ΔC_M.

Wing ID	**W10**			**W11**			**W12**			**W13**		
Re	1 x 10^5	1.5 x 10^5	2 x 10^5	1 x 10^5	1.5 x 10^5	2 x 10^5	1 x 10^5	1.5 x 10^5	2 x 10^5	1 x 10^5	1.5 x 10^5	2 x 10^5
α	-----	-----	-----	-----	-----	-----	-----	-----	-----	-----	-----	-----
2.5°	-111.5%	-121.3%	-167.2%	26.5%	356.6%	6.93%	-81.1%	-60.5%	-192.1%	-43.0%	-86.5%	-165.0%
5°	-127.9%	-129.2%	-165.7%	10.5%	661.1%	-76.9%	-105.3%	-86.5%	-223.3%	-65.7%	-117.0%	-203.5%
7.5°	-59.4%	-40.6%	-18.6%	0.30%	275.0%	-9.61%	-48.2%	-33.2%	-31.1%	-73.3%	-78.2%	-81.8%
10°	-34.7%	-23.4%	-18.1%	-9.67%	83.3%	-22.2%	-32.7%	-26.7%	-28.6%	-34.9%	-44.9%	-41.0%
12.5°	-31.7%	-19.9%	-15.9%	-5.67%	28.8%	-15.1%	-25.7%	-17.1%	-27.4%	-26.6%	-31.3%	-27.4%
15°	-30.9%	-19.2%	-12.4%	-7.74%	8.58%	-13.0%	-25.1%	-20.7%	-21.9%	-28.4%	-31.8%	-27.6%
17.5°	-28.4%	-16.2%	-8.89%	-6.21%	-2.06%	-10.5%	-21.7%	-15.8%	-16.7%	-22.2%	-26.5%	-23.6%
20°	-24.2%	-10.2%	-9.47%	-3.81%	-4.51%	-12.8%	-21.0%	-12.2%	-17.0%	-20.4%	-23.3%	-20.6%
22.5°	-21.8%	-11.7%	-9.95%	-4.10%	-4.14%	-6.68%	-19.2%	-11.9%	-17.2%	-17.6%	-21.4%	-22.0%
25°	-22.5%	-8.86%	-5.54%	0.37%	-7.04%	-3.74%	-15.8%	-9.81%	-13.5%	-17.2%	-20.2%	-13.6%
27.5°	-24.3%	-11.0%	-7.67%	-5.27%	-11.5%	-6.55%	-21.2%	-11.4%	-16.4%	-21.1%	-19.6%	-18.7%
30°	-25.3%	-10.7%	-5.95%	-6.81%	-18.5%	-6.29%	-20.4%	-12.3%	-16.2%	-20.3%	-20.7%	-18.6%

Table C.8 %$\Delta C_L/C_D$.

Wing ID	**W10**			**W11**			**W12**			**W13**		
Re	1 x 10^5	1.5 x 10^5	2 x 10^5	1 x 10^5	1.5 x 10^5	2 x 10^5	1 x 10^5	1.5 x 10^5	2 x 10^5	1 x 10^5	1.5 x 10^5	2 x 10^5
α	-----	-----	-----	-----	-----	-----	-----	-----	-----	-----	-----	-----
2.5°	-42.8%	-39.6%	-41.6%	44.5%	17.6%	-8.92%	-19.5%	-9.07%	-32.1%	24.9%	26.6%	-1.20%
5°	-28.9%	-19.0%	-25.1%	15.0%	1.26%	-7.55%	-11.9%	-7.26%	-16.6%	15.2%	14.7%	6.82%
7.5°	-15.3%	-10.3%	-11.0%	9.67%	1.42%	-3.39%	-1.31%	-2.56%	-7.80%	7.92%	6.37%	1.72%
10°	-9.48%	-5.51%	-7.59%	5.56%	0.46%	-4.05%	2.15%	-2.91%	-4.98%	7.65%	4.70%	-0.22%
12.5°	-7.47%	-5.59%	-7.99%	6.66%	0.41%	-2.99%	1.92%	-2.41%	-4.19%	6.52%	3.14%	-0.86%
15°	-6.96%	-3.93%	-5.25%	6.41%	-0.47%	-1.06%	2.32%	-0.42%	-3.20%	4.39%	1.04%	-1.56%
17.5°	-4.53%	-3.18%	-3.86%	5.91%	1.13%	-1.19%	3.53%	0.25%	-1.96%	5.31%	1.60%	-0.30%
20°	-3.31%	-1.83%	-3.42%	4.86%	1.15%	-0.95%	2.74%	0.32%	-2.26%	3.90%	1.23%	-0.04%
22.5°	-2.64%	-2.00%	-2.70%	4.04%	0.81%	-0.61%	2.42%	0.49%	-1.51%	3.59%	1.19%	-0.38%
25°	-2.09%	-1.37%	-1.98%	3.87%	0.88%	-0.22%	2.62%	0.24%	-0.97%	3.22%	1.18%	0.46%
27.5°	-1.53%	-0.90%	-1.51%	2.88%	0.71%	-0.35%	1.76%	0.40%	-0.81%	2.53%	1.16%	0.33%
30°	-1.27%	-0.83%	-1.09%	2.24%	0.53%	-0.31%	1.62%	0.23%	-0.53%	2.09%	0.60%	0.17%

Table C.9 %$\Delta(C_L/C_D)$/weight.

Wing ID	**W10**			**W11**			**W12**			**W13**		
Re	1 x 10^5	1.5 x 10^5	2 x 10^5	1 x 10^5	1.5 x 10^5	2 x 10^5	1 x 10^5	1.5 x 10^5	2 x 10^5	1 x 10^5	1.5 x 10^5	2 x 10^5
α	-----	-----	-----	-----	-----	-----	-----	-----	-----	-----	-----	-----
2.5°	-39.9%	-36.6%	-38.6%	49.3%	21.5%	-5.89%	-13.9%	-2.83%	-27.4%	42.8%	44.8%	13.0%
5°	-25.3%	-14.9%	-21.3%	18.8%	4.63%	-4.47%	-5.81%	-0.89%	-10.9%	31.8%	31.2%	22.2%
7.5°	-11.0%	-5.74%	-6.46%	13.3%	4.80%	-0.17%	5.46%	4.13%	-1.47%	23.5%	21.7%	16.4%
10°	-4.90%	-0.72%	-2.91%	9.07%	3.80%	-0.86%	9.16%	3.75%	1.55%	23.2%	19.8%	14.2%
12.5°	-2.78%	-0.80%	-3.33%	10.2%	3.75%	0.24%	8.92%	4.29%	2.39%	21.9%	18.0%	13.4%
15°	-2.25%	0.94%	-0.45%	9.95%	2.84%	2.23%	9.35%	6.42%	3.44%	19.4%	15.6%	12.6%
17.5°	0.30%	1.73%	1.01%	9.44%	4.49%	2.10%	10.6%	7.13%	4.77%	20.5%	16.2%	14.1%
20°	1.59%	3.14%	1.47%	8.35%	4.52%	2.35%	9.79%	7.20%	4.45%	18.9%	15.8%	14.4%
22.5°	2.29%	2.96%	2.23%	7.50%	4.16%	2.69%	9.46%	7.39%	5.25%	18.5%	15.8%	14.0%
25°	2.88%	3.63%	2.98%	7.33%	4.24%	3.10%	9.66%	7.12%	5.83%	18.1%	15.8%	14.9%
27.5°	3.46%	4.12%	3.49%	6.31%	4.07%	2.96%	8.75%	7.29%	6.00%	17.3%	15.7%	14.8%
30°	3.73%	4.20%	3.92%	5.65%	3.88%	3.01%	8.60%	7.11%	6.30%	16.8%	15.1%	14.6%

APPENDIX G: 3’ X 3’ WT ADDITIONAL PLOTS

a) C_L:

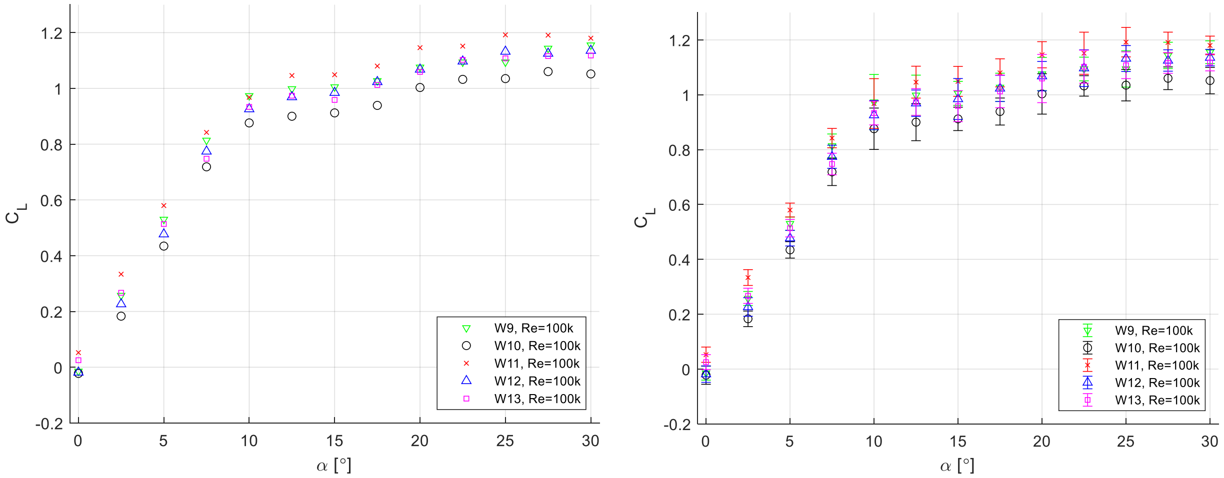

Figure G.1 C_L at Re ≈ 100,000.

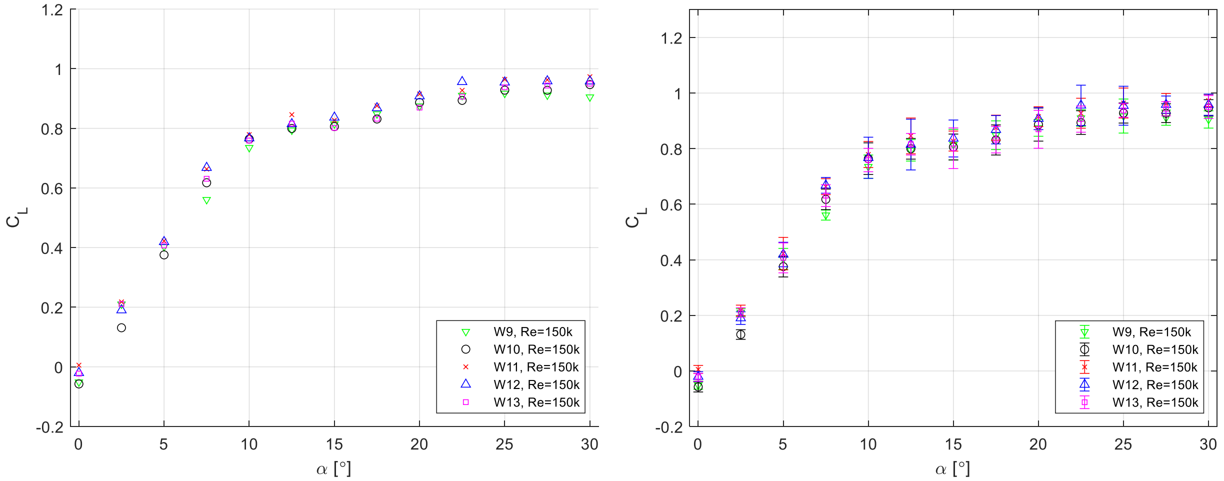

Figure G.2 C_L at Re ≈ 150,000.

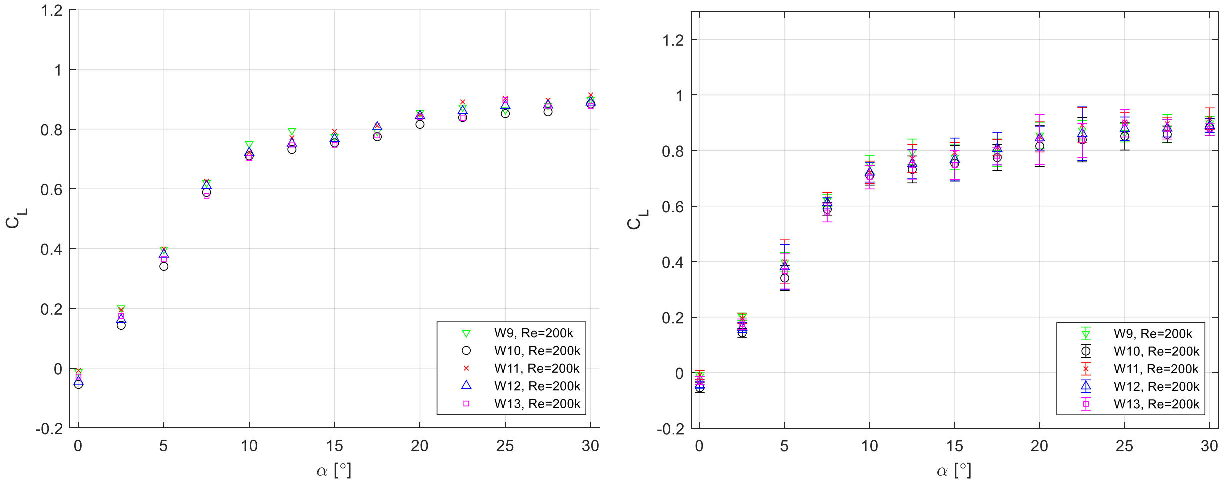

Figure G.3 C_L at Re ≈ 200,000.

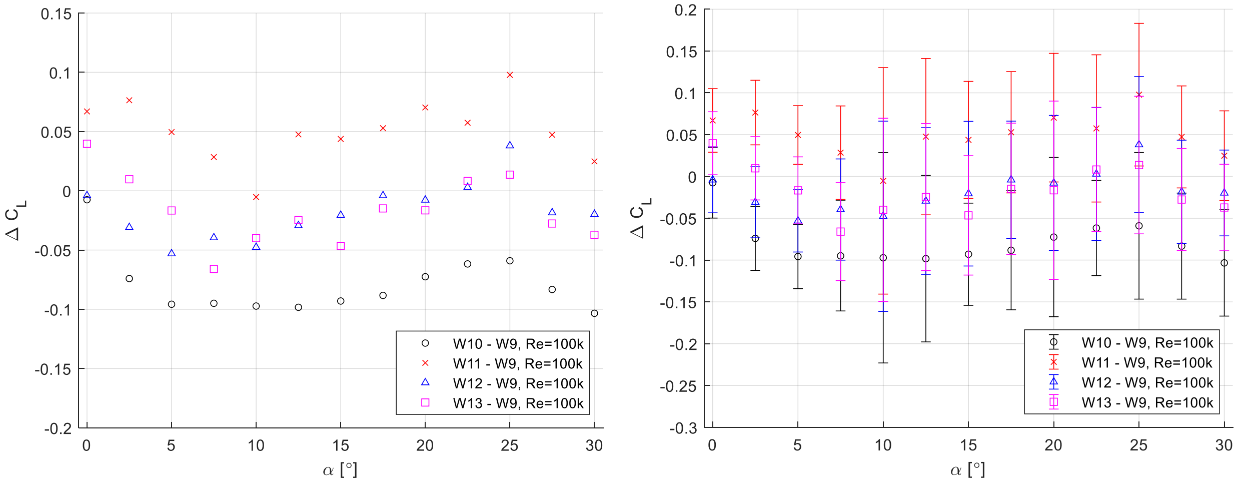

Figure G.4 ΔC_L at Re ≈ 100,000.

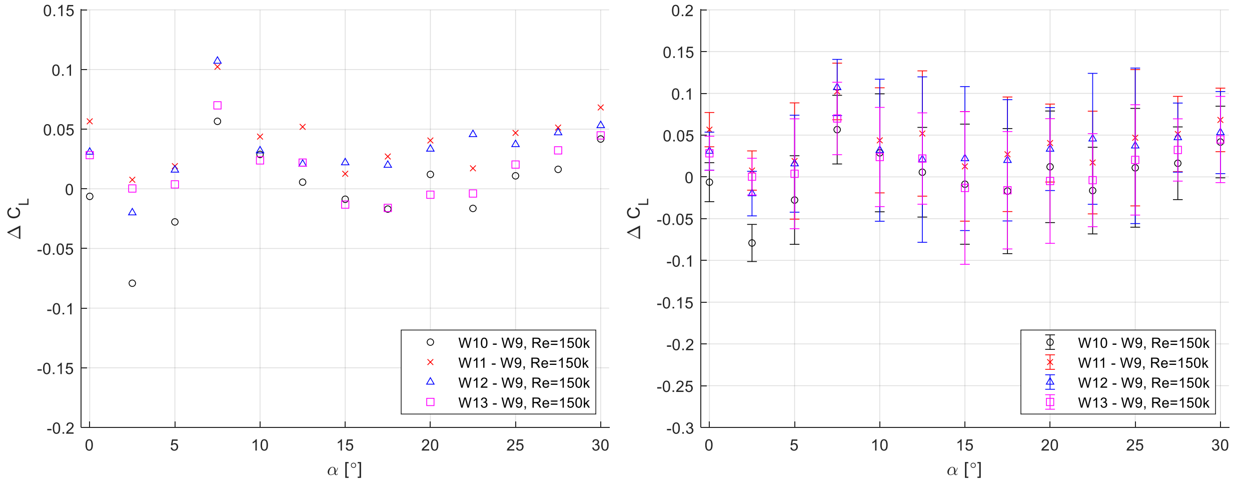

Figure G.5 ΔC_L at Re ≈ 150,000.

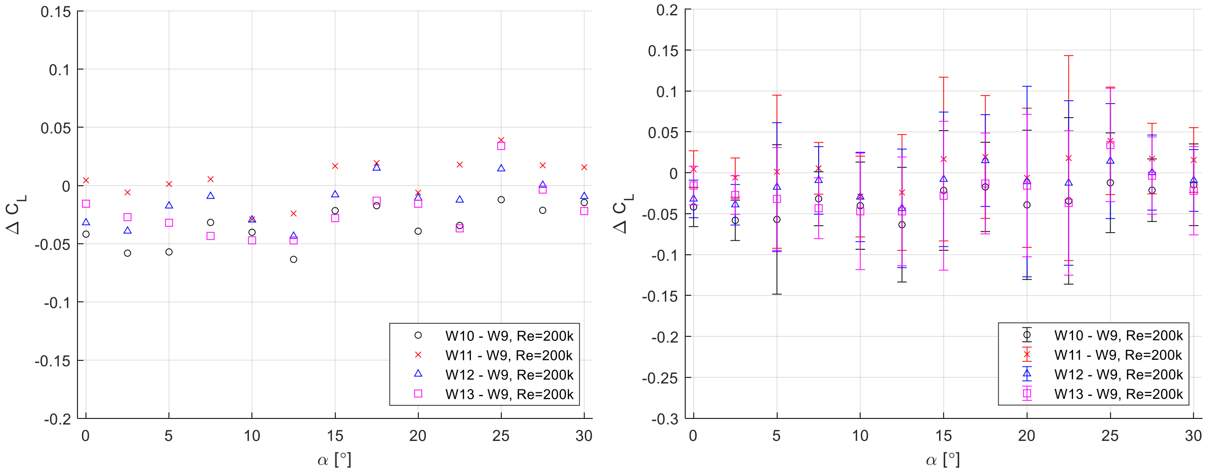

Figure G.6 ΔC_L at Re ≈ 200,000.

b) C_D:

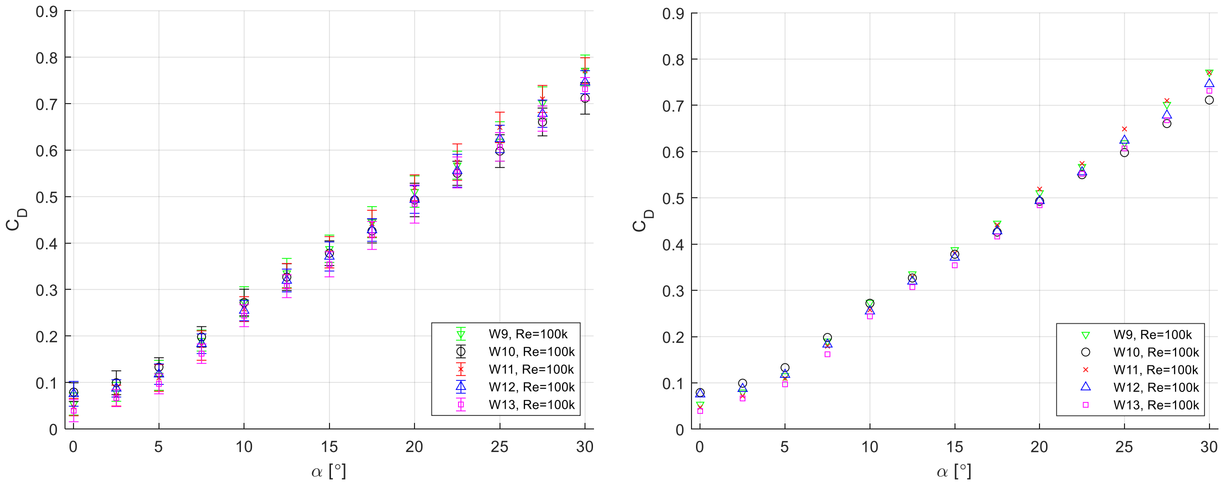

Figure G.7 C_D at Re ≈ 100,000.

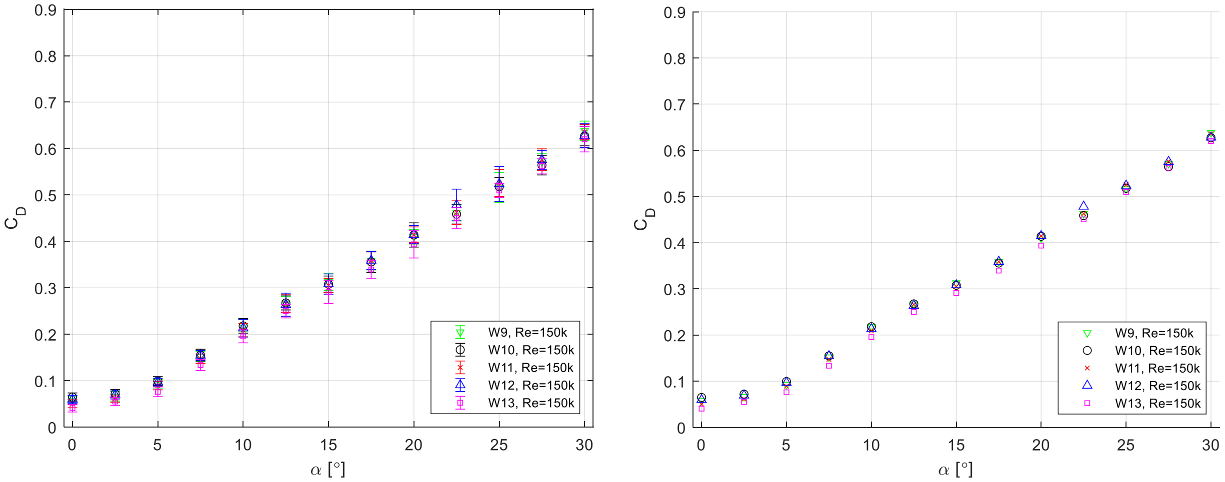

Figure G.8 C_D at Re ≈ 150,000.

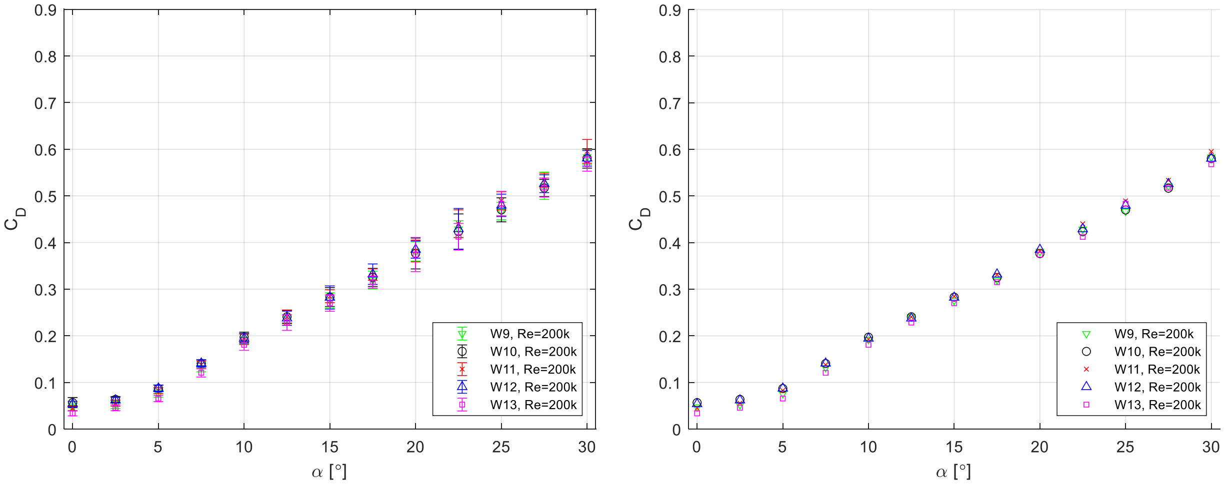

Figure G.9 C_D at Re ≈ 200,000.

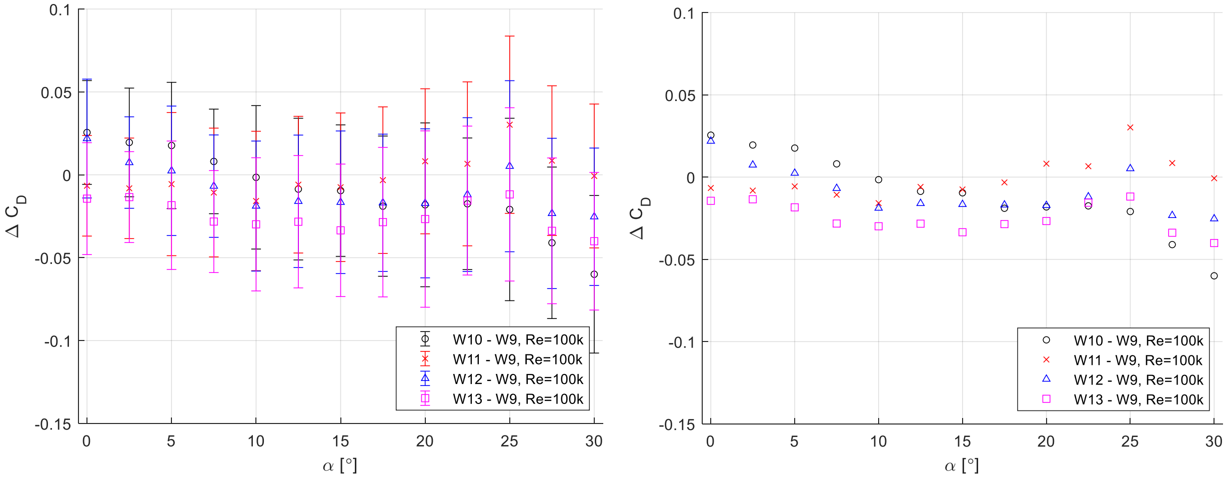

Figure G.10 ΔC_D at Re ≈ 100,000.

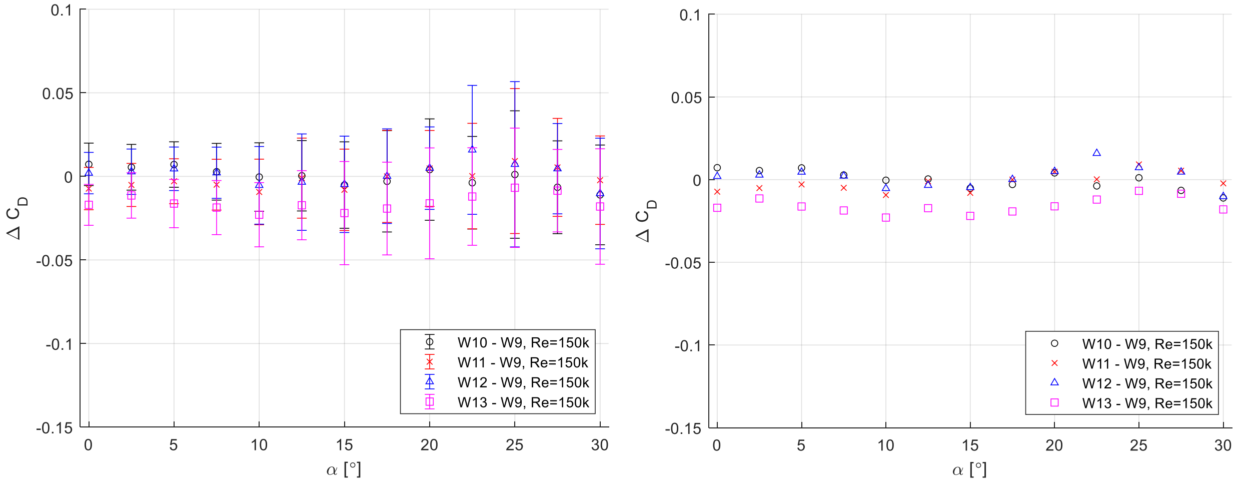

Figure G.11 ΔC_D at Re ≈ 150,000.

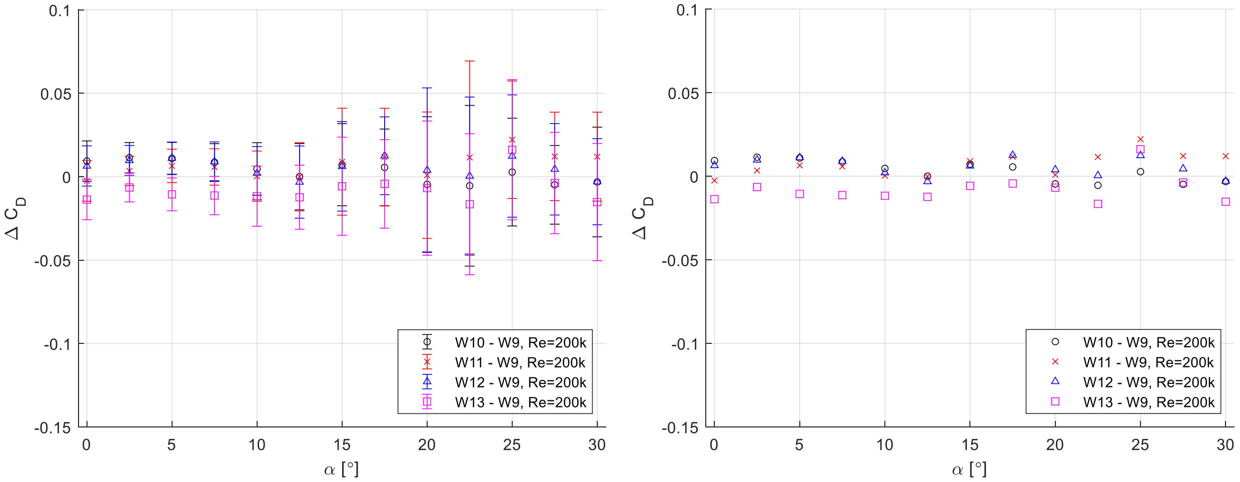

Figure G.12 ΔC_D at Re ≈ 200,000.

c) C_M:

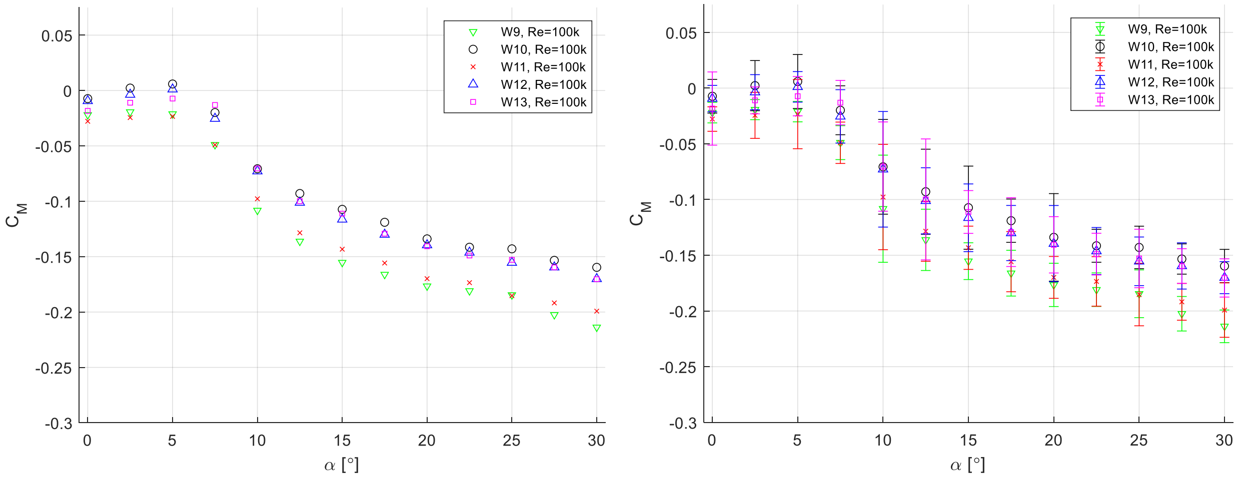

Figure G.13 C_M at Re ≈ 100,000.

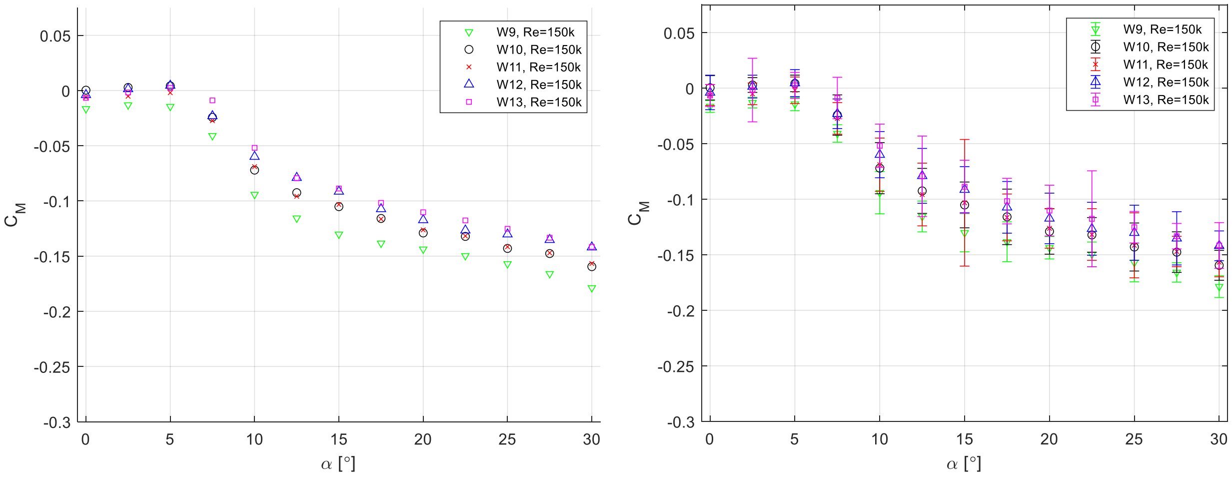

Figure G.14 C_M at Re ≈ 150,000.

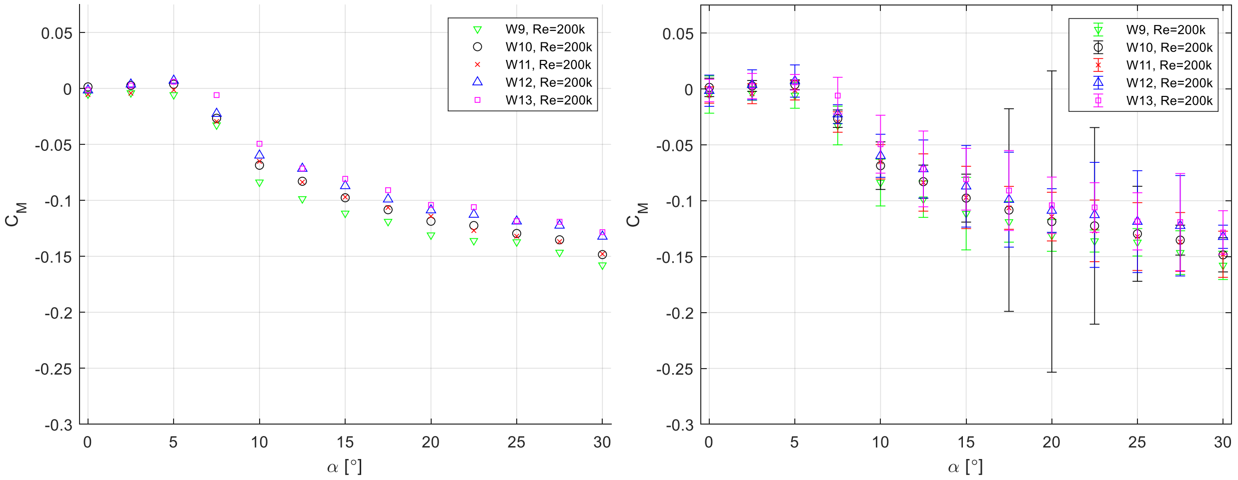

Figure G.15 C_M at Re ≈ 200,000.

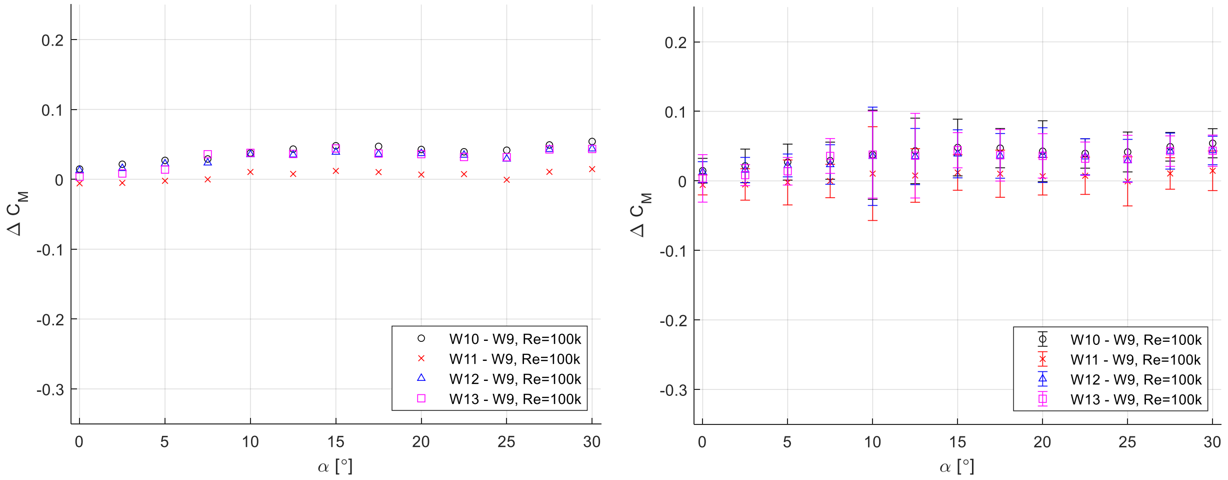

Figure G.16 ΔC_M at Re ≈ 100,000.

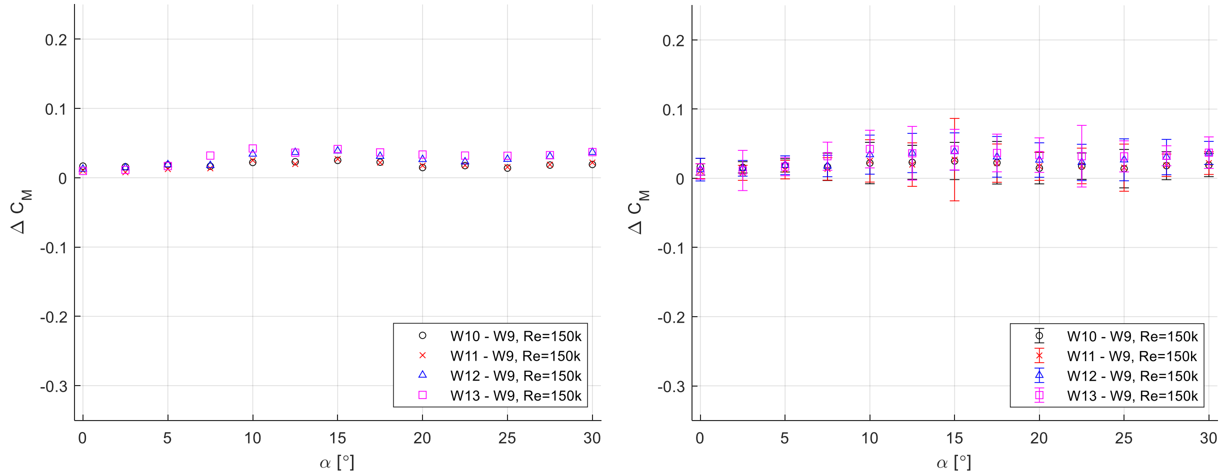

Figure G.17 ΔC_M at Re ≈ 150,000.

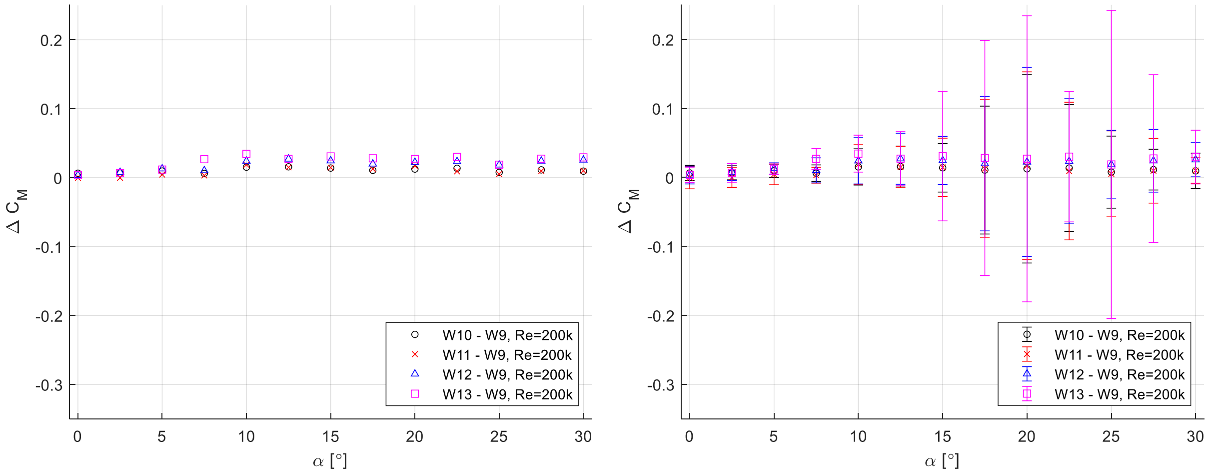

Figure G.18 ΔC_M at Re ≈ 200,000.

d) C_L/C_D:

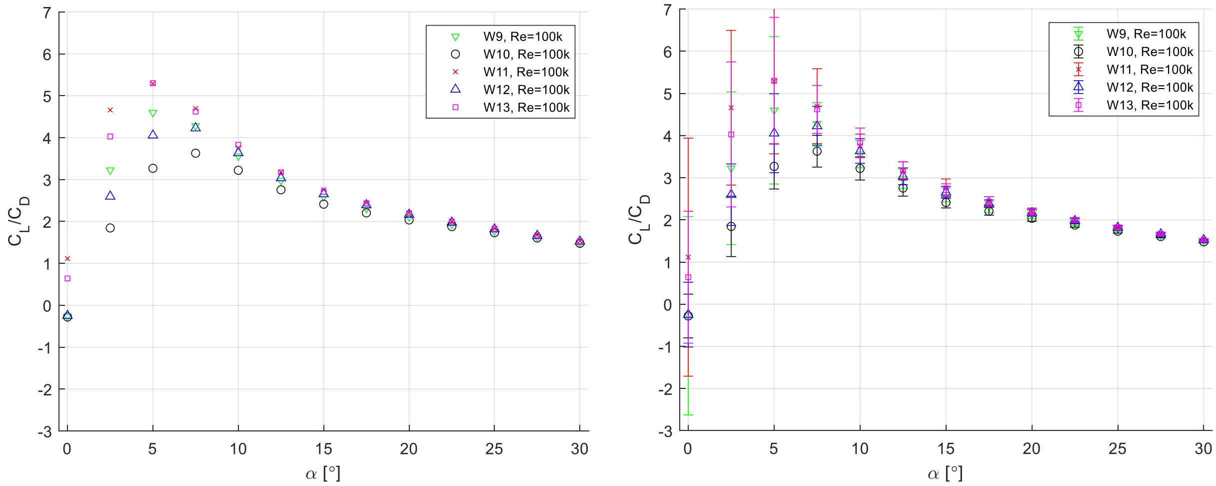

Figure G.19 C_L/C_D at Re ≈ 100,000.

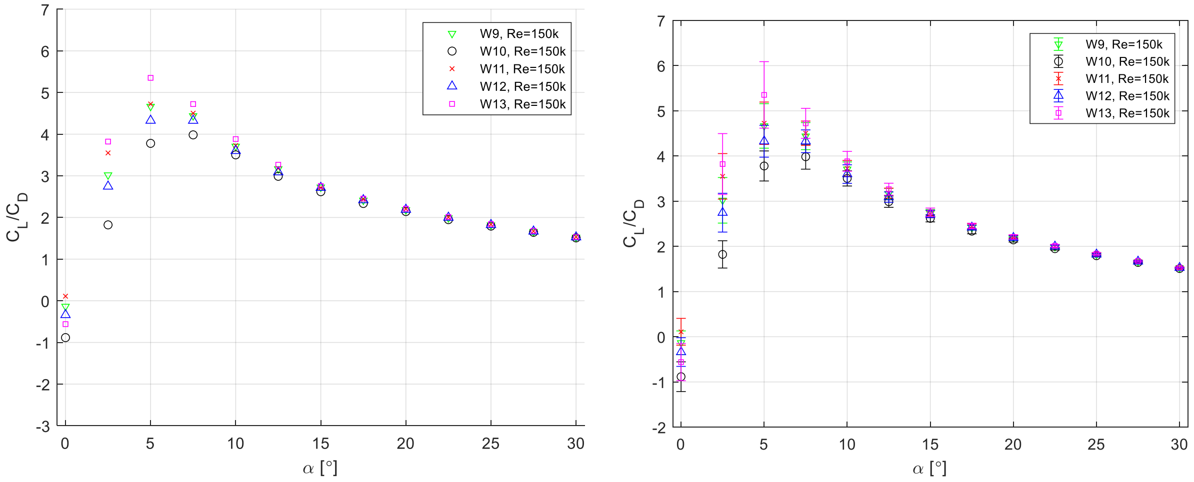

Figure G.20 C_L/C_D at Re ≈ 150,000.

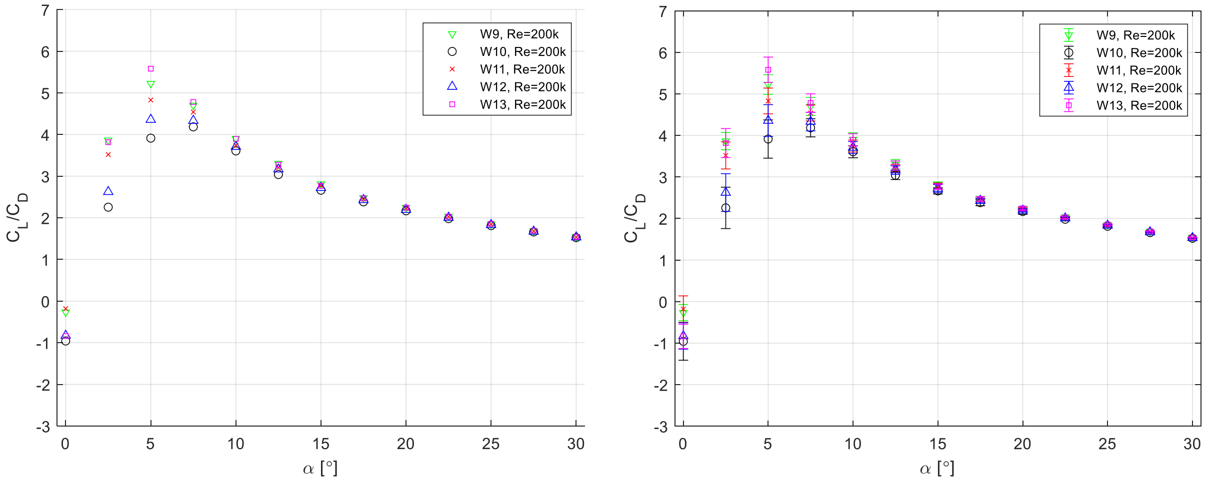

Figure G.21 C_L/C_D at Re ≈ 200,000.

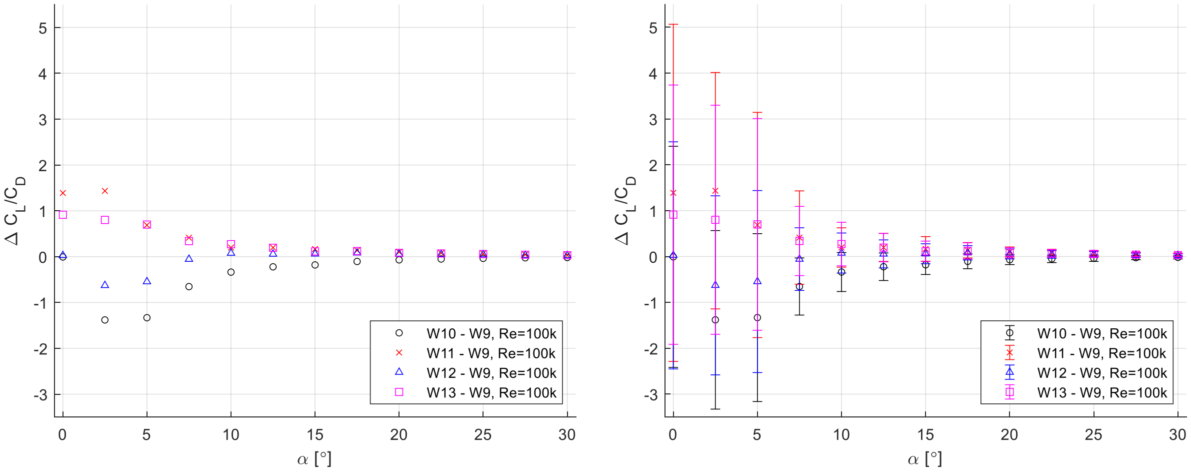

Figure G.22 $\Delta C_L/C_D$ at Re ≈ 100,000.

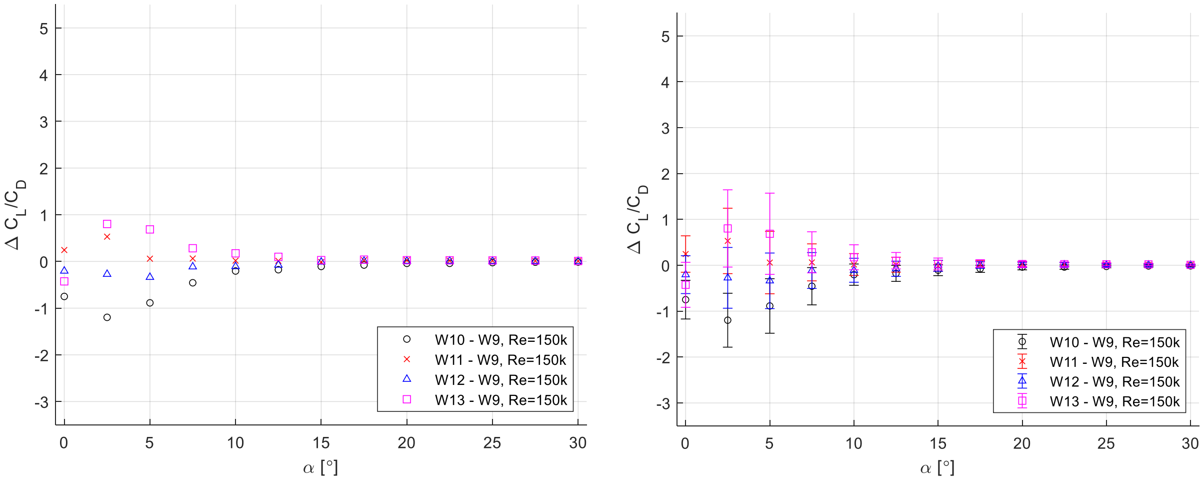

Figure G.23 $\Delta C_L/C_D$ at Re ≈ 150,000.

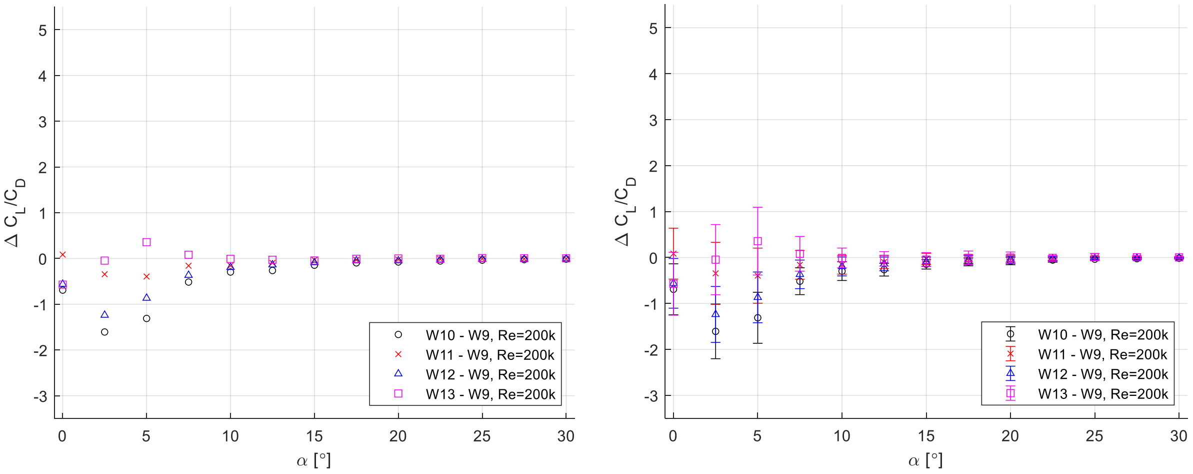

Figure G.24 $\Delta C_L/C_D$ at Re ≈ 200,000.

e) (C_L/C_D)/weight:

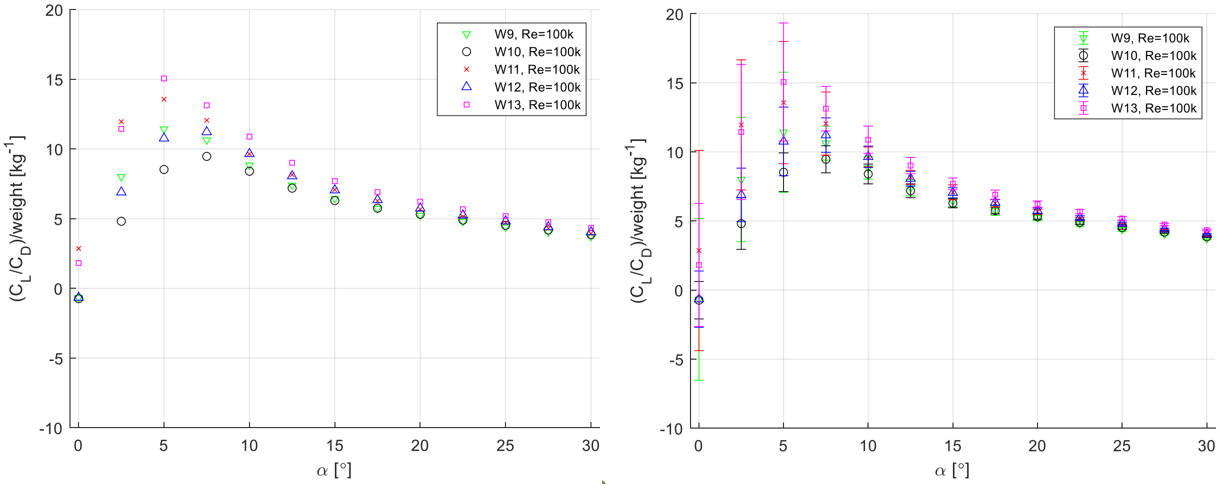

Figure G.25 (C_L/C_D)/Weight at Re ≈ 100,000.

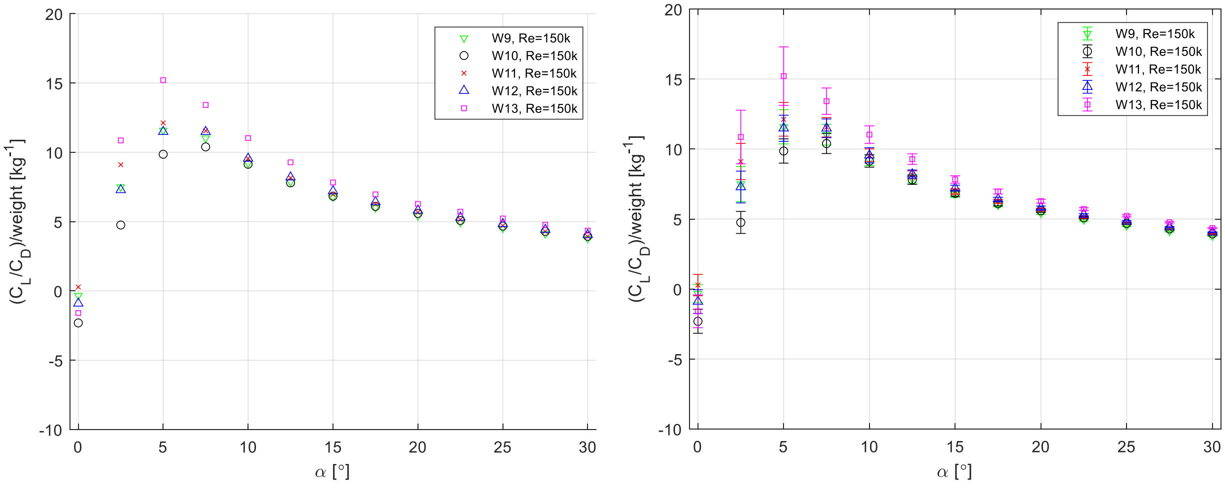

Figure G.26 (C_L/C_D)/Weight at Re ≈ 150,000.

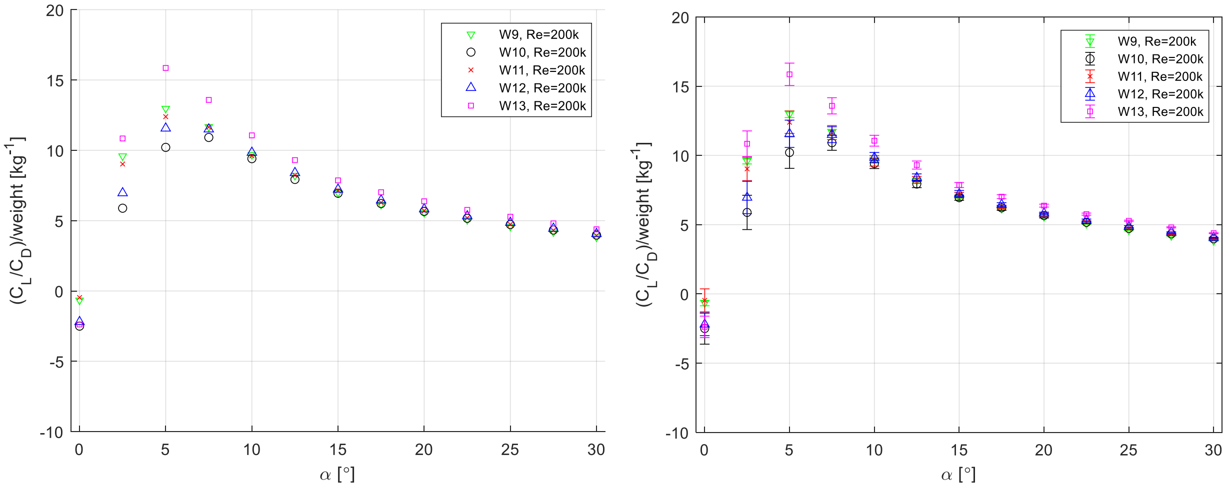

Figure G.27 (C$_L$/C$_D$)/Weight at Re ≈ 200,000.

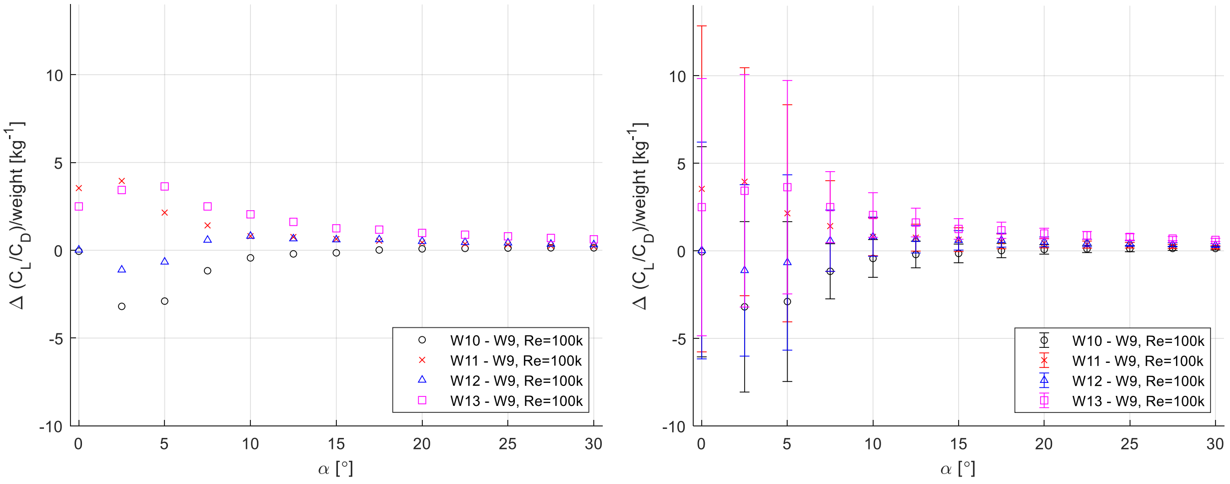

Figure G.28 Δ(C$_L$/C$_D$)/Weight at Re ≈ 100,000.

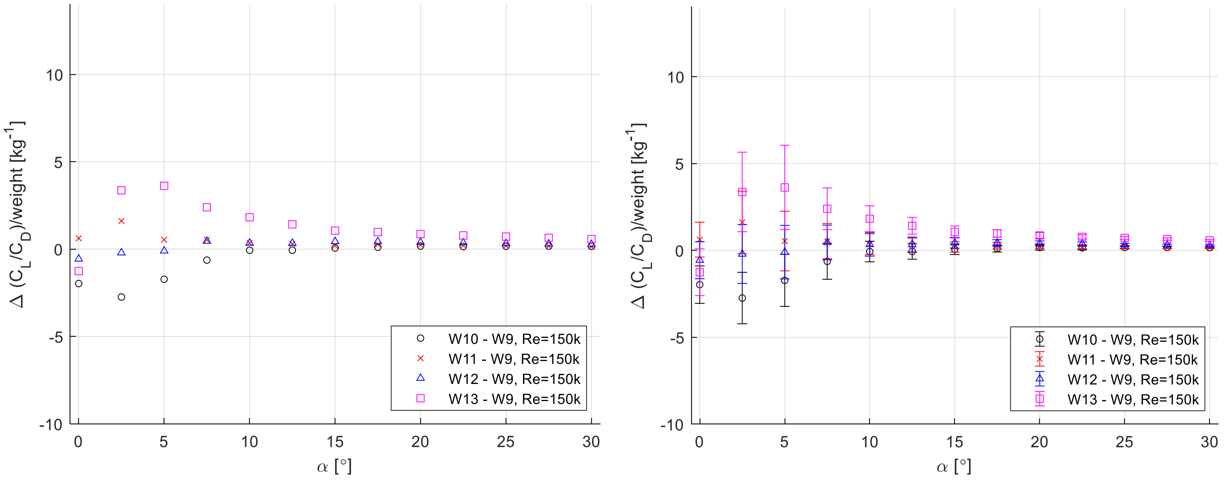

Figure G.29 Δ(C$_L$/C$_D$)/Weight at Re ≈ 150,000.

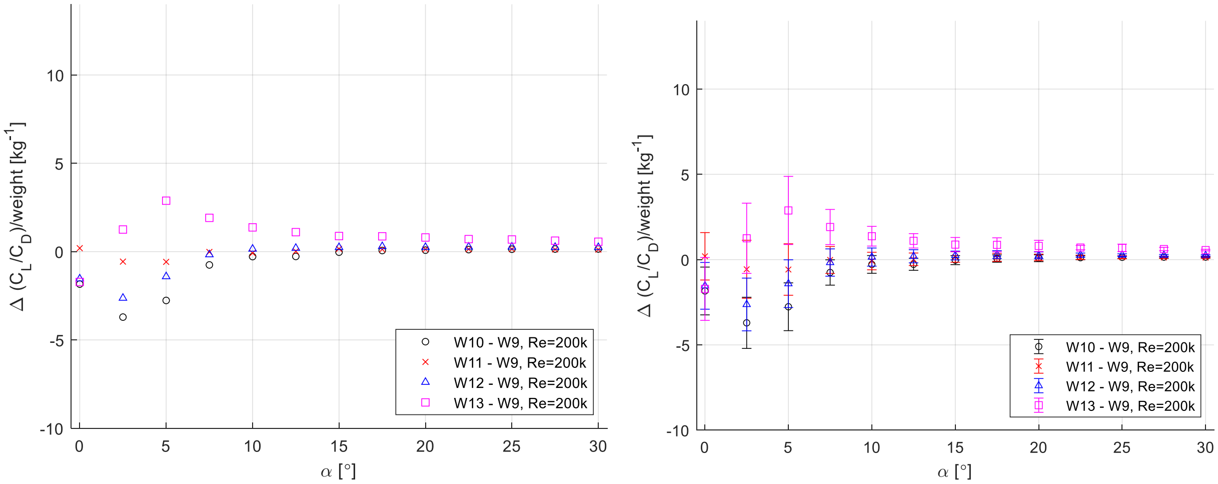

Figure G.30 $\Delta(C_L/C_D)$/Weight at Re ≈ 200,000.

VITA

Born in Rio de Janeiro, Brazil, Israel Bron Simplicio has a B.S. in mechanical engineering. Israel focuses on experimental fluid dynamics. He is passionate about aerodynamics and developments in the aviation industry.